

Electric Deflection Measurements of Sodium Clusters in a Molecular Beam

A Thesis
Presented to
The Academic Faculty

by

Anthony Liang

In Partial Fulfillment
of the Requirements for the Degree
Doctor of Philosophy

School of Physics
Georgia Institute of Technology
December 2009

Electric Deflection Measurements of Sodium Clusters in a Molecular Beam

Approved by:

Professor Walter de Heer
School of Physics
Georgia Institute of Technology, Advisor

Professor Andrew Zangwill
School of Physics
Georgia Institute of Technology

Professor Mei-Yin Chou
School of Physics
Georgia Institute of Technology

Professor Phillip First
School of Physics
Georgia Institute of Technology

Professor Robert Whetten
School of Chemistry
Georgia Institute of Technology

Date Approved: Oct 26, 2009

To my parents, Shen-Min Liang and Lee-Chiou Liau.

ACKNOWLEDGEMENTS

It is my great pleasure to have known and worked with many people during the years in Georgia Tech. I am deeply grateful to have my advisor, Professor Walter A. de Heer, to give me rich guidance, solid training which one would need to become a science researcher in this era.

I would like to express my sincere thankfulness to my committee members: Professor Walter A. de Heer, Professor Mei-Yin Chou, Professor Robert Whetten, Professor Andrew Zangwill and Professor Phillip First for their precious time spent on my thesis and their constructive suggestion.

I also cordially appreciate my teammates, John Bowlan, Xiao-Shan Xu and Shuangye Yin for all this years working together and numerous fruitful discussion. I also want to thank Professor Mei-Yin Chou, Professor Robert L. Whetten, Professor Phillip First and Professor Brian Kennedy for answering my physics questions.

My obligation to the staff of physics department of Georgia Tech, Debbi James, Kelvin Carter, Keith Garner, Scott Centers, Samantha King, Lori Federico, Jennifer Fairchild-Pierce, Felicia Goolsby, Judy Melton, Velera Pate and Victoria Speights, is from their help of making everyday life smooth. I would also like to express gratitude to Sam Mize and Norman Scott from the machine shop, for the quality machining, training and expert advice which have been essential for our experiment.

TABLE OF CONTENTS

DEDICATION	iii
ACKNOWLEDGEMENTS	iv
LIST OF TABLES	vii
LIST OF FIGURES	viii
SUMMARY	xv
I INTRODUCTION	1
1.1 Metal Clusters	2
II BACKGROUND THEORY	8
2.1 Classical Conducting Triaxial Ellipsoid	8
2.2 Molecular Polarizability and Electric Susceptibility	13
2.2.1 Harmonic Bound Charges (electrons and ions)	13
2.2.2 Quantum Mechanical Description	14
2.2.3 Electric Susceptibility and Electric Dipole Moment (EDM)	17
2.3 Electronic Shell Structure and Magic Numbers of Simple Metal Clusters	21
2.4 Earlier Works on Polarizability and EDM of Sodium Metal Cluster	27
2.4.1 Static Dipole Polarizability	27
III EXPERIMENTAL SETUP/METHODS	31
3.1 Molecular Beam Method	31
3.2 The Production of Gas Phase Clusters	33
3.2.1 Cluster Generation: Pulsed Vaporization within An Inert Gas Flow	33
3.2.2 Growth of Clusters at Low Temperature	35
3.3 Formation of a Beam via Free Jet Expansion	39
3.4 Beam Electric Deflection	44
3.4.1 Deflection of a Single Particle and of a Beam	46
3.5 Adiabatic Electric Polarization Distribution of a Ensemble	50
3.5.1 Nonpolar and Polarizable Clusters	52
3.5.2 Polar clusters	54
3.6 Beam Profiles	68

3.6.1	To Get the Polarizability	69
3.6.2	To Get the EDM	70
3.7	Speed Measurements	73
3.8	Detection and Recording of Spectrum	76
IV	RESULTS AND DISCUSSION	82
4.1	Averaged Static Dipole Polarizability of Sodium Clusters at 20 °K	82
4.1.1	Measured Results	82
4.1.2	Polarizability Enhancement due to Triaxial Ellipsoidal Distortion	86
4.1.3	The Effect of Electronic Shell Structure on Polarizability	90
4.2	Upper Bound on Electric Dipole Moments of Sodium Clusters	97
4.2.1	Possible Dipole Moment of Na ₆	100
4.2.2	A Short Look at Gold Cluster Au ₉	103
APPENDIX A	— ANCILLARY	106
APPENDIX B	— PHOTOABSORPTION OF SODIUM CLUSTERS	112
REFERENCES	115
VITA	123

LIST OF TABLES

1	Experimental observed magic numbers and the theoretical prediction. . . .	25
2	Pressures, mean free paths and the types of pumps in the differentially pumped environment.	40
3	Finite difference numerical method is used to generate the beam profile of a beam of polarizable spheres.	48
4	The polarization distributions and their first and second moment (mean and variance) for three kinds of rigid polar rotors: spherical, symmetric and asymmetric. Under low field limit.	65

LIST OF FIGURES

1	This antique engraved Czechoslovakian glass shows color produced by colloidal suspensions. When gold is in metallic colloidal form, as in the 10-nm-diameter particles in "ruby glass", the "Mie scattering theory" has to be used to explain the unexpected red color illustrated. Ref. www.webexhibits.org .	3
2	Different sized quantum dot nanoparticles are shown above, first in ultraviolet light and then in ambient light. The length of the synthesis reaction determines particle size. Unlike the metal clusters in the cup these solutions contain semiconductor CdSe clusters. Their size increases from left to right. The color depends on the size. From Ref. www.webexhibits.org	4
3	As the number of neighboring atoms increases, the spacing between the energy levels decreases. More overlap occurs and bands of low and high energy replace the distinct energy levels. As more atoms combine, the distance between the two bands decreases, the band gap decreases. From Ref. http://www.webexhibits.org/	4
4	The approximate spherical symmetry of the cluster imposes a DOS with pronounced level bunching. This graph present the electronic levels in three different kinds of central potential that one can approach to the real cluster case. (three-dimentional spherical potential wells). From Ref. [32].	5
5	Illustrative energy levels and DOS of bulk, and of three finite small systems: a quantum well(2-dimension), a quantum wire(1-dimension) and a quantum dot(0-dimension), showing the discrete nature of the energy levels. (Wikipedia)	7
6	A conducting ellipsoid in an uniform electric field along the longest principal axis a	9
7	The effect of a geometry depolarization $1/N_z$, for a oblate spheroid.	11
8	The effect of a geometry depolarization $1/N_z$, for a prolate spheroid.	11
9	Polarizability enhancement $\frac{\alpha_{oblate}}{\alpha_{sphere}} = \frac{1}{9} \sum_{i=1}^3 \frac{1}{N_i}$, a oblate contribution to the polarizability, assuming volume is fixed.	12
10	Polarizability enhancement $\frac{\alpha_{prolate}}{\alpha_{sphere}} = \frac{1}{9} \sum_{i=1}^3 \frac{1}{N_i}$, a prolate contribution to the polarizability, assuming volume is fixed.	12
11	Metal surface charge density simulation by Kohn and Lang[69]. Graph showing charge density without external electric field $n(x)$ and induced charge density distribution $-n_d(x)$ with external electric field. One can clearly see the enhancement of electron spillout due to the screening of electron clouds at the surface. From Ref. [69].	15

12	Predicted perturbed dipole density $-n_d(x)$ for neutral spheres with $r_2=2$ containing $N=70$ and 92 electrons. The dashed curve is the corresponding perturbed density for a plane surface. One can tell that the Friedel oscillation is altered from the bulk surface (dash line) due to finite size effect. From Ref. [11].	16
13	Color representation of the electronic charge transfer of the homonucleus molecule ozone.(upper figure) Due to its sp^2 hybridization bonding nature of the center atom (lower figure), it is a polar molecule with a dipole moment of 0.5337 D. From Ref. Wikipedia.	20
14	An guessed illustration of the center of masses of the electron cloud and of the ionic cores for a metal cluster.	20
15	Dipole moments of the optimized ground state neutral sodium clusters (blue circle) as a function of cluster size calculated by the DFT method[99]. For some clusters, more than one isomer has been considered (green square and yellow triangle). Figure is regenerated from [99].	22
16	Upper figure: high temperature mass spectrum of sodium clusters. Magic-number clusters are more abundant (more stable) than the others. Bottom figure: theoretical prediction. From Ref. [59].	23
17	Low-lying energy levels of a nucleus in a single-particle shell model with a modified oscillator potential without spin-orbit (left) and with spin-orbit (right, the Nilsson model) interaction. The number to the right of a level indicates its degeneracy, $(2j+1)$. The boxed integers indicate the magic numbers. Figure's source: Hyperphysics.com.	23
18	Energy level quantization for electrons confined in three different kinds of central potential (harmonic, intermediate and square wall three-dimentional spherical potential wells). A metal cluster's energy levels actually resemble this. From Ref. [32].	24
19	Ionization potentials measurements on sodium and potassium clusters reveals the electronic shell structure. The general trend gradually decreases as a function of size and approaches the bulk work function. From Ref. [32]. . .	26
20	In 1962, Mackay presented a family of icosahedral structures as 'a dense non-crystallographic packing of eqaul spheres'. In his report, Mackay showed that clusters containing certain 'magic numbers' of identical atoms may form compact, nearly spherical structures with surfaces that are nearly close-packed. Each of these icosahedral structures is composed of 20 fused, distorted tetrahedra. From Ref. [72].	27
21	The previously measured $\bar{\alpha}$ is plotted. Figure is a courtesy from [100] (A oven cluster source. Vapor temperature 873 K. Argon carrier gas with a pressure of 600-620 kPa. Nozzle diameter is $75\ \mu m$ (with supersonic expansion) and temperature of clusters is measured to be 1093K.)	28

22	Polarizability of all the elements on the periodic table. The trend can be explained by considering the radius of the atom. Generally speaking, as the atomic number increases along each row of the periodic table, the additional electrons go into the same outermost shell; whose radius gradually contracts, due to the increasing nuclear charge. In a noble gas, the outermost shell is completely filled; therefore, the additional electron of next alkali metal will go into the next outer shell, accounting for the sudden increase in the atomic radius. (The increasing nuclear charge is partly counterbalanced by the increasing number of electrons, a phenomenon that is known as shielding; which explains why the size of atoms usually increases down each column.)	30
23	Ionization potentials of all the elements.	30
24	A look at the whole apparatus. From Ref. [80].	32
25	Schematic of the trajectories of a free cluster when it passes through the inhomogeneous electric field. (field on and field off; the deflection is d .) . . .	33
26	Cluster source layout used in this experiment. Laser vaporization sources produce pure and mixed clusters of most elements. A traditional oven source (or seeded expansion source) is limited to metals with a low boiling point (alkali, etc.)	34
27	Cluster source. Machined from a copper block. Copper is chosen because of its high thermal conductivity.	35
28	Sodium clusters mass spectrum with an high temperature oven source. From Borggreen et al.[21]	36
29	A mass spectrum with a low-temperature (20 K) laser vaporization source showing the structureless, log-normal ($\Gamma=1$) distributed signature characteristics of this source, as opposed to the structural mass spectrum in high temperature source. (Cf. Figure 28)	37
30	Aluminum clusters size distribution with different pressures of helium carrier gas. Notice the intensive peak on the left is the aluminum atom peak. The relative abundance between the atom and the clusters is the largest when backing pressure of helium is the least and vice versa.	38
31	Niobium clusters size distribution with different pressures of helium carrier gas.	39
32	The shape of the heated-nozzle assembly. The middle part will be surrounded by thermalcoax heating element. The thermocouple will be soldered to the copper rind around the front nozzle.	40
33	Illustration of the differential pumping of the system.	41
34	Continuum supersonic free-jet expansion and its interior structure. In the zone of silence there is essentially no collisions between the gas content. Thus a molecular beam can be extracted from the central streamline. From Ref. [95].	42

35	Quitting surface of the expansion. This is where the clusters turn into a molecular beam. This figure is not to scale. Normally the distance of the quitting surface will sit within a distance several orifice diameter away from the nozzle exit.	43
36	A cross section illustration of the electric plates. The strip in the middle indicates the cluster beam shape after collimation.	45
37	A conducting sphere passes through the inhomogeneous transverse electric field and deflects toward the high field.	46
38	Cross section view of the finite difference simulation of conducting <i>spheres</i> passing through the field. Blue dots represent the clusters before they enter the field, yellow dots represent the clusters after they leave the field but with field turned off, and red ones represent the clusters after they leave the field with field turned on.	48
39	The simulated profiles recorded at the detector from Figure 38. Only horizontal information is kept. Vertical information is summed spatially. Red is the profile when the field is on, blue is field off.	49
40	Vector model representation of a symmetric polar rotor under an electric field. Nutation and precession of p_J are shown and the time-averaged effective dipole \bar{p} is indicated. The effective dipole \bar{p} will be the effective polarization of this rotating cluster under electric field in this particular arrangement. In an ensemble the orientation of J , E and p_0 are all random so one will have a distribution of \bar{p} . For a visual illustration on symmetric rotor nutation please see [42].	55
41	Logarithmic polarization distribution. Horizontal is plotting $p = \bar{p}/p_0$. This is the characteristic polarization distribution for a spherical cluster with an intrinsic permanent dipole moment in the zero or low electric field limit. . .	59
42	Polarization distribution of symmetrically prolate ($\gamma = 0.5$), spherical ($\gamma = 1$) and oblate ($\gamma = 2$) tops under high field (or large $\frac{p_0 E}{kT}$). (γ is defined in Eq. 16 and $x = \frac{p_0 E}{kT}$) The important point is that even a spherical polar top can have asymmetrical polarization distribution for large x . Figure Ref. [13]. . .	60
43	The number of configurations of the possible M and K quantum numbers that make up a constant value $M * K = C = \bar{p}_{QM} J(J + 1)$	63
44	In the continuum approximation the number of configurations can be found by calculating the area between the two constant parabola.	63
45	The examination between a real logarithmic function (in red, line) and a distribution of quantized polarization (blue histogram) under low angular momentum J	65
46	Angular momentum $J = 100$. As one can see the distribution (blue histogram) is very close to the logarithmic function (red).	65

47	The Boltzmann factor associated with K quantum number: this is essentially the weighting factor in Eq 88. One can somehow include this and maybe one can derive the polarization distribution (refer to Figure 43). B is the rotational constant. Asymmetry parameter κ is defined in the first chapter.	66
48	Na ₆₀ beam profile with field on and field off.	68
49	(exp1) Electric field off and focus on the large clusters. One can get the width of the collimated profile.	70
50	(exp2) Electric field on and focus on the small clusters. One can get the width contribution from the scattering.	71
51	(exp3) Electric field is on and focus on the large clusters. One can get the field broadening contribution to the width.	72
52	(exp4) Electric field is on and focus on the magic number clusters. One can obtain the scattering and field broadening contribution to the width. . . .	72
53	Setup of the chopper. The geometry of the chopper is on the right bottom. A courtesy figure from [80].	74
54	A spacial representation of middle portion of the clusters beam pulse, showing the intensity distribution of clusters in the beam and the depleted regions caused by the rotating chopper. Z-axis is the cluster intensity, x-axis are the spacial position along the beam streamline and y-axis showing the cluster size.	75
55	An illustration of the TOF mass spectrometer.	77
56	Typical mass spectrum of sodium clusters.	78
57	Position sensitive time of flight illustration. Also shown is the indication of the width of the beam and its corresponding width in the TOF time. . . .	79
58	Second ionization of the sodium clusters. The signature pattern will emerge as extra middle peaks on top of the original spectrum. Clusters temperature are 20 Kelvin. Ionization laser is 225nm from the OPO laser.	79
59	The upper figure is a mass spectrum using moderate ionization flux, which reflects the real neutral clusters distribution. The bottom figure is a mass spectrum with high photon flux. As one can see the clusters fragment after being ionized and the spectrum can be very different from the original. From Ref. [23].	80
60	We can tune the ionization wavelength so that the mass spectrum of sodium clusters does not depend much on the wavelength of the ionizing light in the 220nm~245nm range. These series of experiments are tuned to a smaller size distribution. Energy flux is about $1 \sim 2 \text{ mJ/cm}^2$	81
61	Average polarizability (per atom) of gas phase sodium clusters at 20 Kelvin. One can see the $1/R$ dependency and on top of it one can observe clear oscillations.	82
62	Polarizability curve with indications of maxima nad minima.	83

63	Our result compares with the earlier higher temperature measurements by Kresin[100] and Knight[58].	84
64	Compare with several theoretical predictions for small sizes, from Manninen[73], Greiner[99] and Kummel[65].	85
65	The suspected shapes of the sodium clusters' delocalized 3s electronic cloud (Na_{1-20}). Figure is reproduced from [32].	87
66	Distortion parameters $\delta = \frac{R_z - R_x}{R_z + R_x}$. Red: the amount which clusters need to deviate away from a sphere in order to account for the oscillation seen in our experiment. The other four: Clemenger-Nillson model with four different parameters U.	88
67	Deformation parameters extracted from the photoabsorption spectrum obtained by Haberland et al with the sodium cationic clusters. Regraphed from [92].	90
68	Polarizability per 3s electron of neutral (dots, from [58]) and charged sodium clusters (Na_x^+ , open circles, [92] and this is also the source of this figure). The plot for neutral clusters has been shifted by one mass, so that clusters with the same number of valence electrons are vertically above one another.	91
69	Experimental polarizability per atom as a function of $\frac{1}{N^{\frac{1}{3}}}$. (This work) . . .	91
70	A theory predicted oscillation in the polarizability curve of alkali clusters (scaled to the bulk polarizability α_{classic}). All clusters are assumed to have a spherical shape. The arrows indicate the opening of a new shell right after a shell closure. From Ref. [86].	92
71	Polarizability ratio curve $\alpha/\alpha_{\text{bulk}}$ from our result and from the spherical jellium theoretical predictions. The $\alpha/\alpha_{\text{bulk}}$ is essentially $(1 + \delta/R)^3$ so this figure gives us an idea how does the spillout scale with the size when compared to the bulk counterpart.	94
72	Experimental separation energy as a function of size from the experiments. The polarizability maxima numbers we observed actually correspond with the minima in experimental shell energy. Figure is regenerated from[17]. . .	95
73	Experimental and theoretical shell energy as a function of size from the experiments. The theory is based on a deformed clusters shape (lower graph)[17].	96
74	Electric dipole moments (EDMs) of neutral sodium clusters.	98
75	EDM of the small sodium clusters (Na_{1-20}) from the theoretical predictions[99].	99
76	EDMs per atom.	99
77	Na_6 cluster profile shows intensity reduction when the field is on (blue) and off (yellow) (this is raw data). If assuming two ground states in the beam and one of them possesses EDM that can be deflected out of the beam, then the thermal population ratio give us the energy difference between the two states $\Delta E = 1.2$ meV. Under the same run, the profiles of Na_5 and Na_7 are plotted in the insets of the figure for a comparison.	101

78	Ionic representation of the two energy isomers of Na_6 from theoretical prediction of [99].	102
79	Another run (ahh series) showing intensity reduction on Na_6 . The intensity ratio gives the enregy different very close to the previous.	102
80	Gold cluster 9 show characteristic beam broadening of an intrinsic dipole moment. Estimated dipole is about 0.42 ± 0.02 Debye. Beam temperature is 33 K.	104
81	Theoretically predicted ionic structure of the two low-lying energy isomers of Au_9 clusters. The energy difference is 80 meV (~ 500 Kelvin). The corresponding dipole moments of 9a and 9b are 0.32 Debye and 1.01 Debye respectively. (Private communication with professor Hannu Haikkinen.) . .	104
82	Sodium typical mass spectrum, with two inset showing left: the distance between on and off peaks in channels, and right: the corresponding polarizability. 106	
83	The width of the field off and field on peak in mm position units. One can see the increase in width as the size gets smaller.	107
84	Mass abundances with different ablation laser wavelengths. Higher photon energy leads to more atoms evaporation and thus higher density and this gives rise to larger cluster size distribution. Other conditions are kept as close as possible.	108
85	Giant resonances for 8-electron clusters $(+)\text{Cs}_8$, $(\times)\text{K}_9^+$, $(\bullet)\text{Na}_8$, $(\circ)\text{Na}_9^+$. The single peak put in evidence spherical symmetry. Source figure from [44] . .	113
86	Photoabsorption cross section of Na_{20} , Na_{92} clusters showing possible volume resonance (shaded region lower graph). Source is from [107].	114

SUMMARY

Rotationally averaged polarizabilities and intrinsic electric dipole moments of sodium clusters are measured and reported. The experimental method is a molecular beam deflection. Our precision is the highest ($<5\%$) and the range of the cluster sizes is the broadest to date ($\text{Na}_{10} \sim \text{Na}_{300}$). Compared to the earlier measurements, our data covers all sizes with no gaps up to the largest cluster. The fine structure in the polarizability curve is previously unobserved. We have carefully ruled out several possible explanations. And we find an earlier existing theory could explain the facts but will lead to magic numbers which were not seen in some previous experiments. A detailed theory is needed to understand the behaviors we see.

Intrinsic electric dipole moments (EDMs) of sodium clusters are probed to answer the intriguing question: Do metal clusters develop electric dipole moments like molecules? Some theories have predicted the existence of EDM in ground state sodium clusters and gave their magnitudes. We put upper bounds on the EDM of sodium clusters and find that they are orders of magnitude smaller than the predictions. This provokes an interesting question: how can one define metallicity in metal clusters?

Our measurements are performed at cryogenic temperature 20 Kelvin. At this temperature the clusters are believed to be in their vibronic ground states.

CHAPTER I

INTRODUCTION

The broadest definition of a cluster is simply an assembly of atoms or molecules. Nonetheless clusters exhibit very unique properties different from those of atoms, molecules and bulk condensed systems. For example, when studying the electronic structure of the metal clusters, physicists discovered certain metal cluster sizes were especially stable, and called these stable clusters “magic number clusters”[59]. Even some non-magnetic bulk materials develop magnetic order when their size becomes small enough, like Rh and Pt clusters[30][71]. Small gold clusters have a special planar structure, contrary to what would be expected from minimization of their surface energy[47]. Also the ‘*shell structure*’ of metal clusters and the analogy with the periodic table suggests the possibility of a cluster chemistry, where metal clusters of different size have different valences. These have been called superatoms, and there is currently much research into the construction of materials using clusters as building blocks[55][89]. These novel physical and chemical properties are always dependent on the length scale of the objects. We can therefore control the grain size to vary the physical and chemical properties of these small clusters. Research on clusters has potential applications in nano-device fabrication, energy development, environmental protection, chemical and medical engineering, and material science.

Though they are different from the bulk in many ways, the cohesive forces that hold a cluster together are essentially the same as those of the bulk. The mechanisms of cluster bonding include van der Waals (noble gas clusters), ionic bonds, hydrogen bonding, and metallic bonding (for alkali and transition metal clusters). The number of the constituent atoms in a cluster in a molecular beam typically ranges from 2 to tens of thousands. The sizes of these objects are in the sub-nanometer to nanometer scale. We sometimes represent clusters as very small miniatures cut from a bulk material. In fact, most properties of bulk do manifest themselves in some form in small clusters, for example, ferromagnetism[16],

phase transitions[43], and plasma resonances[97]. When the length scale or the physical dimension of a object becomes small enough, the energy bands will become discrete (see Figure 5). This leads to novel quantum properties in clusters. In addition, due to the high surface-to-volume ratio at small sizes, surface effects play an increasingly important role in the properties of clusters (e.g. the vibrational spectrum[109]). By studying clusters' characteristics and their variation with size, one can understand the emergence of physical bulk properties starting from a single atom, a task which was previously possible only theoretically.

Historically the term 'clusters' has been used to describe collections of molecules on a surface, complexes existing in a liquid or condensed phase, large inorganic and organometallic complexes, as well as isolated assemblies in the gas phase. The objects we discuss in this thesis are gas phase clusters in a beam where they experience no collisions.

1.1 Metal Clusters

We begin this thesis with a look back into the rich history of metal clusters. The following example is quoted from the book of Ekardt[37] (1999):

The Victoria and Albert Museum in London has on display a glass drinking cup that was manufactured during the later years of the Roman Empire. Its shining colors of red and yellow are an early and very beautiful example of an artistic and commercial application of cluster science. It is also a fine example of how the properties of finely dispersed matter change with size. The 'golden' color of Au changes if the gold particles become small enough.

The glass makers of ancient days did not know, of course, what produced the shining colors, but they knew from experiment that if metal salts were mixed into the hot glass it would result in a brilliant coloration. Metal atoms become mobile in the hot glass, and if they meet during their diffusive motion they will stick together and form that we call today a 'cluster'. The process was employed over the centuries for making colored glass, and is still in use today. It was only



Figure 1: This antique engraved Czechoslovakian glass shows color produced by colloidal suspensions. When gold is in metallic colloidal form, as in the 10-nm-diameter particles in "ruby glass", the "Mie scattering theory" has to be used to explain the unexpected red color illustrated. Ref. www.webexhibits.org

in 1908 that Gustav Mie showed that the beautiful colors are due to resonantly enhanced light-scattering. A microscopic understanding of the process had to wait for the theory pioneered by Ekardt and the experiments of the Knight's group. These seminal works gave new impetus to the field of metal cluster science in 1984.

The above quotation presents a fascinating application of clusters by the ancients. Of course nowadays people can obtain much more colorful stains due to better control on sizes, see Figure 2. This means we can manipulate the properties of a cluster by varying its size.

In a metal cluster the atoms are held together just like the bulk metal, by the delocalization of the valence electrons, or simply metallic bonding. However due to the finite size of a metal cluster, the energy bands become discrete states. This is illustrated in Figure 3 where energy levels of an atom and a bulk material are shown. Metal clusters should appear somewhere in the middle. Due to the surface roughness of these small objects, we can treat this surface disorder as a random perturbation and statistically describe the distribution of energy levels as well as the dependence of this distribution of the particle size[64].

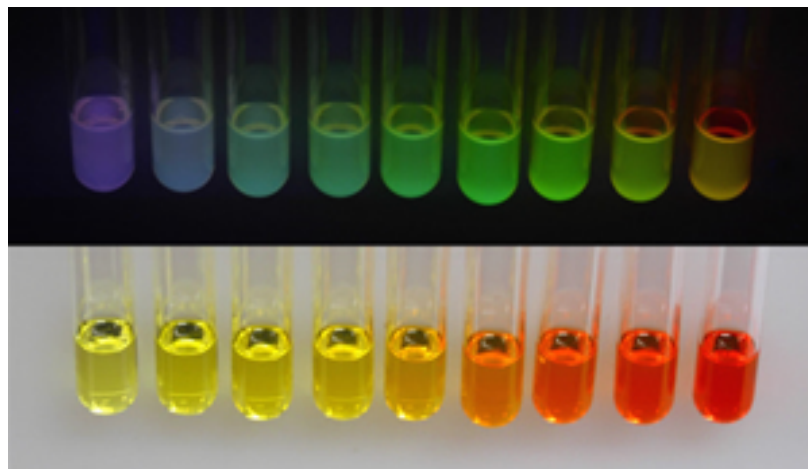


Figure 2: Different sized quantum dot nanoparticles are shown above, first in ultraviolet light and then in ambient light. The length of the synthesis reaction determines particle size. Unlike the metal clusters in the cup these solutions contain semiconductor CdSe clusters. Their size increases from left to right. The color depends on the size. From Ref. www.webexhibits.org

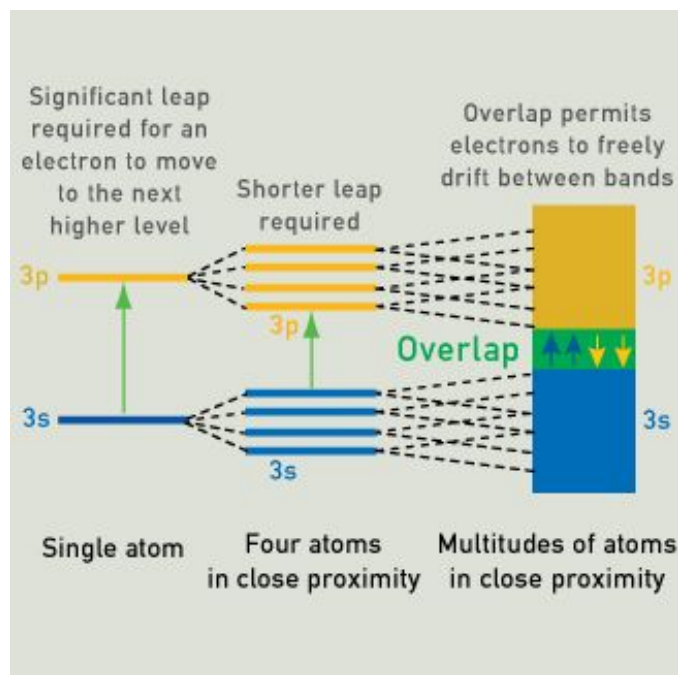


Figure 3: As the number of neighboring atoms increases, the spacing between the energy levels decreases. More overlap occurs and bands of low and high energy replace the distinct energy levels. As more atoms combine, the distance between the two bands decreases, the band gap decreases. From Ref. <http://www.webexhibits.org/>

In 1984 Knight's group discovered important characteristic electronic structures in alkali metal clusters[59] and opened up another era of cluster science. They observed the effect of bunching of energy levels of the free alkali metal clusters in the abundance spectrum, the so-called *electronic shell structure* (See Section 2.3 for an introduction on this effect.). The energy levels resembled those of electrons in a spherical well. In fact there is a close analogy between the energy levels in a cluster and those in a nucleus: the energy levels of a nucleus also organize into shells (will be discussed later in Section 2.3). After this discovery, cluster physics developed rapidly. See [32] for a review. The field is still evolving and progressing today. In this thesis we will carefully examine the interaction of the electronic shell structures with the physical observables we measured.

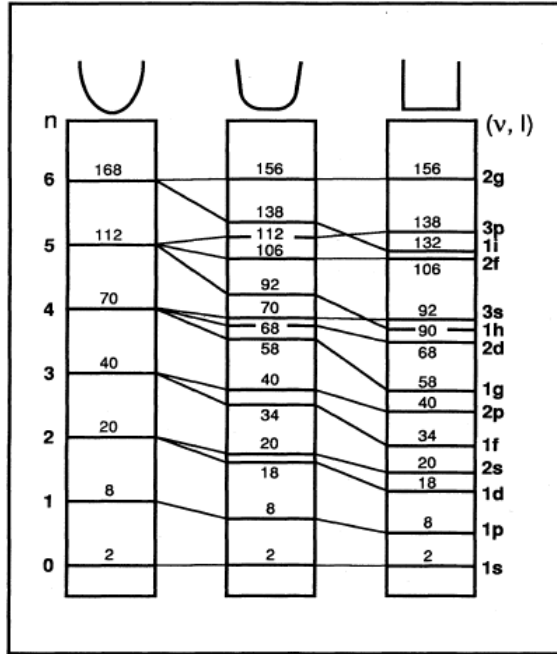


Figure 4: The approximate spherical symmetry of the cluster imposes a DOS with pronounced level bunching. This graph present the electronic levels in three different kinds of central potential that one can approach to the real cluster case. (three-dimentional spherical potential wells). From Ref. [32].

Historically, clusters were first studied when embedded in a matrix (e.g. glass or noble gas matrix) or deposited on a substrate, and this already led to an understanding of the importance of the quantum size effect in metal particles[48]. However in this way one would

not be able to look at the properties of a pure (or bare) cluster, because cluster-substrate or matrix interaction inevitably and uncontrollably distorts the pure particle properties. To study “free” clusters, one has to eliminate all collisions.

Study of free clusters was made possible by development of molecular beam methods, by Stern and Gerlach[41], Rabi[87], Ramsey[88], and the other researchers (see Section 3.3). The conditions of atomic condensation were studied extensively since then, originally for the purpose of avoiding unwanted cluster formation in atomic and molecular beam studies[45]. Now various metal clusters can be reliably and efficiently produced.

Characterizing the dielectric properties is an important step towards understanding the physics of metal clusters. A direct and easy way is to observe the response of a cluster when an external electric field is applied. The response is due to the electric polarizability and susceptibility of the metal cluster. In order to continue the previous sodium cluster polarizability studies, we performed more extended measurements with a better accuracy, a broader size range and a continuous measurement in size. Surprisingly, we had experimentally observed or confirmed, in the polarizability curve of sodium clusters, an earlier theoretical prediction. And we had found that related effects were actually already seen (or revealed itself) in the separation energy of sodium clusters (vacuum evaporation experiment). These will be thoroughly discussed in Chapter 4.1.1.

In the bulk metal, metallicity is defined as absence of gap at Fermi level between the conduction band and valence band. Now we know that the energy discretization of the quantum size effect [QSE] will cause a strong size-dependence energy gap at E_F , with certain well-defined sizes exhibiting substantial gaps. We will show that some metal clusters have non-metallic characteristics. This provokes the questions whether metal clusters possess electric dipole moment or not. Does the screening ability of the delocalized valence electrons still exist under this small size. Here we specifically address this question, whether sodium clusters possess electric dipole moments. These experiments test theories that have predicted large electric dipole moments in the sodium clusters[99].

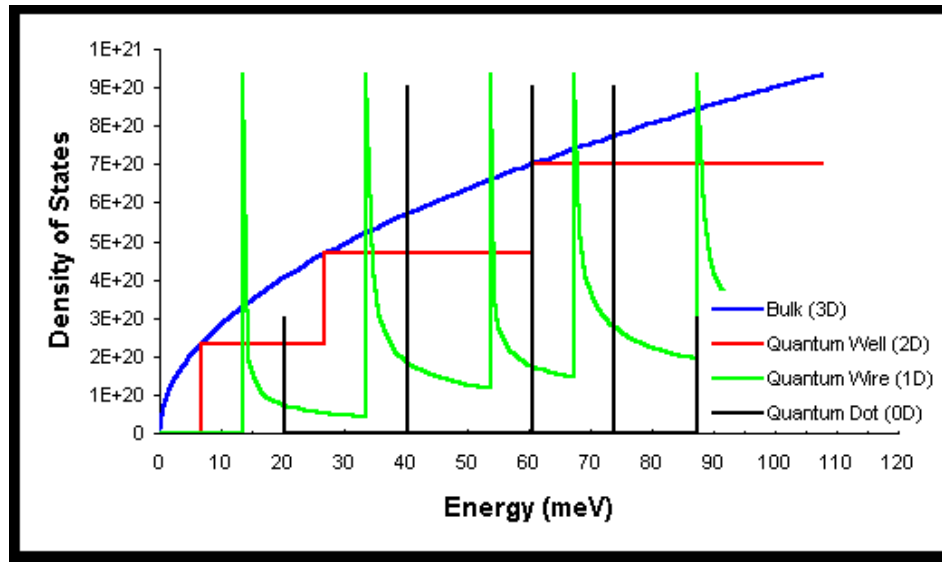


Figure 5: Illustrative energy levels and DOS of bulk, and of three finite small systems: a quantum well(2-dimension), a quantum wire(1-dimension) and a quantum dot(0-dimension), showing the discrete nature of the energy levels. (Wikipedia)

CHAPTER II

BACKGROUND THEORY

2.1 *Classical Conducting Triaxial Ellipsoid*

To understand the rotational averaged polarizability of metal clusters, we need to first introduce the general theory of the polarizability of a metal cluster.

A simple model for the polarizability of a cluster is a conducting triaxial ellipsoid. Lets look at the problem of the induced charge distribution of an ungrounded conducting sphere in an uniform electric external field. This is a classical electrostatics problem that can be solved in many ways. (Laplace's Equation, Method of Images, Greens Function for the sphere, etc.[52][68]) I simply write down the relevant results here. The electric potential can be written as

$$\Phi = -E_0 \left(r - \frac{R^3}{r^2} \right) \cos \theta \quad (1)$$

where R is the radius of the sphere, (r, θ) is the vector position in polar coordinates, and E_0 is external uniform field. The induced surface-charge density is

$$\sigma = -\epsilon_0 \frac{\partial \Phi}{\partial r} \Big|_{r=R} = 3\epsilon_0 E_0 \cos \theta \quad (2)$$

And the total electric dipole p and the corresponding polarizability α in S.I. units

$$p = 4\pi\epsilon_0 E_0 R^3 = \alpha E_0 \quad (3)$$

$$\alpha = 4\pi\epsilon_0 R^3 \text{ (in S.I. units, Cm}^2\text{V}^{-1}\text{)} \quad (4)$$

Note that in cgs units the isotropic polarizability of a conducting sphere is just R^3 .

The energy of a spherical polarizable conductor with induced dipole p is

$$\frac{1}{2}\alpha E^2 = \frac{p^2}{2\alpha} = \frac{p^2}{2 \cdot 4\pi\epsilon_0 R^3} = \frac{p^2}{2 \cdot 4\pi\epsilon_0 \frac{V}{\frac{4\pi}{3}}} = \frac{p^2}{6\epsilon_0 V} \quad (5)$$

where V is the volume. The average electric field created by the induced polarization in the sphere is just

$$E_{\text{induced}} = -\frac{p}{3\epsilon_0 V} = -E_0 \quad (6)$$

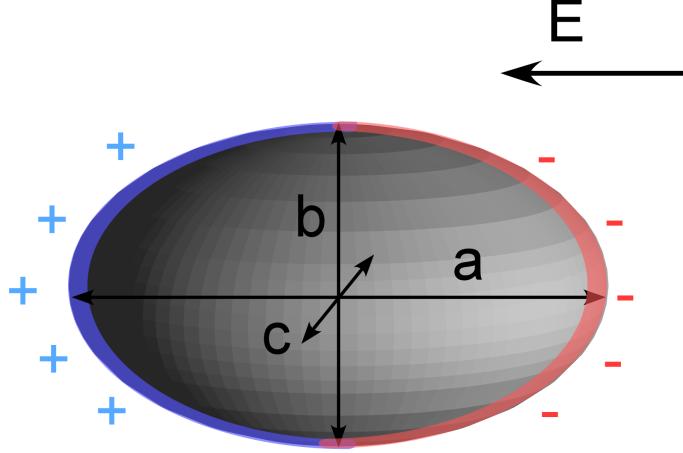


Figure 6: A conducting ellipsoid in an uniform electric field along the longest principal axis a .

What about a conducting triaxial ellipsoid? The generic form of the polarizability of a conducting triaxial ellipsoid along the one principle axis i is [67]

$$\alpha_i = (4\pi\epsilon_0) \frac{abc}{3} \frac{1}{N_i} \quad (\text{in S.I. unit, Cm}^2\text{V}^{-1}) \quad (7)$$

$$= \frac{abc}{3} \frac{1}{N_i} \quad (\text{in CGS unit, Å}^3) \quad (8)$$

where i denotes the x , y , z direction chosen to be the three principle axes, a , b and c are the principal radii of the triaxial ellipsoid, and N_i is the depolarization factor that depends only on the eccentricity of the ellipsoid. (Principle axes are along the eigenvectors of polarizability tensor: these are the axes along which the cluster can rotate freely without experiencing any torque). The depolarization factor N_i has the following integral form

$$N_i = \frac{abc}{2} \int_0^\infty \frac{dt}{(j^2 + t) \sqrt{(a^2 + t)(b^2 + t)(c^2 + t)}} \quad (9)$$

where $j = a, b, c$ in order when $i = x, y, z$. N_i has been calculated and tabulated and can be found in many places[81][6][91][7][5][39]. From the definition one can prove that N_i satisfies

the following relation

$$\sum_{i=x,y,z} N_i = 1 \quad (10)$$

So the induced dipole moment will be (under the body frame coordinate)

$$\vec{p} = \hat{\alpha} \vec{E} = \begin{pmatrix} \alpha_{11} & 0 & 0 \\ 0 & \alpha_{22} & 0 \\ 0 & 0 & \alpha_{33} \end{pmatrix} \begin{pmatrix} E_1 \\ E_2 \\ E_3 \end{pmatrix} \quad (11)$$

One can see that the induced dipole does not need to be in the same direction with the applied field. The off-diagonal contribution in the diagonalized polarizability tensor for metal clusters is generally small and can be taken as zero[24].

For oblate and prolate spheroids ($x = y \neq z$, $a = b \neq c$), N_z can be written as the following analytic expressions

$$N_z = \frac{1 + \varepsilon^2}{\varepsilon^3} (\varepsilon - \tan^{-1} \varepsilon) \quad (12)$$

for a oblate, where $\varepsilon = \sqrt{|a^2 - c^2|}/c \in (0, \infty)$ and $a = b > c$.

$$N_z = \frac{1 - \varepsilon^2}{\varepsilon^3} \left(\ln \sqrt{\frac{1 + \varepsilon}{1 - \varepsilon}} - \varepsilon \right) \quad (13)$$

for a prolate, $\varepsilon = \sqrt{|a^2 - c^2|}/a \in (0, 1)$ and $a > b = c$.

$$N_{i=x,y,z} = \frac{1}{3}, \text{ for a sphere} \quad (14)$$

Here ε is the eccentricity of the ellipsoid. Figures 7 and 8 plot the contribution $\frac{1}{N_z}$ in the polarizability Eq. 7.

The rotational average polarizability α_{avg} is defined as the trace of the polarizability tensor α_{ij} . Along with Eq. 7 α_{avg} is expressed as

$$\alpha_{avg} \equiv \frac{1}{3} Tr(\alpha_{ij}) = \frac{abc}{3} \left(\frac{1}{3} \sum_{i=1}^3 \frac{1}{N_i} \right) \quad (15)$$

We will later show this is the quantity that relates to the experimental observable (as discussed in depth in Section 3.5). Now we look at $\frac{1}{3} \sum_{i=1}^3 \frac{1}{N_i} = \frac{1}{3} \left(\frac{1}{N_x} + \frac{1}{N_y} + \frac{1}{N_z} \right)$ to see the effect of a non-sphericity to the polarizability. They are plotted in Figures 9 and 10. Why the measured polarizability is α_{avg} will be explained later in ch 3.5.

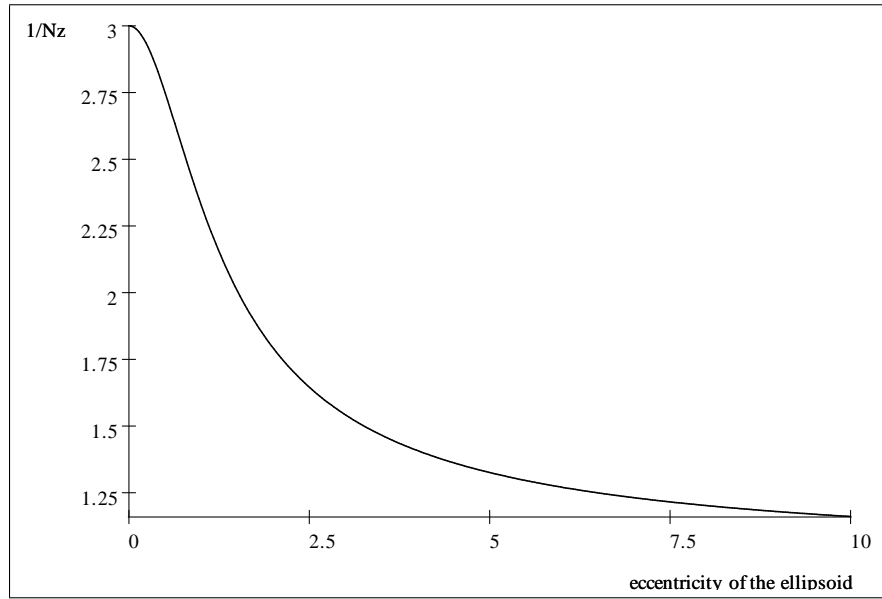


Figure 7: The effect of a geometry depolarization $1/N_z$, for a oblate spheroid.

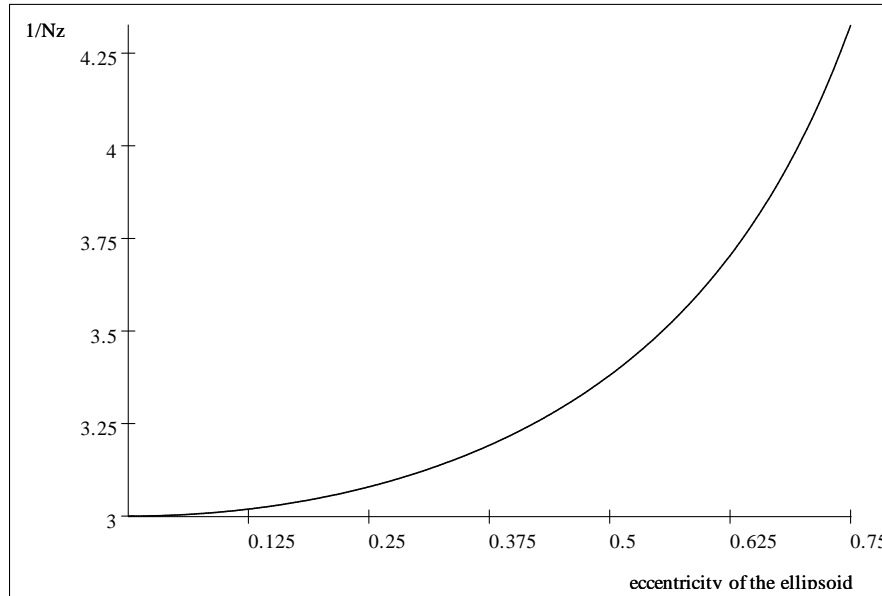


Figure 8: The effect of a geometry depolarization $1/N_z$, for a prolate spheroid.

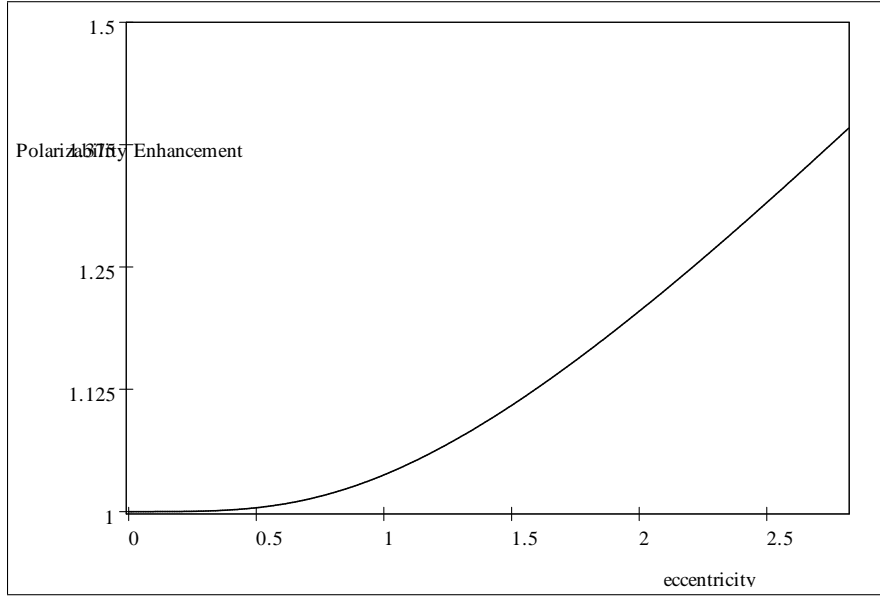


Figure 9: Polarizability enhancement $\frac{\alpha_{oblate}}{\alpha_{sphere}} = \frac{1}{9} \sum_{i=1}^3 \frac{1}{N_i}$, a oblate contribution to the polarizability, assuming volume is fixed.

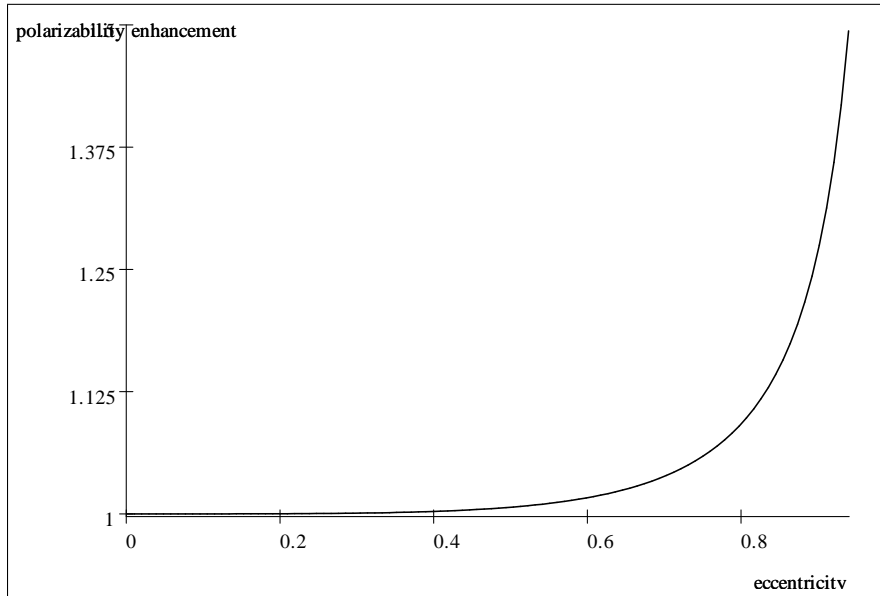


Figure 10: Polarizability enhancement $\frac{\alpha_{prolate}}{\alpha_{sphere}} = \frac{1}{9} \sum_{i=1}^3 \frac{1}{N_i}$, a prolate contribution to the polarizability, assuming volume is fixed.

From this one knows that a deformation away from a sphere can lead to an increase in average polarizability measured in experiment. The amount of increase in the polarizability is related to the amount of deformation of the object. These classical expressions will be further developed and utilized in the following sections.

The depolarization factor is sometimes quoted in the following form[39].

$$N_z = (1 - \gamma^2) \left(1 - \gamma (1 - \gamma^2)^{-\frac{1}{2}} \cos^{-1} \gamma \right), (\gamma < 1, \text{ oblate}) \quad (16)$$

$$N_z = \frac{1}{3}, (\gamma = 1, \text{ sphere}) \quad (17)$$

$$N_z = (\gamma^2 - 1)^{-1} \left(\gamma (\gamma^2 - 1)^{-\frac{1}{2}} \cosh^{-1} \gamma - 1 \right), (\gamma > 1, \text{ prolate}) \quad (18)$$

here γ is the ratio of the longitudinal (polar) axis to the transverse (equatorial) axis $\frac{c}{a}$.

One can also define the distortion parameter $\delta = 2\frac{c-a}{c+a}$, and the polarizability can be expanded as[37][29]

$$a = a_{\delta=0} \left(1 + \frac{4}{9}\delta^2 + O(\delta^3) \right) \quad (19)$$

We will return to this in the Results section to utilize this formula.

For classical *dielectric* ellipsoids one can show the polarizability take the following form

$$\alpha_i = (4\pi\epsilon_0) \frac{abc}{3} \frac{\epsilon - 1}{1 + (\epsilon - 1) N_i} \text{ (in S.I. unit)} \quad (20)$$

where ϵ is the dielectric constant[20][67]. It is therefore no surprise that α_{avg} depends on the geometry of the object; as will be further explained, one can infer that the spatial shape of the screening electron cloud determines to a large extent the value of the static polarizability of a metal cluster.

2.2 Molecular Polarizability and Electric Susceptibility

2.2.1 Harmonic Bound Charges (electrons and ions)

The polarization of a collection of atoms or molecules can arise in two ways:[52]

1. The applied field distorts the charge distributions and so produces an induced dipole moment in each molecule;
2. The applied field tends to line up the initially randomly oriented permanent dipole moments of the molecules.

The first contribution can be approximated by harmonically bound charges. A set of harmonically bound charges e_j with mass m_j has a polarizability

$$\gamma_{mol} = \frac{1}{\epsilon_0} \sum_j \frac{e_j^2}{m_j \omega_j^2} \quad (21)$$

where ω_i are the frequency of oscillation about equilibrium for i th oscillator. This result can be applied to an electron cloud that is bound in a harmonic potential. This is a good approximation for a metal cluster as shown later. For the second contribution, for molecules with a permanent dipole moment p_0 which can be oriented in any direction in space. In the absence of a field, thermal agitation keeps the molecules randomly oriented so that there is no net dipole moment. With an applied field the average dipole moment along the field will be (assume $p_0 E / kT < 1$)

$$\langle p_{mol} \rangle \simeq \frac{1}{3} \frac{p_0^2}{kT} E \quad (22)$$

(for a derivation see Appendix A). The orientation polarization depends inversely on the temperature. In general both types of polarization, induced (electronic and ionic) and orientation, are present, and the general form of the molecular polarization is

$$\gamma_{total} \simeq \gamma_{mol} + \frac{1}{3} \frac{p_0^2}{\epsilon_0 kT} \quad (23)$$

[52]. So the electric susceptibility consists of the polarizability, the Langevin-Debye contribution of dipole moment (second term). An important feature is that this suggest that experimentally we can separate the dipole contribution via the $1/T$ temperature dependence. We will discuss in depth in the theory section.

2.2.2 Quantum Mechanical Description

If we approximate a metal cluster with a harmonic oscillator potential containing many electrons, we can first calculate the single-particle electron wavefunction and find its polarizability. Then similar to Eq. 21 this can be further extended to the polarizability of the entire cluster if we consider the valence electrons to be non-interacting, and if we neglect cluster's core ions polarizabilities. (For a sodium atom the s -electron provides about 98% of the its atomic polarizability.) It can be shown that all possible linear combinations

of the harmonic oscillator single particle eigenstates, properly normalized, give the total polarizability[80].

From a quantum mechanical point of view, the polarizability of a substance is related to the excitation energies of the system (which in a cluster this will depend on shape and size). The following two dipolar sum rules are important when considering the dipole polarizability:

$$W_{-2} \equiv \sum_n (E_n - E_0)^{-2} |\langle 0 | z | n \rangle|^2 = \frac{\alpha}{2e} \quad (24)$$

$$W_0 \equiv \sum_n (E_n - E_0)^0 |\langle 0 | z | n \rangle|^2 = \frac{N\hbar^2}{2m} \quad (25)$$

where W_p is the p th moment of the dipole oscillator strength $|\langle 0 | z | n \rangle|^2$ for a system with ground state $|0\rangle$ and excited state $|n\rangle$. The second sum rule is the well-known Thomas-Reiche-Kuhn sum rule for oscillator strengths for N electrons.

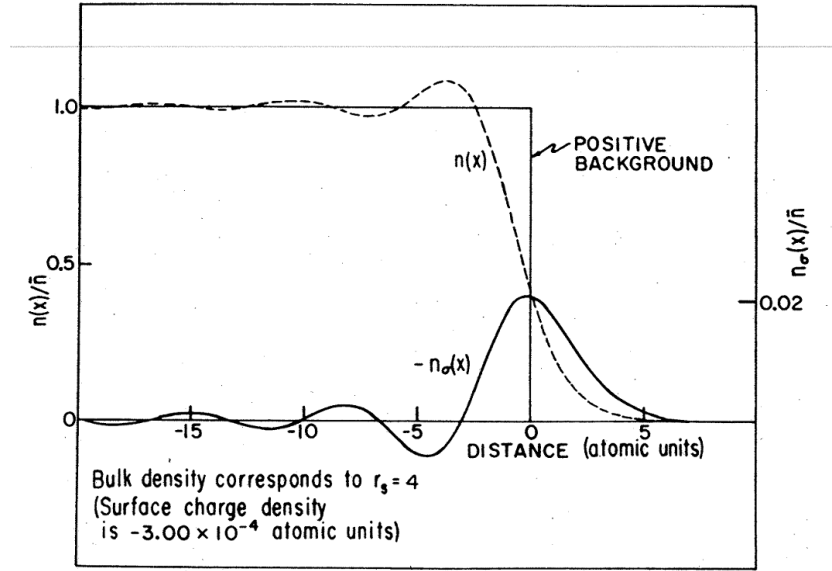


Figure 11: Metal surface charge density simulation by Kohn and Lang[69]. Graph showing charge density without external electric field $n(x)$ and induced charge density distribution $-n_\sigma(x)$ with external electric field. One can clearly see the enhancement of electron spillout due to the screening of electron clouds at the surface. From Ref. [69].

On a bulk metal surface, the electron charge density has been well studied and understood. We know that the electrons always extend beyond the metal surface to some extent (this is called an electron spillout) and inside the metal the charge density has an

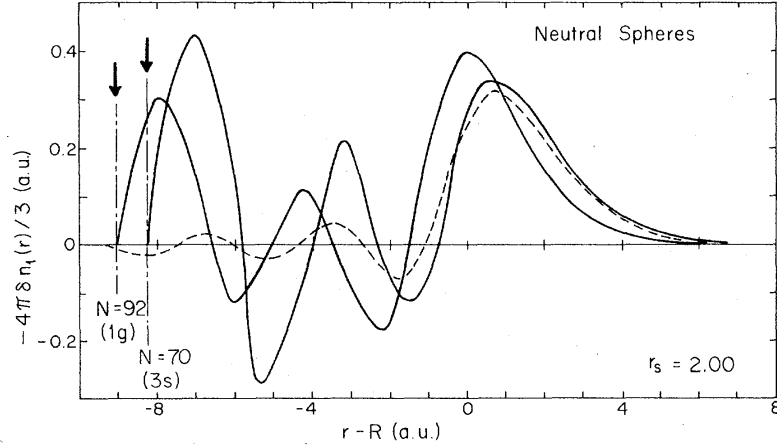


Figure 12: Predicted perturbed dipole density $-n_d(x)$ for neutral spheres with $r_2=2$ containing $N=70$ and 92 electrons. The dashed curve is the corresponding perturbed density for a plane surface. One can tell that the Friedel oscillation is altered from the bulk surface (dash line) due to finite size effect. From Ref. [11].

oscillating component (Friedel oscillation)[52][70]. (See Figure 11) With an external electric field presents, the electron spillout will also response to the field and this gives rise to the enhancement in the polarization. We will show later, as the size of the bulk metal becomes smaller, the electron spillout will further be modified due to the quantum size effect[11]. Figure 12 illustrates the perturbed charge densities of two neutral spheres with different number of electrons compared with that of a metal surface. Clearly a classical picture of a conducting sphere or triaxial ellipsoid is not enough to explain the experimental results for small clusters. One has to take the electron spillout and the quantum mechanical effects into account[11][36][86]. A good approximation is to treat the electronic spillout as a function of size $\delta(N)$, with N the number of atoms. Assuming a conducting alkali metal cluster with a spherical shape with N metal atoms the polarizability can be written as $\alpha(N) = 4\pi\epsilon_0 (R + \delta)^3$ where R is the classical radius. So the polarizability is enhanced due to the electronic spillout δ . We will come back to this point later, but first if we assert this, then following Eq. 20, for a dielectric triaxial ellipsoid, the polarizability can be written as [57][20]

$$\alpha_i = (4\pi\epsilon_0) \frac{(a + \delta)(b + \delta)(c + \delta)}{3} \frac{\epsilon - 1}{1 + (\epsilon - 1)N_i} \text{ (S.I.)} \quad (26)$$

If a physical property depends on its surface, then as the size gets smaller, surface-to-volume ratio $\frac{S}{V}$ becomes larger. For a sphere with radius R , the physical property per atom will be proportional to $\frac{4\pi R^2}{\frac{4}{3}\pi R^3} \sim \frac{1}{R}$. So this physical property can be expected to scale inversely with the size. As shown later, the polarizability per atom of metal clusters we are interested in essentially follows this global trend.

2.2.3 Electric Susceptibility and Electric Dipole Moment (EDM)

The relation between the macroscopic electric displacement D and polarization P is

$$D = \epsilon_0 F + P = \epsilon F \quad (27)$$

where F is the static external electric field. The polarization P can be expressed as

$$P = \epsilon_0 \chi_e F \quad (28)$$

and this defines the electric susceptibility χ_e of a substance. So the dielectric constant $\epsilon = \epsilon_0 (1 + \chi_e)$. Here F and P is the macroscopic average fields and dipole density. We use the continuum approximation for the dielectric material and neglect atomic-scale behaviors as is usually done. Next, the Clausius-Mossoti relation relates the macroscopic polarizability α of a substance to its dielectric constant ϵ through

$$\alpha = V \frac{4\pi}{3} \frac{\epsilon/\epsilon_0 - 1}{\epsilon/\epsilon_0 + 2} = V \frac{4\pi}{3} \left(\frac{\chi_e}{\chi_e + 3} \right) \quad (29)$$

For a conductor $\chi_e \rightarrow \infty$, so that α becomes $V \frac{4\pi}{3} \sim R^3$.

Alternatively one can also start from the perturbation theory of the Stark effect: one applies an external, static electric field \mathbf{F} and expands the total energy E_{stark} up to second order in \mathbf{F} . The coefficient of the quadratic term is the polarizability.

$$E_{stark}(\mathbf{F}) = \underbrace{(\nabla_{\mathbf{F}} E_{stark}) \cdot \mathbf{F}}_{\vec{p}_0} + \frac{1}{2} \underbrace{(\nabla_{\mathbf{F}} \nabla_{\mathbf{F}} E_{stark}) \cdot \mathbf{F}^2}_{\vec{\alpha}} + \dots \quad (30)$$

This energy shift due to the external electric field is the Stark energy. The first coefficient of the linear field correspond to the permanent electric dipole moment of the medium. The second coefficient is the polarizability tensor of the media which gives the induced electric

polarization. If we take first derivative with respect to the field, we will get the total electric dipole moment

$$\frac{dE_{stark}}{d\mathbf{F}} = \vec{p} = \vec{p}_0 + \vec{\alpha} \cdot \vec{F} + \frac{1}{2} \vec{\beta} : \vec{F}^2 + \frac{1}{6} \vec{\gamma} : \vec{F}^3 \quad (31)$$

The electric polarization P is equal to the electric susceptibility χ times F . When there is no permanent electric dipole, P is usually expressed as a Taylor series in F whose coefficients will include the nonlinear susceptibilities:

$$\frac{P_i}{\epsilon_0} = \sum_j \chi_{ij}^{(1)} F_j + \sum_{jk} \chi_{ijk}^{(2)} F_j F_k + \sum_{jkl} \chi_{ijkl}^{(3)} F_j F_k F_l + \dots, \quad (32)$$

where $\chi^{(1)}$ is the linear susceptibility, $\chi^{(2)}$ gives the Pockels effect, and $\chi^{(3)}$ gives the Kerr effect. In our case we only need to consider the linear term, because the higher order terms are only important in very intense electric field application and will be more suitably described in the field of nonlinear crystal optics. In a homogeneous linear and isotropic dielectric medium, the polarization is aligned with, and proportional to the electric field F . In an anisotropic material, the polarization and the field are not necessarily in the same direction. Then, the i th component of the polarization is related to the j th component of the electric field, and the medium is nonlinear. So in this thesis we only consider the linear response of the susceptibility and isotropic polarization, which is an excellent approximation.

The susceptibility is also a function of the frequency ω of the applied field. When the field is an arbitrary function of time t , the polarization is a convolution of the Fourier transform of $\chi(\omega)$ with the $F(t)$. This reflects the fact that the dipoles in the material cannot respond instantaneously to the applied field, and causality considerations lead to the Kramer's-Kronig relations which relate real and imaginary parts of χ . In this thesis, static field is used so $\omega = 0$. This is an excellent approximation for frequencies ω well below the plasma frequency. (When the cluster enters the field, however, it does experience a ramping fringe field, we will turn back to this in the experiment section.)

In a quantum description, first order perturbation gives the permanent dipole moment

$$\langle \vec{p} \rangle = \langle \psi^0 | \vec{p} | \psi^0 \rangle \quad (33)$$

where ψ^0 is the ground state wavefunction. For tops with inversion symmetry it vanishes thus they do not possess first order Stark effect in ground state. S -state atoms in its ground

state have this property and thus element atoms can not possess any permanent electric dipole moment[25].

In second order this gives the polarizability tensor

$$\alpha_{ij} \equiv -2 \sum_{k>0} \frac{\langle \psi_k^0 | p_i | \psi_0^0 \rangle \langle \psi_k^0 | p_j | \psi_0^0 \rangle}{E_0^{(0)} - E_k^{(0)}} \quad (34)$$

$$E_{stark}^{(2)} = -\frac{1}{2} \sum_{i,j=1}^3 F_i \alpha_{ij} F_j \quad (35)$$

where ψ_k^0 , $E_k^{(0)}$ are the k th order unperturbed wavefunction and eigen-energy respectively.

The definition of the electric dipole moment (EDM) is $p = \int r \rho(r) dV$ where r and ρ are the position and density of the charges. The unit of EDM is the electronic charge unit times the length unit. The electronic charge unit in cgs system is statcoulomb (statC) or franklin (Fr) or electrostatic unit of charge (esu). So the unit of EDM can be in statC·m, esu·Å, Coulomb·meter (SI) or Debye. The relations between different units are given below

$$1 \text{ statC} = 1 \text{ esu} = 1 \text{ Fr} \quad (36)$$

$$1 \text{ Coulomb} = 10 \times (\text{speed of light}) \text{ statC} \quad (37)$$

$$1 \text{ statC} = 1 \text{ esu} = 3.33564 \times 10^{-10} \text{ Coulomb} \quad (38)$$

$$1 \text{ Debye} \equiv 10^{-10} \text{ statC} \cdot 1 \text{ Å} = 3.33564 \times 10^{-30} \text{ Coulomb} \cdot \text{meter} \quad (39)$$

In cluster science EDM is conventionally expressed in Debye. The definition of Debye is the dipole moment magnitude of 10^{-10} statC charges separated by 1 Å. Typical dipole moments for simple diatomic molecules are in the range of 0 to 11 Debye. The charge anisotropy in the water molecule cause it to possess a dipole moment of 1.85 Debye. Electric beam deflections of water molecules have been measured by Kresin[79]. Gas phase potassium bromide, KBr, has a dipole moment of 10.5 D. Homonucleus ozone molecule O₃ has a dipole moment of 0.53 Debye (see Figure 13). The expectation value (physical observable) of EDM of a polar molecule in its ground state, without external field, is always zero due to the rotational symmetry in its ground state wavefunction. In order to observe the EDM we need to apply an perturbed external field[25].

Can homonucleus *metal* cluster possess electric dipole moment like molecules do? In a neutral metal cluster, if the cluster lacks inversion symmetry, it seems possible to have

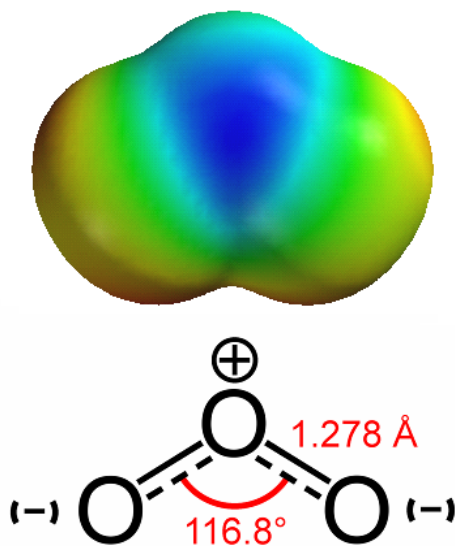


Figure 13: Color representation of the electronic charge transfer of the homonucleus molecule ozone.(upper figure) Due to its sp^2 hybridization bonding nature of the center atom (lower figure), it is a polar molecule with a dipole moment of 0.5337 D. From Ref. Wikipedia.

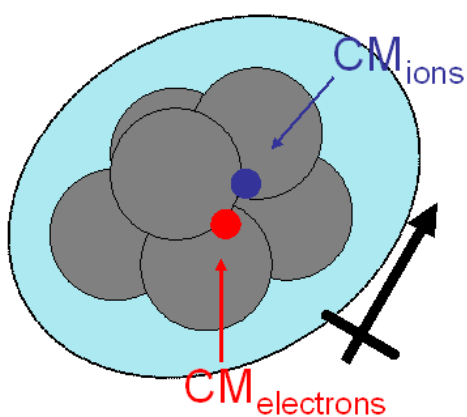


Figure 14: An guessed illustration of the center of masses of the electron cloud and of the ionic cores for a metal cluster.

different center of masses for the delocalized electron clouds and for the core ions

$$p = \int r \rho(r) dr \quad (40)$$

$$= \int r_+ \rho_+(r_+) dr_+ + \int r_- \rho_-(r_-) dr_- \quad (41)$$

$$= r_{\text{ions}}^{CM} \times (+Q) + r_{\text{electrons}}^{CM} \times (-Q) \neq 0 \quad (42)$$

after minimizing their total energy. This will lead to an electric dipole moment. Professor Greiner etc. had theoretically predicted the existence of EDM in alkali sodium metal clusters in their ground state[99], using all-electron ab initio theoretical method based on the Hartree-Fock approximation, density functional theory, and perturbation theory. The results are replotted in Figure 15. In the bulk phase the delocalized electrons screen electric fields (Thomas-Fermi screening)[56]. It will be interesting to know to what degree the metal cluster inherent this screening property from the bulk metal. In other words, how does the metallicity of metal cluster develop as the size gets smaller and how does it relate to the screening effect?[31]

2.3 Electronic Shell Structure and Magic Numbers of Simple Metal Clusters

The polarizabilities of metal clusters depend on their electronic structures. So first we discuss the electronic shell structure of simple metal clusters. Simple metals include the alkalis. In the bulk, these are the so-called free (or nearly-free) electron metals. It is found that the outer-shell valence electrons form a delocalized sea of conduction electrons, with a characteristic approximately spherical Fermi surface. Their interaction with the lattice of the remaining ion cores can be ignored to a good approximation or taken into account by means of a residual pseudopotential.

In simple metal clusters the same electron-delocalized phenomenon in general occurs: the electrons delocalize to form an electron cloud. The motion of the delocalized valence electrons is reminiscent of a particle in a box quantum mechanical problem. When we confine electrons into a specific three dimensional potential well, we can solve the Schrödinger equation for the eigenenergies, as is shown in Fig. 18 with three different types of potential

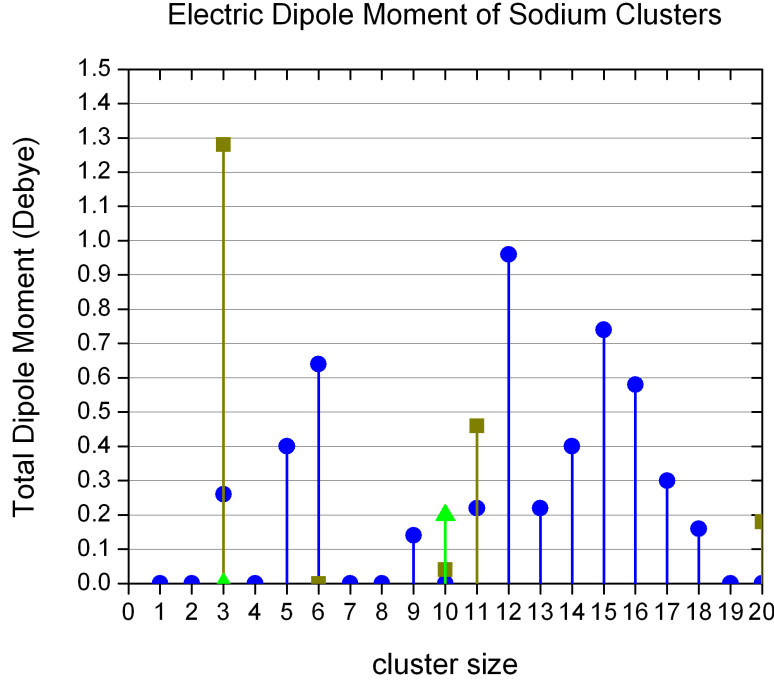


Figure 15: Dipole moments of the optimized ground state neutral sodium clusters (blue circle) as a function of cluster size calculated by the DFT method[99]. For some clusters, more than one isomer has been considered (green square and yellow triangle). Figure is regenerated from [99].

wells: harmonic, intermediate and square well. Also shown in Fig. 18 is the degeneracy of each angular state or level. The model predicts that when a degenerate energy level is fully filled with electrons (a closed shell), the cluster will be more stable compared to the open-shell ones (not fully filled with electrons), similar to the atomic discrete energy levels where the noble gases are most stable when considering their chemical properties. This effect has been experimentally observed[56]. As mentioned before, clusters with an energy level filled with electrons (a full shell) are called “magic numbers” clusters. This simple metal cluster property is the “electronic shell structure”. Electronic levels in simple metal clusters closely represent the eigenenergies of an intermediate (between harmonic and square) potential well.

There is a strong and intriguing analogy between the physics of a metal cluster and that of a nucleus. In a densely packed nucleus, a nucleon moves in an effective potential created by all the forces of the other nucleons. This leads to energy levels resemblances to those

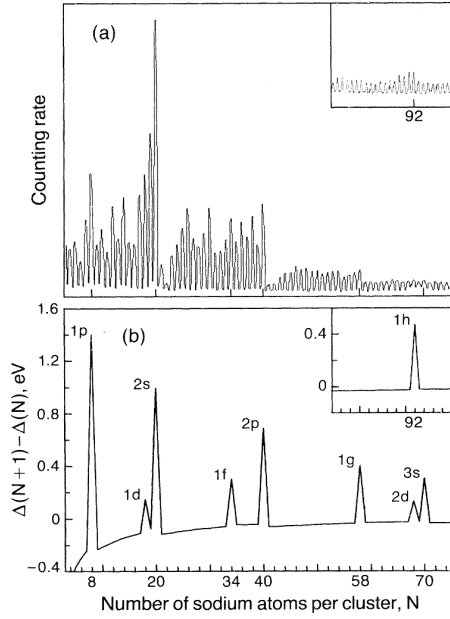


Figure 16: Upper figure: high temperature mass spectrum of sodium clusters. Magic-number clusters are more abundant (more stable) than the others. Bottom figure: theoretical prediction. From Ref. [59].

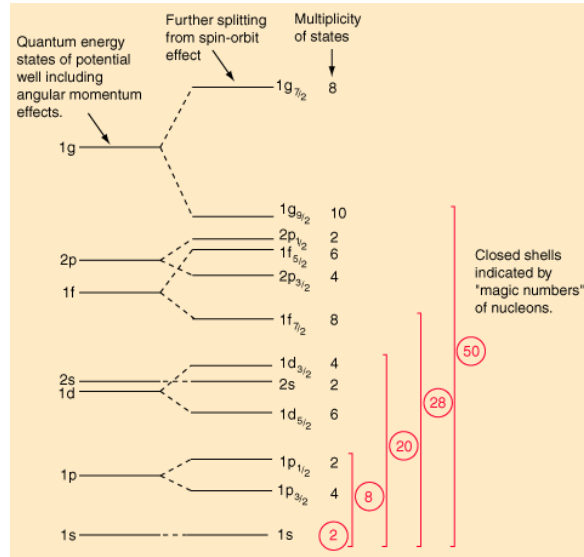


Figure 17: Low-lying energy levels of a nucleus in a single-particle shell model with a modified oscillator potential without spin-orbit (left) and with spin-orbit (right, the Nilsson model) interaction. The number to the right of a level indicates its degeneracy, $(2j+1)$. The boxed integers indicate the magic numbers. Figure's source: Hyperphysics.com.

discrete energy levels in a square well or a harmonic oscillator potential in a metal cluster. See Figure 17. In a metal cluster, similar effect occur, each valence electron sees an effective potential created by all the other valence electrons and all the core ions, and as a result shell structure in the energy levels forms. In both cases we are dealing with a finite-sized system of identical Fermi particles in a quantum well.

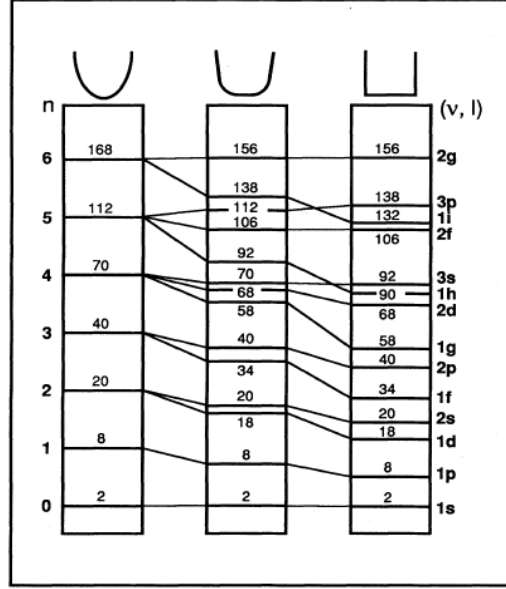


Figure 18: Energy level quantization for electrons confined in three different kinds of central potential (harmonic, intermediate and square wall three-dimensional spherical potential wells). A metal cluster's energy levels actually resemble this. From Ref. [32].

The electronic shell structure was discovered in experimental mass abundance spectra in sodium clusters [59], where a shell structure causes close shell clusters to be more stable than others. (Please refer to Figure 16) Notice that the high intensities or counts corresponding to the closed shells clusters occur at 8, 20, 40 and 58. A theoretical prediction of the mass spectrum is also in the figure.

Later, evidence of the shell structure was also found in the mass abundance spectra of potassium[58], copper, silver and gold[54]. Bjørnholm was able to confirm that all magic numbers were found for $N \leq 1000$ [17]. In 1991, TP Martin was able to take mass spectra for sodium clusters for up to 22000 atoms, with the remarkable result that all magic numbers $N \leq 15000$ could be explained within the framework of the electron confinement model[83].

It is only for even larger N that mass anomalies could be related to atomic rearrangements (Page 9 in [37]).

Table 1: Experimental observed magic numbers and the theoretical prediction.

Experiment					Theory (Na)	
Shell n	Ag	Au	Cs	Na	Wood-Saxon	Jellium LDA
0	2	2	2	2	2	2
1	8	8	8	8	8	8
2	20	20	18/20	20	20	18/20
3	40	34	34/40	40	40	34/40
4	58	58	58	58	58	58
5	92	...	92	92	92	92
6	138	...	138	138	138	138
7	(198)	...	198 \pm 2	196	198	186/196
8			263 \pm 5	260 \pm 4	254/268	254
9			341 \pm 5	344 \pm 4	338	338
10			443 \pm 5	440 \pm 2	440	440
11			557 \pm 5	558 \pm 8	562	556
12			700 \pm 15		694	676
13			840 \pm 15		832	832
14			1040 \pm 15		1012	

Experimentally observed magic numbers of several metal clusters are shown in Table 1. The table is regenerated from [18][17]. Just as in the nuclear case, when compared with the theoretically predicted magic numbers (for the intermediate potential), we immediately observe correspondences and also some discrepancies. For instance, between $N = 58$ and $N = 92$ there should be more shell closings ($N = 68$ or 70), and between $N = 92$ and $N = 138$ there should be another shell closings ($N = 106$). They actually do not produce magic numbers in the abundance experiment. This gave rise to the conclusion that the closing of a spherical shell is a necessary but not sufficient condition for the existence of magic numbers[17]. In fact, Bjørnholm proposed each spherical shell comprises several l values and a new shell closing only appears whenever the radius of the cluster has been increment by a characteristic length, equal to about 0.5 times the Wigner-Seitz radius[17]. Besides, the positions of shell closings may vary from one element to the next.

The ionization potentials (IPs) also show a transition from atomic to bulk-like behavior. Measurements of IPs in sodium, potassium [60] and also silver [1] show high values for small clusters and a downward trend towards the bulk work function as size increases(which is the

bulk limit). See Figure 19. More importantly it shows the size dependent variations that can be interpreted by considering the electronic shell structure. The main lesson learned from the study of these simple metal clusters is that electronic properties are dominated by the delocalized valence electrons.

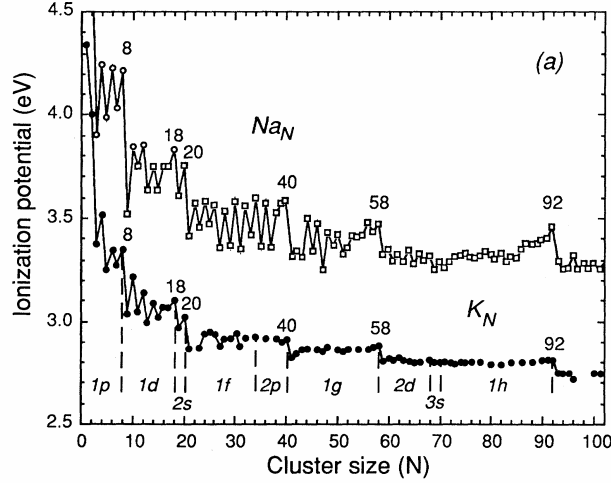


Figure 19: Ionization potentials measurements on sodium and potassium clusters reveals the electronic shell structure. The general trend gradually decreases as a function of size and approaches the bulk work function. From Ref. [32].

Similar evidence of shell structure is found in polarizability of alkali clusters and this will be discussed in this thesis (see Figure 61 and discussion therein).

2.3.0.1 Van der Waals clusters

It is worth mentioning some other 'magic numbers' in cluster science. They appear in the clusters whose constituent atoms are bonded by weak van der Waals forces. This includes the noble gas clusters (Ar_N , Kr_N , Xe_N), C_{60} fullerene clusters $(\text{C}_{60})_N$ and aggregates of closed shell molecules, like $(\text{I}_2)_N$, $(\text{N}_2)_N$, $(\text{CO}_2)_N$ and $(\text{SF}_6)_N$. The bond strength is about 0.1 eV per atom. (Compared to metal cluster's binding energy of $\sim 1\text{eV}$ per atom.) Due to the weak force the clusters can be modeled by central pair forces and because of this the most stable cluster structures are those with high atomic density, with a close packing arrangement in structure. This includes the well-studied MacKay icosahedral family shown in Figure 20. The icosahedron packing nature of Van der Waals clusters had been experimentally

confirmed[50][2][53]. Scientist have found evidence of icosahedron packing nature of ions in metal clusters[93][43][46][84]. And we will carefully look for evidence of this kind in our polarizability measurements of sodium clusters.

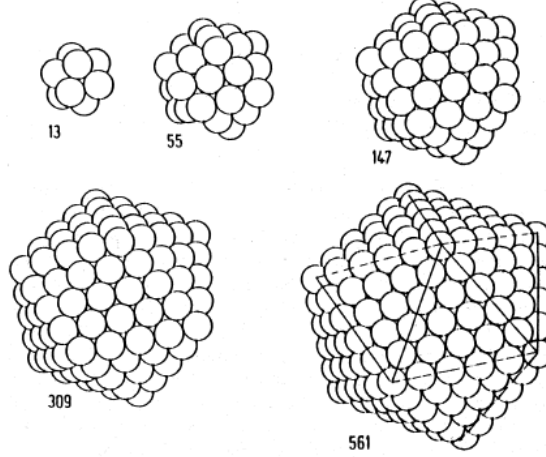


Figure 20: In 1962, Mackay presented a family of icosahedral structures as 'a dense non-crystallographic packing of equal spheres'. In his report, Mackay showed that clusters containing certain 'magic numbers' of identical atoms may form compact, nearly spherical structures with surfaces that are nearly close-packed. Each of these icosahedral structures is composed of 20 fused, distorted tetrahedra. From Ref. [72].

The Van der Waals weak interaction can be modeled using the Lennard-Jones potential

$$V_{LJ}(r) = \zeta \left[\left(\frac{r}{r_0} \right)^{-12} - 2 \left(\frac{r}{r_0} \right)^{-6} \right] \quad (43)$$

where ζ is the depth of the potential well. The long range attraction r^{-6} part is from the induced dipole - induced dipole interaction.

2.4 *Earlier Works on Polarizability and EDM of Sodium Metal Cluster*

2.4.1 Static Dipole Polarizability

Static Dipole Polarizability is one of the most straightforward dielectric properties that can be measured using the beam deflection methods. Electric beam deflection measurement of free alkali metal atomic clusters have been performed by two groups[100][4]. There are other indirect methods to extract cluster polarizabilities, such as; photo-absorption[92], and

PES (photoelectron spectroscopy)[10]. We will compare our result with these measurements later on. The earlier results are collected and graphed in Figure 21.

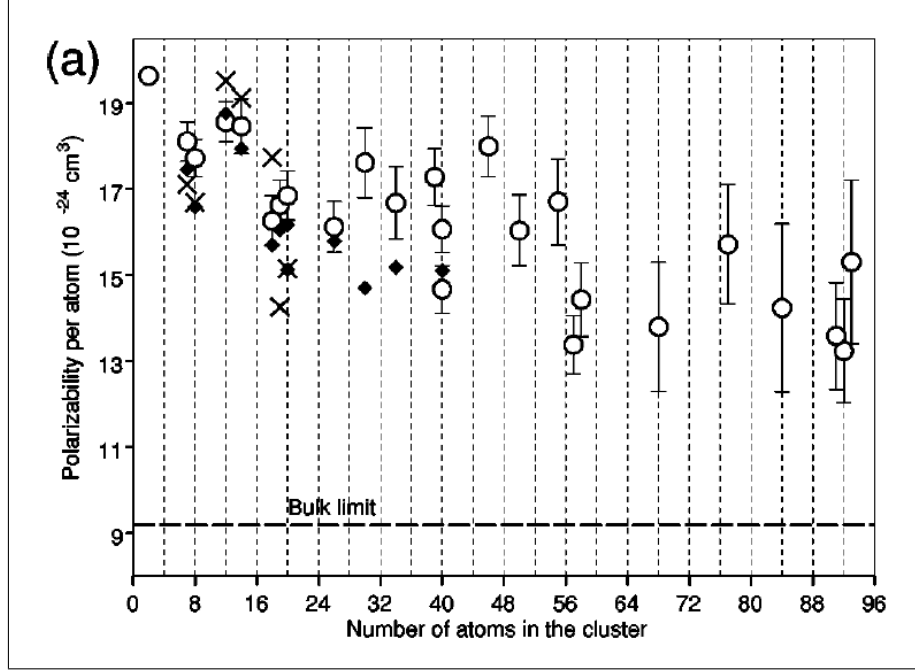


Figure 21: The previously measured $\bar{\alpha}$ is plotted. Figure is a courtesy from [100] (A oven cluster source. Vapor temperature 873 K. Argon carrier gas with a pressure of 600-620 kPa. Nozzle diameter is $75 \mu\text{m}$ (with supersonic expansion) and temperature of clusters is measured to be 1093K.)

The previous theoretical calculations of the polarizabilities of alkali clusters outnumber those of the experiments. For a review on the theoretical works, see [20][22]. Earlier polarizability theory tends to underestimate the experimentally measured values. Various corrections have been proposed to deal with these discrepancies, but the discrepancies remain unresolved. Recent theoretical work has addressed the possibility of a strong influence of metal cluster temperature on the polarizability[19][65]. However this still needs an experimental test.

In the current work, with an extended size range, better precision, and a continuous measurement in size, we further observed several unpredicted features. The polarizability per atom versus the size, that we will present, shows new well-defined oscillations which are not resolved previously. Besides, the local minima and maxima corresponds to the

magic numbers predicted simply by the spherical jellium model[86][35]. This suggests that the spherical electronic shell structure actually dominates the polarizability and causes oscillations between specific minima and maxima.

The polarizabilities of the element atoms from the periodic table is plotted in Figure 22. As explained in atomic physics the polarizability of the element with same principal quantum number is the largest when a new shell is starting to fill (the alkalis). This can be seen in the figure as the high values in polarizability. While adding one more proton, the nuclear charge of the atom will increase. An increased nuclear charge means the nucleus attracts the same energy level electrons more to it hence the extent of the electrons cloud of the atom decreases. This will go on until the next electronic level is reached. The electronic structure is also seen in the IPs of the element atoms (Figure 23).

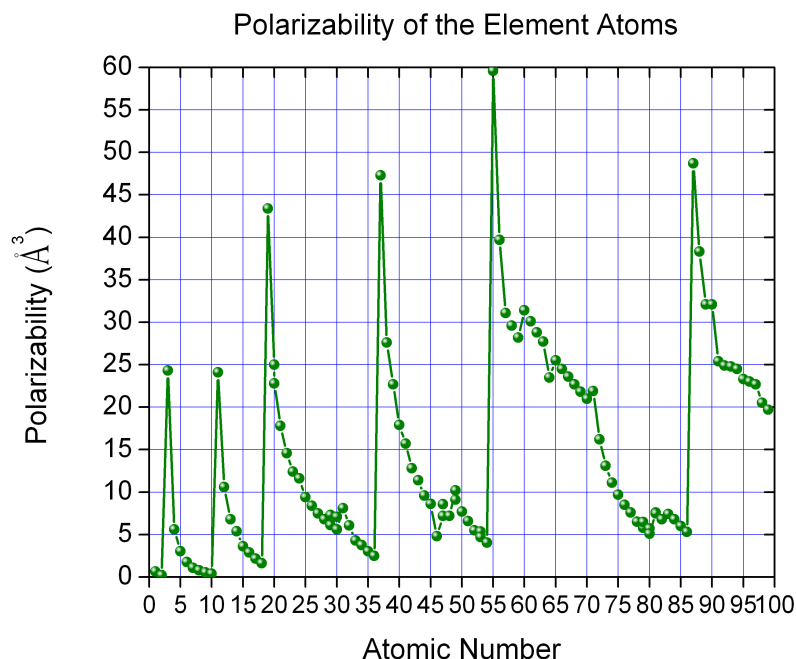


Figure 22: Polarizability of all the elements on the periodic table. The trend can be explained by considering the radius of the atom. Generally speaking, as the atomic number increases along each row of the periodic table, the additional electrons go into the same outermost shell; whose radius gradually contracts, due to the increasing nuclear charge. In a noble gas, the outermost shell is completely filled; therefore, the additional electron of next alkali metal will go into the next outer shell, accounting for the sudden increase in the atomic radius. (The increasing nuclear charge is partly counterbalanced by the increasing number of electrons, a phenomenon that is known as shielding; which explains why the size of atoms usually increases down each column.)

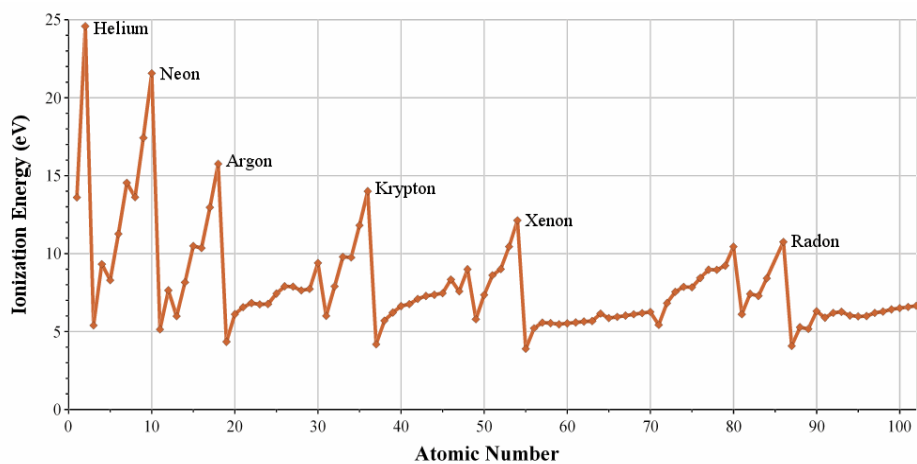


Figure 23: Ionization potentials of all the elements.

CHAPTER III

EXPERIMENTAL SETUP/METHODS

Clusters have been studied with various techniques. Free clusters in the gas phase have the advantage of being isolated from any substrate and remain in a non-interacting state, so the intrinsic properties of the pure cluster can be investigated. The well developed molecular beam methods allow us to probe the free clusters with no interactions except for our probe. This aspect is important to fundamental physics because it serves as a great test bed to examine existing theories. We will describe the key components of the molecular beam method and its basic principles.

3.1 Molecular Beam Method

Deflection experiments on a atom beam can date back to Stern-Gerlach (SG) experiments of 1920s[41], where different spin states of silver atoms split in an inhomogeneous magnetic field. In similar principles, atomic cluster beam formation was observed in 1956 using a low-temperature supersonic hydrogen beam [BEC'56]. Here instead of sending a beam of silver atoms through a magnetic field, we send a beam of atomic clusters through an electric field.

The apparatus and its main components are displayed in Figure 24. The principles of the experiment are briefly described here and each component is discussed in detail in the following sections. A neutral cluster is produced in a source and is sent through an inhomogeneous electric field. The cluster deflects due to the electric field. The electric field causes polarization. The resulting dipole then interacts with the field gradient which exerts a force on the cluster and deflects it.

The deflection is measured and we extract the cluster's electric polarizability. The detection of the deflection will be discussed in Section . In reality an ensemble of clusters

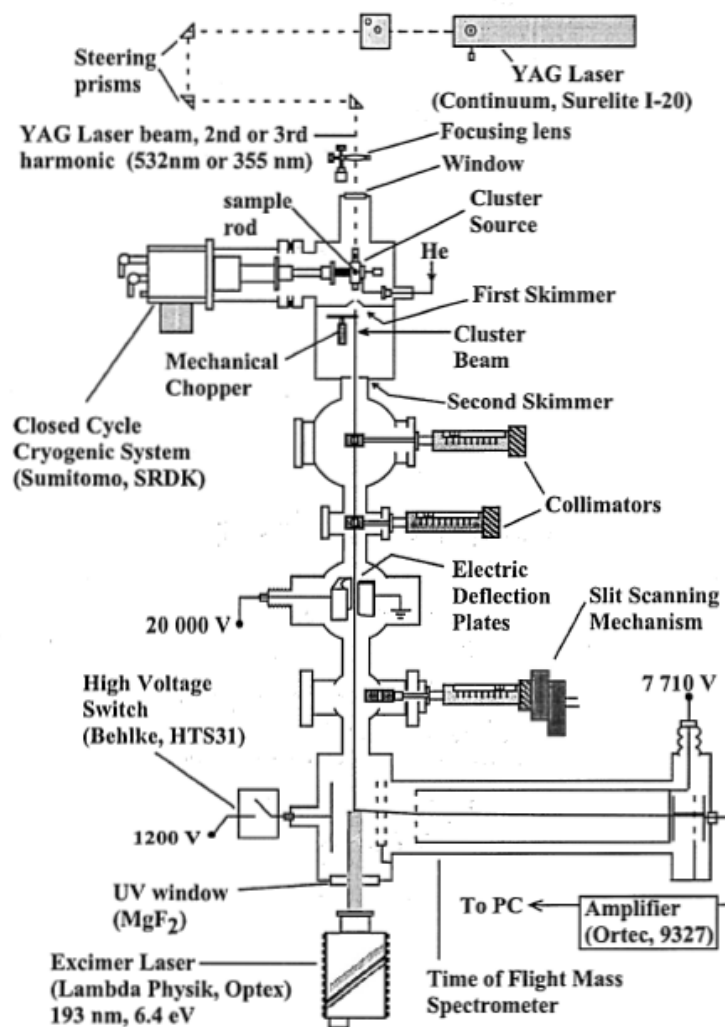


Figure 24: A look at the whole apparatus. From Ref. [80].

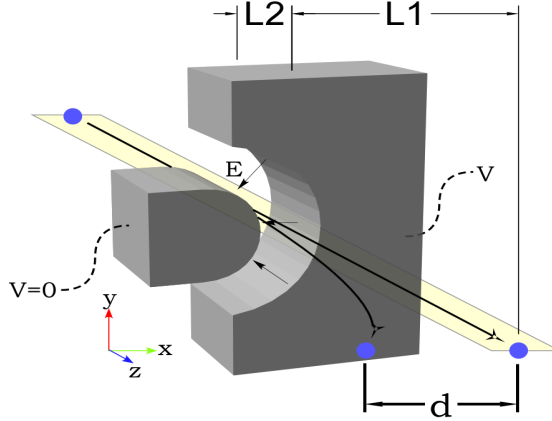


Figure 25: Schematic of the trajectories of a free cluster when it passes through the inhomogeneous electric field. (field on and field off; the deflection is d .)

is used to increase the intensity. Now we explain each component of the apparatus.

3.2 *The Production of Gas Phase Clusters*

3.2.1 Cluster Generation: Pulsed Vaporization within An Inert Gas Flow

To obtain gas-phase clusters, vapor condensation of the metal element is employed. The goal is to form a region where a supersaturated atomic vapor of the material is produced. A pulsed laser beam is tightly focused onto a small surface of the bulk metal to generate a hot plasma plume. The vaporized metal is supersaturated and is unstable to the condensation of clusters[28].

To enhance the production of clusters, the laser vaporization takes place within a pulsed cold inert gas flow. The inert buffer gas cools the produced supersaturated atomic gas[82]. The buffer gas also takes away the condensation heat of the just-formed cluster and therefore stabilizes it against evaporation. So that the inert gas facilitates the growth of clusters[95]. (For a nucleation theory, see [74][95][82])

The ablation laser is a frequency-doubled neodymium-doped yttrium aluminum garnet (Nd:YAG) pulsed laser focused on to a rod of the metal material under investigation. Vaporization involves the transfer of approximately 10 mJ of tightly focused laser energy onto the metal sample in an area of 0.005 mm^2 (Rayleigh waist of a focused Gaussian beam:

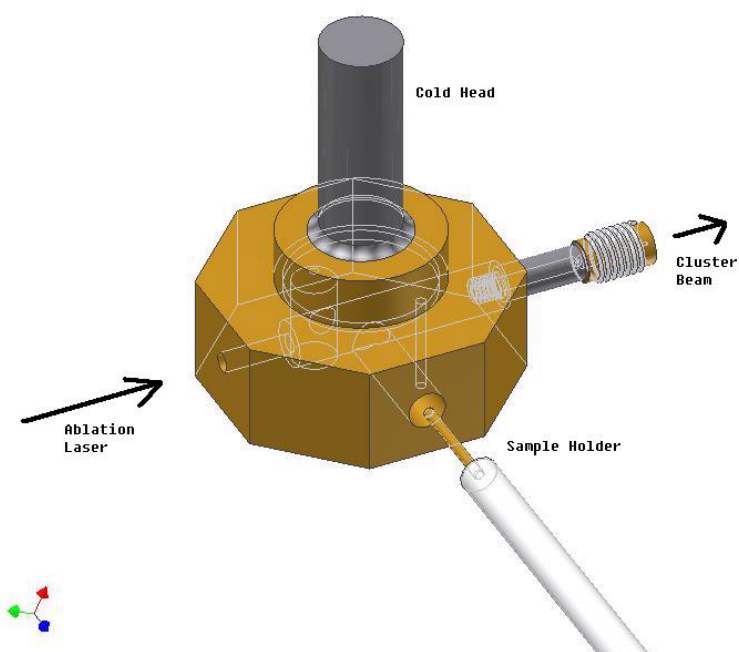


Figure 26: Cluster source layout used in this experiment. Laser vaporization sources produce pure and mixed clusters of most elements. A traditional oven source (or seeded expansion source) is limited to metals with a low boiling point (alkali, etc.)

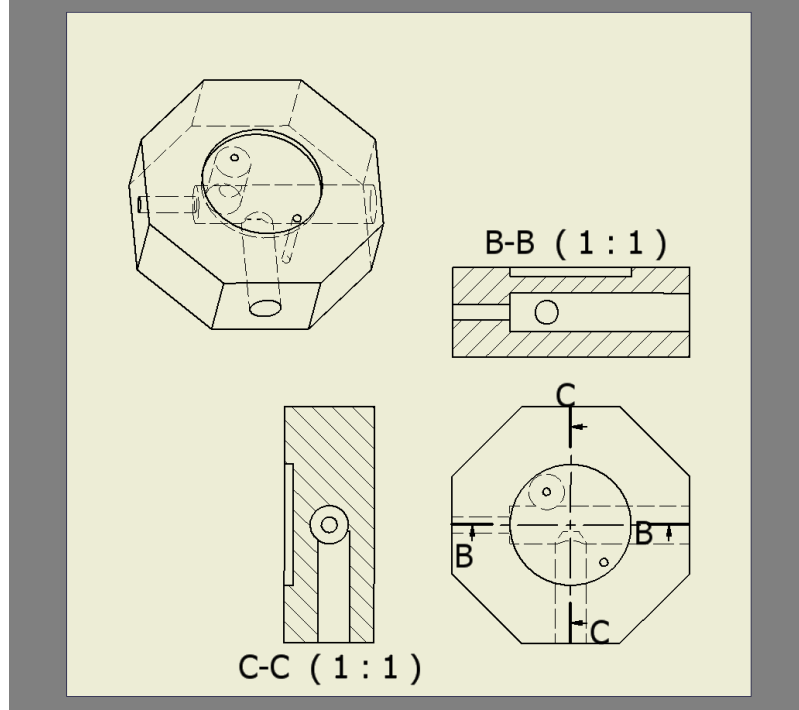


Figure 27: Cluster source. Machined from a copper block. Copper is chosen because of its high thermal conductivity.

$2w_0 = \frac{4\lambda}{\pi} \frac{f}{D}$) in about 10 ns to generate a hot plasma ($\sim 10,000$ K). About 10^{16} atoms will be removed from the surface. The hot plasma mixes with the cryogenically cooled helium gas pulse in a chamber in the source, causing cluster formation as discussed next.

3.2.2 Growth of Clusters at Low Temperature

The inert buffer gas is cryogenically cooled to a temperature of 20 Kelvin before it is injected into the ablation area. Clusters can be produced in a source that can be cryogenically cooled to 10 K using a closed-cycle helium refrigerator (Sumitomo Inc.). It is routinely operated at temperature 20 K. With a low-temperature inert-gas background there is essentially no evaporation and the abundance spectrum of clusters reflects that of a statistical nucleation event (thus can be compared with the abundance spectra from high temperature source, see Fig. 29). In other words, at low temperature, the atoms aggregate into clusters. From the nucleation and growth theory, the particle size distribution should obey the well-known

lognormal distribution[105][106]: (our sodium mass spectrum is presented in Figure 29)

$$p(x : \sigma, \mu, \Gamma) = \frac{1}{\sqrt{2\pi}\sigma(x - \Gamma)} e^{-\frac{1}{2}\left(\frac{\ln(x-\Gamma)-\mu}{\sigma}\right)^2} \quad (44)$$

where x is the cluster size in number of atoms, μ and σ are the mean and standard deviation and Γ is the critical cluster size (the smallest stable cluster).

J. BORGGREEN *et al.*

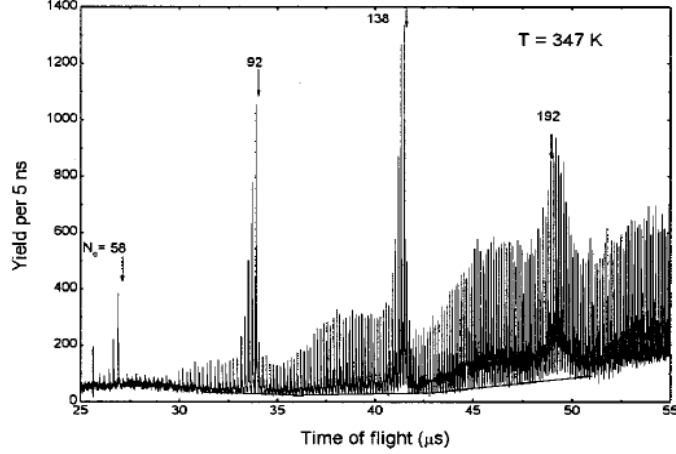


Figure 28: Sodium clusters mass spectrum with an high temperature oven source. From Borggreen et al.[21]

It is clear that the mass spectrum envelope fits the lognormal distribution well for $\Gamma = 1$. The deviations from the lognormal curve can be attributed to variations in the ionization potentials of the clusters - this will be discussed in detail later. The log-normal distribution allows us to describe the size distribution with two simple parameters μ and σ . These parameters can be controlled by varying the ablation conditions such as the laser fluence and the cryogenic inert gas pressure (this determines the number of collisions and thus the nucleation rate). The mean cluster size μ can be adjusted from ~ 30 to ~ 120 atoms at 20 Kelvin in our source.

The mean free path of a molecule increases with increasing temperature, assuming pressure is fixed. (mean free path $\lambda = \frac{1}{\sqrt{2}\pi n d^2} = \frac{1}{\sqrt{2}\pi d^2} \frac{RT}{P}$, d is the molecular radius, R is the gas constant, T is temperature and P is pressure. The ideal gas law is assumed to be valid.) Unlike an evaporative ensemble, our laser vaporization source allows the mean

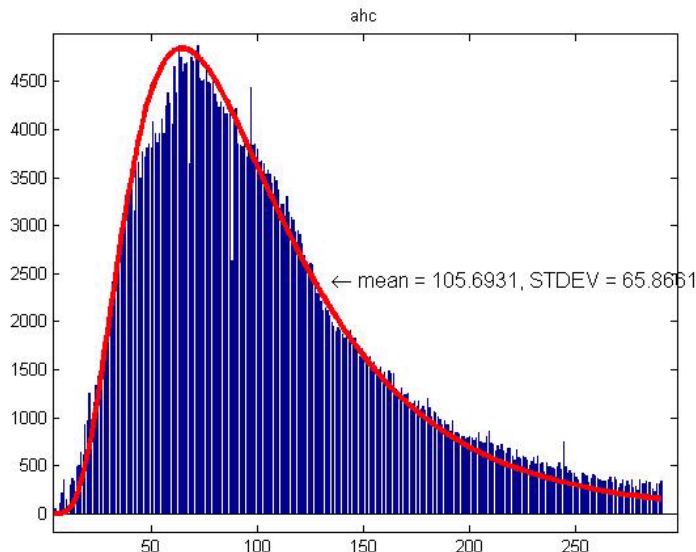


Figure 29: A mass spectrum with a low-temperature (20 K) laser vaporization source showing the structureless, log-normal ($\Gamma=1$) distributed signature characteristics of this source, as opposed to the structural mass spectrum in high temperature source. (Cf. Figure 28)

cluster size of the ensemble shifts to be controlled. See Figure 30 for an example of how the size distribution depends on pressure of the buffer gas.

Our cluster source has several unique features. The first is that it uses two pulsed valves connected in series. When the first valve opens the helium flows into a small cryogenically cooled reservoir to get cooled. Then the second valve injects the cooled gas into the laser vaporization chamber. This geometry is essential since it is not possible to cool room temperature He gas to cryogenic temperatures rapidly enough using a single valve. (It takes milliseconds to cool helium from 300K to 20K[109].

The cryogenically cooled helium reservoir also serves as a purifier to clean the pulsed inert gas. At 20 K oxygen and water will condense to the reservoir's wall so they will not react and contaminate the pure clusters. Note that reactive species can be introduced intentionally to produce compound clusters.

To have a better control on the range of temperature of the clusters, a heated nozzle is employed. The heated nozzle is installed right after the cluster source before the pulsed flow expands into the vacuum. The layout of the heated nozzle is shown in Figure 32.

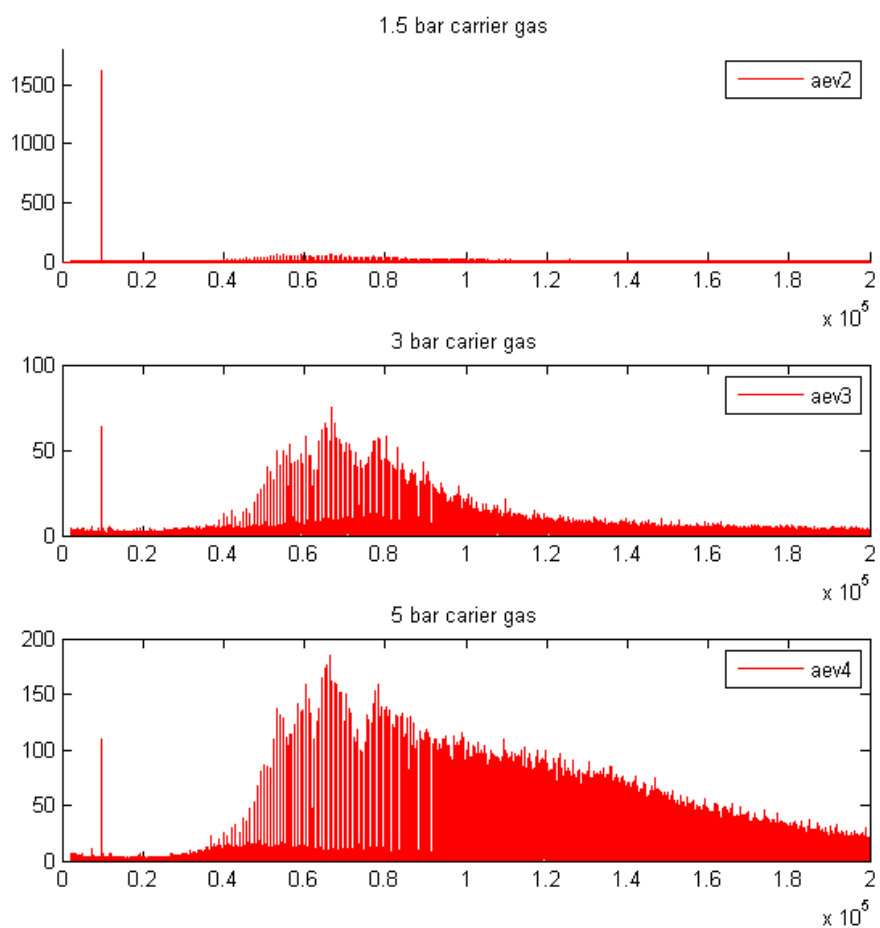


Figure 30: Aluminum clusters size distribution with different pressures of helium carrier gas. Notice the intensive peak on the left is the aluminum atom peak. The relative abundance between the atom and the clusters is the largest when backing pressure of helium is the least and vice versa.

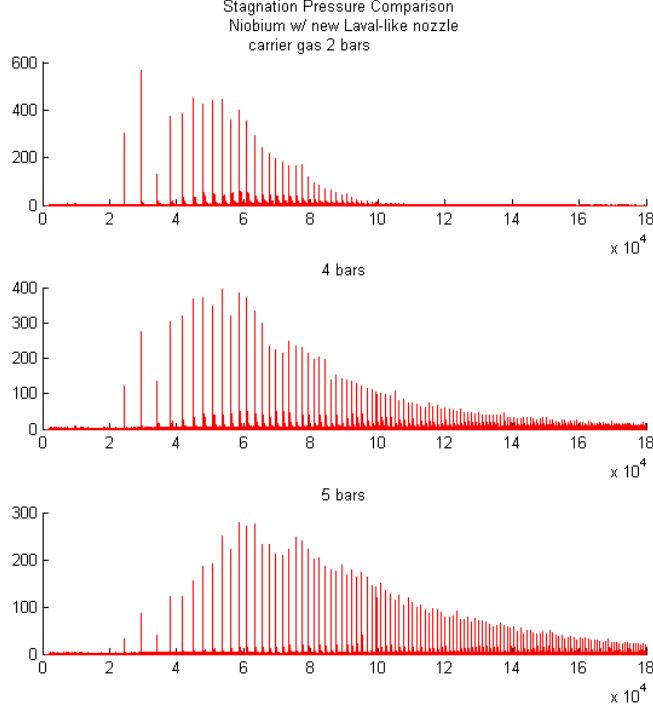


Figure 31: Niobium clusters size distribution with different pressures of helium carrier gas.

Basically, another reservoir is introduced with a resistive heater attached to it and by varying the current going through the heater one can adjust the inert gas and clusters mixture temperature. In this way we can adjust the temperature of the clusters from 10 K to 300 K. (See appendix part for a heat transfer calculation of our source.) The exact temperature is measured at the heated nozzle by a type-K thermocouple.

3.3 Formation of a Beam via Free Jet Expansion

Free jet expansion into a vacuum is used to produce beam of free clusters in a collision free environment. The various chambers of our apparatus are differentially pumped, see Table 2.

The carrier gas/ cluster mixture in the cluster source is at a higher pressure (called stagnation pressure) than the vacuum chamber that houses the source, see Figure 33. Due to this pressure difference the carrier gas/ cluster mixture expands through a nozzle into the source chamber. The physical picture of the kinetic process is explained as follows. If the

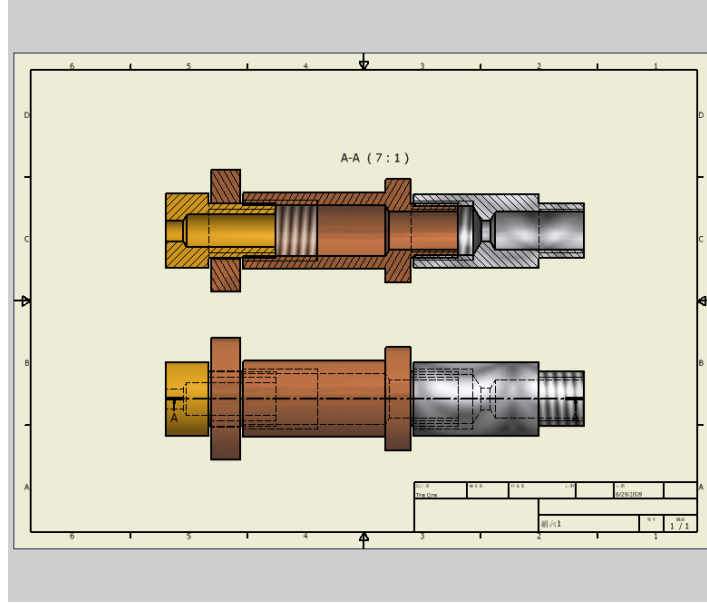


Figure 32: The shape of the heated-nozzle assembly. The middle part will be surrounded by thermalcoax heating element. The thermocouple will be soldered to the copper rind around the front nozzle.

Table 2: Pressures, mean free paths and the types of pumps in the differentially pumped environment.

Chamber:	Cluster	Source	Deflection	TOF
Pressure (Torr)	10^{-2}	$10^{-5} \sim 10^{-6}$	10^{-7}	10^{-9}
Mean Free Path (m)	10^{-3}	$1 \sim 10$	10^2	10^4
Pump	roots pump	turbomolecular	turbomolecular	turbomolecular

pressure in the cluster source is high enough that the mean free path of the gas (about 5 nm) is much shorter than the diameter of the nozzle (2 mm), many collisions take place around the throat of the nozzle (this is called a choked flow). The net effect of these collisions is to transfer all random oriented momentum toward the exit. As a consequence, the gas contents will then travel with very similar speeds, which depend only on the internal temperature of the carrier gas. Due to the expansion, the gas becomes more and more dilute down the stream until the mean-free path is comparable to the dimensions of the vacuum chamber. At this point a molecular beam is formed. (One can define a quitting surface which separates the molecular flow and the continuum flow, see Figure 35) This technique is called a free-jet expansion.

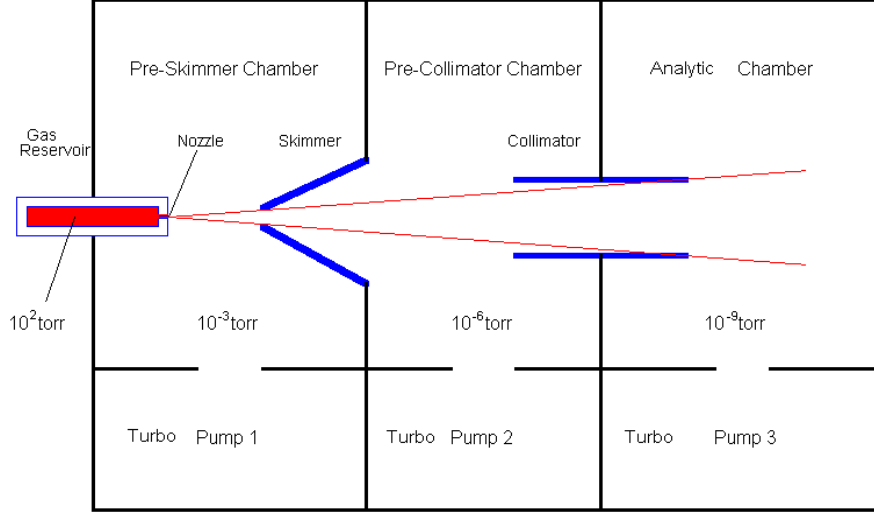


Figure 33: Illustration of the differential pumping of the system.

In hydrodynamics, the most important equation for the free jet expansion is the energy equation (conservation of energy, consisting of thermal, potential energy (these two make the enthalpy h) and the kinetic energy), which for such a flow becomes $h + v^2/2 = h_0$ where h is the enthalpy ($h = U + PV$) and v is the flow speed[82]. Viscous friction and heat conduction can be neglected, so a free jet expansion process is adiabatic[95][82]. So when our cluster/inert gas mixture enters the source chamber, it undergoes an adiabatic expansion and the thermal motion is converted into translational motion. From the above assumptions, one can obtain the following relations for the velocity and the temperature of

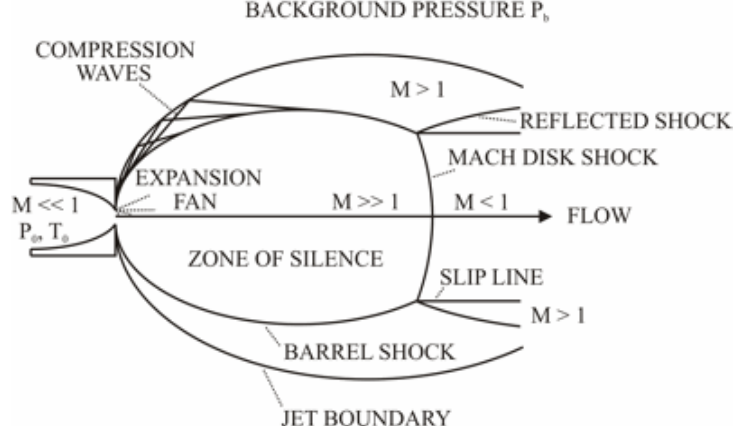


Figure 34: Continuum supersonic free-jet expansion and its interior structure. In the zone of silence there is essentially no collisions between the gas content. Thus a molecular beam can be extracted from the central streamline. From Ref. [95].

the molecular beam along the central streamline

$$V = M \sqrt{\frac{\gamma R T_{nozzle}}{W}} \left(1 + \frac{\gamma - 1}{2} M^2 \right)^{-\frac{1}{2}} \quad (45)$$

$$\frac{T_{He}}{T_{nozzle}} = \left(1 + \frac{\gamma - 1}{2} M^2 \right)^{-1} \quad (46)$$

where M is the Mach number, γ is heat capacity ratio, W is the molar mass, R is the gas constant, translational temperature T_{He} , and nozzle temperature T_{nozzle} .

Thus the translational temperature T_{He} may be tuned much lower than nozzle temperature T_{nozzle} . From Eq. 46 T_{He} is found to depend on the Mach number which in turn depends on the ratio of local speed to local speed of sound. So the Mach number will depend on the choking helium pressure P_{He} at the nozzle which can be tuned by varying the pressure difference between the helium backing pressure and the background vacuum pressure. Essentially two regimes may be obtained that we shall not discuss in detail here: a supersonic regime characterized by high values of P_{He} , where $T_{He} \ll T_{Nozzle}$, and an effusive regime characterized by low values of P_{He} where $T_{He} \approx T_{nozzle}$ [28]. Ultimately, one can manipulate the source parameters to achieve the condition $T_{nozzle} = T_{vibration}(\text{clusters vibrational temperature}) = T_{rotation}(\text{clusters rotational temperature}) = T_{He}$. For a formal discussion on the matter, Pauly and Scoles' books are referred[82][95].

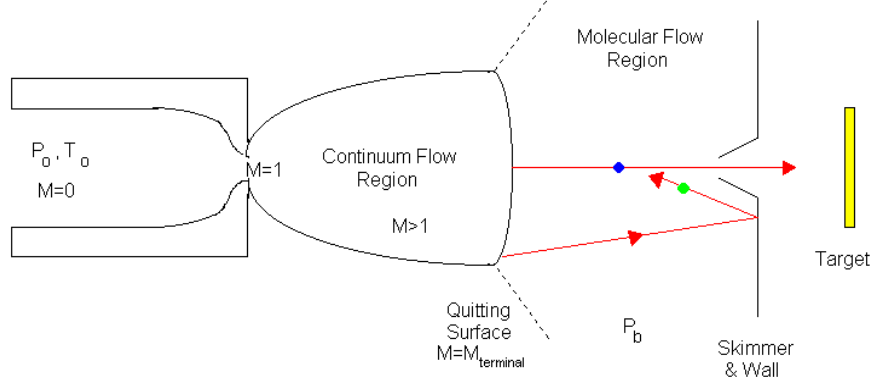


Figure 35: Quitting surface of the expansion. This is where the clusters turn into a molecular beam. This figure is not to scale. Normally the distance of the quitting surface will sit within a distance several orifice diameter away from the nozzle exit.

A free jet expansion in the supersonic regime could also lead to clustering. Our measurements were made far from the supersonic regime so no significant cluster formation occurs in the expansion. Hagena found that the condition for the onset of clustering scales with the product of the backing pressure and the nozzle diameter $P_0 d$ [45]. For a comparison our stagnation pressures (P_0) and nozzle diameter (d) gives a $P_0 d$ product in the range $0.44 < P_0 d < 22$ [Torr cm]. The theory suggests that, to avoid clustering (<10% of atomic gases) in supersonic expansion the following bound must be satisfied:

$$\frac{P_0}{\left(\frac{\epsilon}{\sigma^3}\right)} \left(\frac{d}{\sigma}\right)^{0.4} \left(\frac{T}{\frac{\epsilon}{k}}\right)^{-2.4} < 0.4 \quad (47)$$

Another issue of great importance for a cluster beam experiments, is whether the clusters have had sufficient time to come to thermal equilibrium. The clusters dwell in the source for about 1 millisecond before leaving through the nozzle. While they are in the source, but have come to equilibrium the distribution of the clusters internal state is given by the canonical ensemble corresponding to the helium gas temperature (i.e. the source temperature). In the source the clusters interchange energy with the gas and source walls through collisions and their energies will fluctuate. After expansion these cold clusters then are ejected into vacuum and form a beam. Now the clusters' internal energies are fixed because there are no collisions. Each individual cluster is a microcanonical ensemble with fixed total energy, but the ensemble of all the clusters in the beam is still distributed according to the

source temperature. This has been called a frozen canonical distribution[109]. Whereas individual clusters in the beam no longer have a defined temperature, the ensemble of clusters in the beam still reflects the source temperature. Consequently, the temperature of the source determines the distribution of the measured properties. This concept is useful in the experiment and provides an explanation for the appearance of relaxation-like processes despite the absence of any interaction with a heat bath[109].

In the cluster source, clusters are thermalized by collisions with background He gas. The thermalization rate or relaxation time is different for various degrees of freedom. The translational temperature is the easiest to thermalize, then the rotational temperature and vibrational temperature. It has been shown that in the source with a pressure of about 100 Torr and temperature 300 K, the vibrational relaxation time is on the order of 10 μ s[109]. The relaxation time is inversely proportional to the number of collisions per unit time

$$n_{\text{collision}} \sim \frac{\sigma_{\text{cross}} P}{\sqrt{k T_{\text{He}} m_{\text{He}}}} \quad (48)$$

where σ_{cross} is the cross-section for collision, P is the pressure, T_{He} is the temperature and m_{He} is the mass of He atom. At 1 Torr and 20 K the vibrational relaxation time is about 0.2 ms, which is shorter than the cluster dwell time in the nozzle (~ 2 ms).

3.4 *Beam Electric Deflection*

Deflection experiments on molecular beams date back to the famous Stern-Gerlach (SG) experiments of the 1920s[41], which demonstrated quantization of angular momentum by deflecting the different spin states of the silver atom with an inhomogeneous magnet. Here we use the same principle, but instead of a magnetic field we use an electric field to deflect a beam of metal clusters.

The cluster beam is collimated from the free jet expansion at a position right after the quitting surface, using a slit collimator. Thus the cross section of the resulting cluster beam has a rectangular shape. This greatly improves the intensity compared to a pinhole collimator. After collimation the beam is sent through a transverse inhomogeneous electric field created by a set of specially-shaped high voltage plates. The shape of the pole faces of the plates is designed to create a gradient in the direction transverse to the beam that can

interact with and deflect the clusters. The shape of the pole faces should have a more or less constant gradient over the rectangular cross section of the beam, so that all the clusters in the beam can experience the same force. For a review of the design of electric deflection plates for deflection measurements or state selection, refer to Ramsey[88], Scoles[95] or Pauly[82]. A cross section of our electric plates is given in Figure 36 with an indication of the slit's position and its dimension. Our experiment is done with coaxial deflection plates, where the pole faces are concentric cylinders.

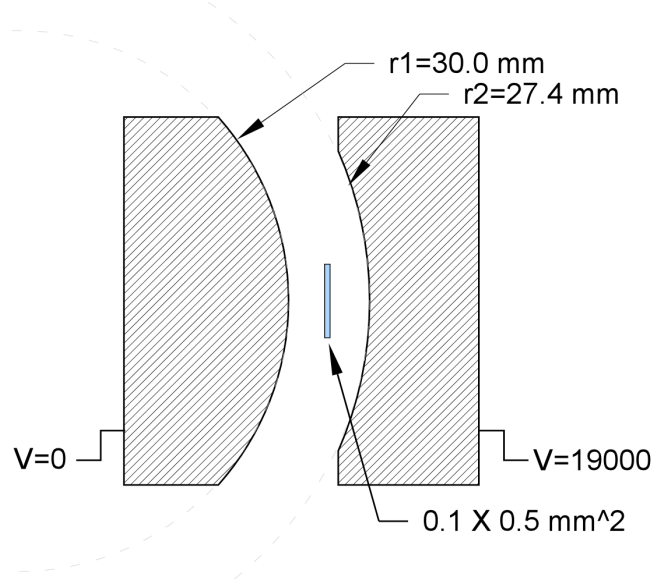


Figure 36: A cross section illustration of the electric plates. The strip in the middle indicates the cluster beam shape after collimation.

Between the two plates, the electric field has cylindrical symmetry along the beam so the field has only a radial component.

$$E(\mathbf{r}) = \frac{-V}{\mathbf{r} \ln\left(\frac{r_1}{r_2}\right)} \quad (49)$$

$$\nabla E(\mathbf{r}) = \frac{V}{|\mathbf{r}|^2 \ln\left(\frac{r_1}{r_2}\right)} \hat{\mathbf{r}} \quad (50)$$

where V is the voltage applied on the plates, \mathbf{r} is the vector position of the particle, r_1 and r_2 are the radius of the two pole faces. So the force F acting on a object in the field is

$$\begin{aligned} F = -\nabla(U) &= -\nabla(p \cdot E) = -p \cdot \nabla E \longrightarrow \text{for a dipole object} \\ &= -\nabla\left(\frac{1}{2}\alpha E^2\right) = -\frac{1}{2}\alpha \nabla(E^2) = -\alpha E \nabla E \longrightarrow \text{for a polarizable object} \end{aligned} \quad (51)$$

3.4.1 Deflection of a Single Particle and of a Beam

Now that we know the field and field gradient Eq. 49 and 50 in the deflection plates, we can calculate the deflection of a particle that will be measured at the detector. Let's first calculate the deflection of a polarizable conducting sphere. Lets say this particle passes through the middle of the collimator. The particle has a mass m and is travelling through the deflection plates with a velocity v . To simplify the analysis we will first neglect the deflection of the particle inside the coaxial plates. With this assumption the force acting on the particle is constant, and the force is applied for a time equal to L_1/v . In this case the electric deflection d at the detector for a polarizable sphere with isotropic polarizability α has an easy relation which can be obtained without any difficulty

$$d = \frac{\alpha E \nabla E}{mv^2} \left(\frac{L_1}{2} + L_2 \right) L_1 \quad (53)$$

where m is the mass, v is the traveling speed, E and ∇E are the field and field gradient, L_1 is the length of the deflection plate, and L_2 is the distance from the deflection plate to the detector. See Figure 37 for an illustration.

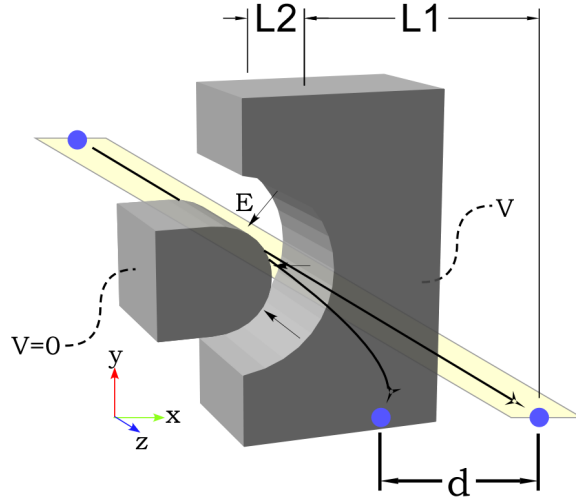


Figure 37: A conducting sphere passes through the inhomogeneous transverse electric field and deflects toward the high field.

A more realistic model accounts for the deflection of the particle that takes place inside the coaxial plates. The force keeps pushing the particle away from its undeflected path and therefore the particle experiences a changing force whose magnitude depends on particle's current position in between the plates. We must also account for the fact that the beam has a 2 dimensional cross section and the force varies in direction over the cross section. This requires a full calculation of the 2 dimension profile and we can no longer assume that the y component of the force is zero.

According to Equation 49, 51, 52 and 53 the equation of motion (EOM) for a dipole object and a polarizable object in the deflection field can be written down

$$\ddot{\mathbf{r}} = -\frac{V}{m \ln\left(\frac{r_1}{r_2}\right)} \frac{1}{r^2} (\mathbf{p} \cdot \hat{\mathbf{r}}) \longrightarrow \text{for a dipolar object} \quad (54)$$

$$= -\frac{\alpha V^2}{m \left(\ln\left(\frac{r_1}{r_2}\right)\right)^2} \frac{1}{r^3} \longrightarrow \text{for a polarizable object} \quad (55)$$

where m is the mass of the particle.

One can solve the second nonlinear EOM analytically by linearizing the equations of motion (EOM). Alternatively, one can solve the second nonlinear equation numerically. We have developed a deflection simulation on computer with finite difference method. Figure 38 shows the profile of the beam before it enters the field and after it leaves the field. (This takes into account the changing force along each trajectory as mentioned one paragraph earlier.)

The advantage of this approach is that it allows us to estimate the effects of misalignment and beam divergence on the deflection profile. We can simulate this by giving the particles an initial condition with a slight transverse velocity. The parameters used in this simulation are listed in Table 3.

This simulation is slightly exaggerated compared to a normal deflection experiment. We show this to illustrate the aberrations that appear in the deflection profile due to the inhomogeneity of the field gradient, and the deflection which takes place inside of the coaxial plates. The real deflections are smaller than this simulation. One can see immediately that the beam shape gets asymmetrically distorted. The beam is broadened slightly because different sides of the beam experience a different net force. At the detector only horizontal

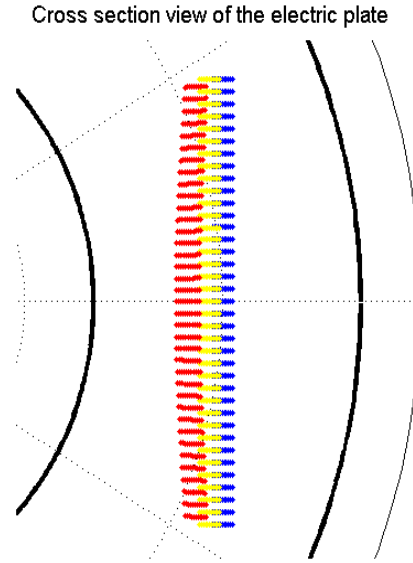


Figure 38: Cross section view of the finite difference simulation of conducting *spheres* passing through the field. Blue dots represent the clusters before they enter the field, yellow dots represent the clusters after they leave the field but with field turned off, and red ones represent the clusters after they leave the field with field turned on.

Table 3: Finite difference numerical method is used to generate the beam profile of a beam of polarizable spheres.

Parameters used to simulate Fig 38
'number of points along x in $2N+1 = 11$ '
'number of points along y in $2N+1 = 31$ '
'number of steps in time = 50'
'slit center in meters = 0.004'
'slit width in meters = 0.0002'
'slit height in meters = 0.004'
'initial horizontal velocity = -0.2'
'beam velocity = 350'
'polarizability in $\text{\AA}^3 = 24\text{e-}30$ '
'Voltage on E plates = 19000'
'mass in atomic mass unit = 24'
'bin, multiplier of $NN_x = 9$ '

information gets recorded, so to calculate a deflection profile we integrate the distribution of particles along the y axis. Figure 39 presents a corresponding profile recorded by the detector for the above simulation.

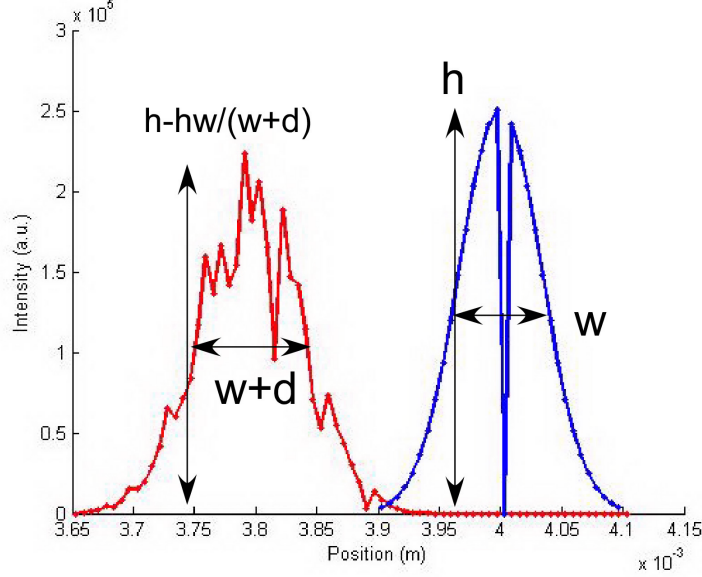


Figure 39: The simulated profiles recorded at the detector from Figure 38. Only horizontal information is kept. Verticle information is summed spacially. Red is the profile when the field is on, blue is field off.

For the deflection of a particle with a permanent dipole moment, the force depends on the projection of the dipole onto the field gradient $p \cdot r$ (see Eq. 54). Because the particle is rotating inside of the electric deflection plates and they also experience a torque $p \times E$, the calculation of the deflection profile becomes more complicated. As the particle rotates the projection of the dipole moment onto the field gradient changes and the particle experiences a rapidly changing force. We will discuss this in great detail in the next section.

The deflection relation for conducting sphere is $d \propto \frac{\alpha E \nabla E}{mv^2}$. One can easily estimate the broadening of the beam if one looks at the width change $\frac{\Delta W}{W}$, which will be proportional to the force difference across the beam $\frac{|\Delta F|}{|F|} \sim \frac{\Delta \left(\frac{1}{r^3} \right)}{\frac{1}{r^3}} = \frac{3\Delta r}{r}$ (From Eq. 49 and 50). For Δr we can use the collimator width and it is about 0.1 mm. For r we can take the position in the middle of the beam which will give $r = 3.5$ mm. Than $\frac{\Delta W}{W} = \frac{0.3}{3.5} \sim 10\%$. However this is overestimated because of the approximation for Δr .

There are also fringe fields at the entrance and the exit of the electric plates. Computer packages are available to simulate the fringe field (e.g. SIMION) if one needs to take the fringe field into account, but in general a reference calibration is enough to take this effect into account. We will also explain why the fringe field does not effect the rotational dynamics of our clusters in the next section.

In summary, it is possible to detect a rectangular beam without significantly distorting its beam profile and with only a small amount of beam broadening. Even for a non-ideal field configuration it has been shown that the deflection formula still describes the position of *the maximum* of the beam profile to high accuracy[101]. Note that up to now we still assume that the clusters in the beam still move at the same velocity.

3.5 *Adiabatic Electric Polarization Distribution of a Ensemble*

Now we can discuss the rotational dynamics of the cluster in Eq. 54 and 55. This is a very important aspect of interpreting the deflection profile. We know the deflection of a non-rotating single particle with dipole moment p in an electric field E from the previous section. (We assume E is along a horizontal z direction, so $E = E_z$) The transverse force along z acting on the particle will be

$$F_z = -\frac{\partial U}{\partial z} = \frac{\partial (p \cdot E)}{\partial z} = p \cdot \left(\frac{\partial E_z}{\partial z} \hat{z} \right) \quad (56)$$

So the deflection d along z due to E_z will simply be

$$d = \frac{1}{2} \frac{F_z}{mv^2} = \frac{1}{2} \frac{p \cdot \left(\frac{\partial E_z}{\partial z} \hat{z} \right)}{mv^2} \quad (57)$$

where m is the mass of the dipole moment. This formula assumes that the projection of the dipole moment onto the field axis $p \cdot \left(\frac{\partial E_z}{\partial z} \hat{z} \right)$ is constant, that the cluster is not rotating. However as we briefly mentioned previously, the clusters are rotating in the field. If we say the dipole couples to the cluster body and the cluster is rotating, the projection of the dipole moment $p \cdot \left(\frac{\partial E_z}{\partial z} \hat{z} \right)$ will depend on the rotational motion of cluster and will not be a constant. In addition, there will be a torque $\vec{p} \times \vec{E}$ acting on the cluster. So in order to calculate the trajectory of the dipole coupled to the cluster and obtain the deflection

profile of the whole cluster beam, one needs to first solve the rotational dynamics of the polar cluster under an electric field. To simplify this problem, we assume the cluster is a rigid body so we will be considering the dynamic rotation of a rigid polar body under an electric field. (We restrict ourself to the rigid body now, a discussion on this will be put afterward.) For easier explanation, we have to further assume the dipole moment is entirely fixed to the body of the rigid rotor.

So under these assumptions, with an electric field presents, there will be a torque ($p \times E$) acting on the rigid body. This means we will need to solve a dynamic rotation of a rigid body motion under a torque. The description of this general problem can be found in [42] and the torque-free rigid body equations of motion has been solved generally therein. With an electric field, the problem is generally complicated but we will show that, classically, for symmetric rigid rotors (with two moment of inertial equal) there will be a time average behavior for the product $\langle p \cdot (\frac{\partial E_z}{\partial z} \hat{z}) \rangle_t$ (will be abbreviated $\langle p \cdot \frac{\partial E}{\partial z} \rangle$ later on) that we can describe and will be very useful when considering the trajectory of a polar cluster. For asymmetric rigid rotors, there will be no general analytic solutions due to a reason we will later explain.

So for the symmetric rotor cases, we will show that the time averaged dipole and field gradient product $\langle p \cdot \frac{\partial E}{\partial z} \rangle$ is a good approximation to the force that the cluster will experience throughout the field. We will further show, in great details, that $\langle p \cdot \frac{\partial E}{\partial z} \rangle$ will depend on two projections. First, it will depend on the projection of the dipole moment to the total angular momentum of the cluster p_J . Second, it will depend on the projection of p_J to the electric field direction \bar{p} . In an ensemble of clusters there are many random orientations for the total angular momentum of cluster, so the product $\langle p \cdot \frac{\partial E}{\partial z} \rangle$ will actually have a distribution of values. We will describe this with a probability distribution of a cluster ensemble. (or a dispersion in susceptibility of a cluster ensemble.) We adopt a conventional name: **probability distribution function**, $\{p_i\}$ or $pdf(p)$. And we will regularly refer to this distribution as a **polarization distribution**[108]. So the deflection profile of the cluster beam will depend on the polarization distribution.

Under this basis, the adiabatic condition described in the experiment chapter (due to

the free jet expansion) will now come into play and affect our polarization distribution. This will be discussed in the last part of this section. Basically we are considering two adiabatic conditions. First, there is no thermal agitation nor a heat bath present in the clusters beam so that the no relaxation of the rotation will occur. Each cluster will represent a micro-canonical ensemble and the whole beam reflect the canonical ensemble while in the source. (See chapter 2.) Second the cluster enter and exit the field adiabatically in a way that the field is slowly turned on, so that one can relate the rotational energy distribution of the clusters before entering the field and while in the field. These two conditions make the cluster beam adiabatically interact with the field throughout. A quantitative description will be given therein.

So to understand the deflection profiles, we must first understand the adiabatic polarization distribution. We will describe several basic polarization distributions both classically and quantum mechanically in great detail in the following and describe their signatures in an deflection experiment. This discussion is somehow lacking, not well realized or not explained thoroughly in the field of cluster science[26]. Note that for real clusters we must consider the combined effects of the electronic polarizability and the rotational dynamics of any permanent dipole moments. This makes the analysis the polarization distribution a subtle job.

3.5.1 Nonpolar and Polarizable Clusters

First lets us step back and consider a simpler case. It will be an ensemble of *polarizable* clusters with *no internal dipole moment*. For these clusters the only contribution to the electric polarization is from the electronic polarizability, which in general is a tensor depending on the cluster's shape. This has been discussed in Chapter 2.1. To calculate the induced dipole under the laboratory framework from Eq. 11, 51 and 54, one will need to consider the rotation of the diagonal polarizability matrix under a body framework to the

matrix in a laboratory framework

$$\vec{p}_{\text{lab}} = \hat{\alpha}_{\text{lab}} \cdot \vec{E}_{\text{lab}} \quad (58)$$

$$= (R(t) \cdot \hat{\alpha}_{\text{body}} \cdot R(t)^{-1}) \cdot \begin{pmatrix} 0 \\ 0 \\ E_z \end{pmatrix} \quad (59)$$

$$= \left(R(t) \cdot \begin{pmatrix} \alpha_{11} & 0 & 0 \\ 0 & \alpha_{22} & 0 \\ 0 & 0 & \alpha_{33} \end{pmatrix} \cdot R(t)^{-1} \right) \cdot \begin{pmatrix} 0 \\ 0 \\ E_z \end{pmatrix} \quad (60)$$

where $R(t)$ is the time-dependent unitary rotation matrix (the form will depend on the actual free rotation of each cluster) and \vec{E}_{lab} is the laboratory field and it only has z component due to the experimental setup.

For a spherical cluster the induced dipole is simply given by $p_{\text{lab}} = p_z = \alpha E_z$ where α is the isotropic polarizability of the cluster. For non-spherical clusters, the polarizability is given in Eq. 60. Because the period of the rotation of the cluster is much shorter than the passage time through the field, the measured polarizability will be the time-averaged result of the rotating polarizability tensor $\langle (R(t) \cdot \hat{\alpha}_{\text{body}} \cdot R(t)^{-1}) \rangle_t$. And only the z component

of the resulting tensor will remain after it multiplies the field vector $\begin{pmatrix} 0 \\ 0 \\ E_z \end{pmatrix}$. Due to

the randomness of the rotation of the cluster in a ensemble beam, one can show that the tensor's time-averaged z component will be $\bar{a} = \frac{1}{3} \sum \alpha_{ii} = \frac{1}{3} \text{Tr}(\hat{\alpha}_{\text{body}})$ as in Eq. 15, and so it will also be the *average* of the polarization distribution of a polarizable ensemble. This is the reason measuring the rotational-averaged polarizability is the same as measuring the average polarizability[24]. So the average of the polarization distribution will simply correspond to $\bar{\alpha}$. In this case the clusters in the beam will be deflected in a way that the difference d between the average of the field-on profile and the average of field off profile will depend on the average polarizability \bar{a} . (See Figure 48). From Eq. 53 the amount of deflection will be

$$d = \frac{1}{2} \frac{\bar{\alpha} E (\nabla E)}{mv^2} C \quad (61)$$

where C is a geometric constant. In this way we can extract the average static dipole polarizability from the experimentally observed deflection d .

3.5.2 Polar clusters

This type of clusters has an intrinsic dipole moment. Moreover, when the cluster rotates, the dipole moment can couple to various freedom of motions to any extent, e.g. a body axis of the cluster, the rotation of the cluster, through different mechanisms. Here we simply divide the interweaving complications into two basic scenarios: totally coupled to the cluster body axis (strong coupling, or locked-moment model) or totally uncoupled from the cluster (or weak coupling).

3.5.2.1 Locked-Moment Model

The coupling of this kind is normally the charge anisotropy inside the cluster. Literature on this problem can be found in [13][12][34][26][94][9] and the references therein. A short summary is given below to understand the polarization distribution of an ensemble of polar clusters. Both classical and quantum mechanical treatments are discussed. However, the analytical solution is limited to symmetric tops, for asymmetric tops the dynamics are chaotic and numerical methods had been developed[33][3].

Classical Treatment

Symmetric Top The classical picture has been considered by Bertsch[12] and Dugourd[34]. They had solved the generic Lagrangian for the rotation of a symmetric rigid rotor with a dipole moment p_0 coupled to (or fixed in direction in the cluster's body) one of the structural symmetry axis of the body in an electric field E . Bertsch had published the Fortran source code on the internet and one can use it to get the polarization distribution for a classical symmetric rotor[9]. They both describe the analytical solution which accounts for the precessional and nutational motion of a polar rotor in an electric field. Experimentally, Dugourd had confirmed the polarization distribution with this classical theory using TiC_{60} and PABN molecule in a molecular beam deflection experiment, very similar to ours

experimental setup[34][38].

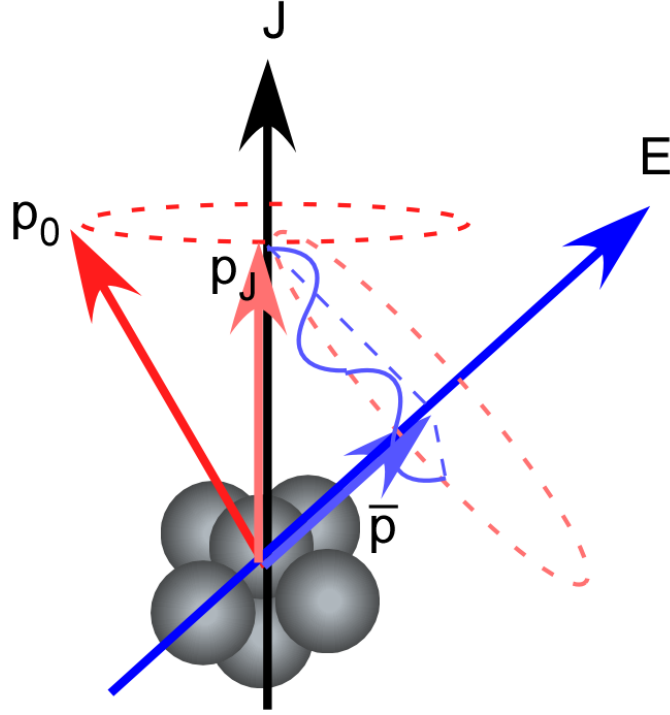


Figure 40: Vector model representation of a symmetric polar rotor under an electric field. Nutation and precession of p_J are shown and the time-averaged effective dipole \bar{p} is indicated. The effective dipole \bar{p} will be the effective polarization of this rotating cluster under electric field in this particular arrangement. In an ensemble the orientation of J , E and p_0 are all random so one will have a distribution of \bar{p} . For an visual illustration on symmetric rotor nutation please see [42].

As mentioned earlier in this section, the clusters we consider rotate fast enough at 20 Kelvin that the average dipole moment experiencing the field p_J will be the projection of the dipole p_0 along the rotating direction, which is the direction of the total angular momentum J (see Figure 40 for an illustration). And due to the electric field the average dipole p_J will experience a torque so the rotating rotor will nutate and precess along the field direction due to conservation of angular momentum. Because the electric field is inhomogeneous the gradient field generates a force on the dipole that pushes the nutating dipole along the field direction. One can also consider a time-averaged effective dipole \bar{p} from the nutation of p_J that experiences the force. This effective dipole \bar{p} is equal to

the projection of the time-averaged nutating p_J over a full nutation cycle along the field direction. So the effective dipole \bar{p} actually depend on the relative orientations between the three vectors: the total angular momentum J , the orientation of the body-fixed dipole and the field gradient direction. So for an ensemble of randomly rotating clusters with a fixed dipole p_0 with respect to the frame of the cluster, a distribution of polarization of the effective dipole \bar{p} is needed.

The following formula are the classical solution from considering the classical mechanics[42]. The full derivation can be found in [12]. The generic Lagrangian of a dipolar rotor in an electric field is

$$L = \frac{1}{2} \sum I_k \omega_k^2 + p_0 E \cos \theta \quad (62)$$

with, in Cartesian coordinate, the principal momenta of inertia I_k , the angular frequency ω_k , E is the electric field strength and θ the angle between p_0 and E . Now for a symmetric rotor $I_1 = I_2$, from the Lagrangian equation one can derive the invariant of motion for $\dot{\theta}$ and write down the following differential equation

$$\frac{I_1}{2} \dot{\theta}^2 + \underbrace{\frac{(m_z - m_3 \cos \theta)^2}{2I_1 \sin^2 \theta} - p_0 E \cos \theta}_{U_{eff}(\theta)} = \underbrace{T - \frac{m_3^2}{2I_3}}_{T'} \quad (63)$$

where m_k , $k=1,2,3 = I_k \omega_k$ and $J = \sum_{k=1,2,3} \sqrt{m_k^2}$ and m_z is the projection of the total angular moment on the field axis.

Then the period of nutation τ and the average polarization \bar{p} along E during one period can then be solved from Eq. 63 and they are given by (for an visual illustration please see [42])

$$\tau = \frac{2}{\sqrt{h(u_2 - u_0)}} K(\nu) \quad (64)$$

$$\bar{p}_{(cl)} = \frac{u_2 K(\nu) + (u_2 - u_1) E(\nu)}{K(\nu)} \quad (65)$$

where

$$\nu = \frac{(u_2 - u_1)}{(u_2 - u_0)} \quad (66)$$

$$u_1, u_2, u_3 = \text{roots of } f(u) \quad (67)$$

$$u = \cos \theta \quad (68)$$

$$f(u) = (e + hu)(1 - u^2) - (m_z - m_3 u)^2 \quad (69)$$

$$h = 2I_1 p_0 B \quad (70)$$

$$e = 2I_1 E' \quad (71)$$

K and E are the complete elliptic integrals of the first and second kind

$$K(\xi) = \int_0^{2\pi} \frac{d\theta}{\sqrt{1 - \xi^2 \sin^2 \theta}} \text{ or } K(\xi) = \int_0^1 \frac{dt}{\sqrt{(1 - t^2)(1 - \xi^2 t^2)}} dt \quad (72)$$

$$E(\xi) = \int_0^{\frac{\pi}{2}} \sqrt{1 - \xi^2 \sin^2 \theta} d\theta \text{ or } E(\xi) = \int_0^1 \frac{\sqrt{1 - \xi^2 t^2}}{\sqrt{1 - t^2}} dt \quad (73)$$

This solution is analytical only because we are dealing with a symmetric rotor. The orientation of the dipole direction will oscillate between two positive angles u_1, u_2 [42]. And the average polarization \bar{p}_{cl} of any dipole rotor is given by Eq. 65.

From statistical mechanics the partition function for this rotor ensemble then can be expressed as

$$Z = \int_0^\infty dJ \int_{-J}^J dm_z \int_{-J}^J dm_3 e^{-\frac{\varepsilon(J, m_3)}{k_B T_{rot}}} \quad (74)$$

where energy $\varepsilon(J, m_3)$ is

$$\varepsilon(J, m_3) = (J^2 - m_3^2)/2I_1 + m_3^2/2I_3 \quad (75)$$

and J is the total angular momentum defined in Eq. 63. The ensemble average of an operator or physical observable \mathcal{O} will simply be

$$\langle \mathcal{O} \rangle_{avr} = \frac{1}{Z} \int_0^\infty dJ \int_{-J}^J dm_z \int_{-J}^J dm_3 \mathcal{O} e^{-\frac{\varepsilon(J, m_3)}{k_B T_{rot}}} \quad (76)$$

So the average or the mean of the polarization distribution is obtained with $\mathcal{O} = \bar{p}$, and the polarization distribution $pdf(\bar{p})$ is obtained using $\mathcal{O} = \delta(p(m_z, m_3) - \bar{p})$ and with p is the all possible average polarization $\{\bar{p}\}$ given by all possible m_z and m_3 in the ensemble

summation in Eq. 76. (This ensemble describe a non-interacting adiabatic dipole rotors, contrary to the Langevin-Debye behavior interacting dipoles in Chapter 2, Eq. 22.)

Now we look at an example.

Example 1 *The polarization distribution of a ensemble of spherical rotors with dipole moment p_0 under zero or low field $p_0E \ll kT$.*

For a spherical top, from Eq. 65 the average polarization under zero field limit (or low field limit, $p_0E/kT \ll 1$) can be easily derived and it is

$$\bar{p} = \frac{u_2 + u_1}{2} \quad (77)$$

Plug this into Eq. 76 then the polarization distribution will be $pdf(\bar{p}) = \langle \delta(p - \bar{p}) \rangle_{\text{over all } p}$ (here p is all the possible polarization given by m_z and m_3 in Eq. 76). One can get $pdf(\bar{p}) = \frac{1}{2} \log(\frac{p_0}{|\bar{p}|})$. In this derivation we will need the following integrals:

$$\int_{-1}^1 dx \int_{-1}^1 dy \delta(c - xy) = \int_{-1}^1 dx \frac{1}{|x|} \quad (78)$$

(eliminate integration in y causes $|x|$ to range from $c \rightarrow 1$)

$$= 2 \int_c^1 dx \frac{1}{|x|} \quad (79)$$

$$= -2 \ln(c) \quad (80)$$

Thus the polarization distribution of the spherical rigid polar rotors in an electric field will be described by the logarithmic function, in the zero field limit. (It also applies for low fields if $p_0E \ll kT$. If this is not satisfied then Eq. 77 is not valid and the average polarization in Eq. 65 need to be used. This will be discussed in the following paragraphs. For 1 Debye p_0 in our electric field 10^6 V/m, p_0E is about $1 \sim 2$ Kelvin. The logarithmic polarization distribution is plotted in Figure 41.) Equivalently, one can say logarithmic broadening will be a characteristic of the deflection of a spherical polar rotor beam. One important thing is that from the above derivation the logarithmic broadening is temperature independent and rotation independent. We will discuss this together in the following quantum picture section.

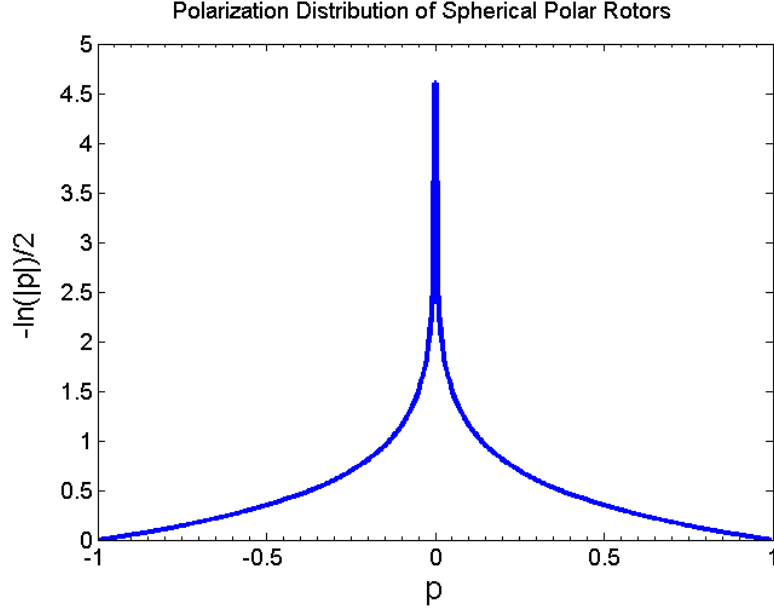


Figure 41: Logarithmic polarization distribution. Horizontal is plotting $p = \bar{p}/p_0$. This is the characteristic polarization distribution for a spherical cluster with a intrinsic permanent dipole moment in the zero or low electric field limit.

Under certain conditions ($p_0 E/kT \sim 1$), the polarization distribution can become highly asymmetric[9][103][13][12] even with an ensemble of spherical dipole rotors. Eq. 77 is not valid and the average polarization in Eq. 65 should be used. The classical program developed by Bertsch can simulate the polarization distribution of an ensemble of 'symmetric' polar rotors[9]. The result is quoted from therein and plotted in Figure 42. Three different types of symmetric rotors (prolate, spherical and oblate) are simulated. Note that the polarization distribution profiles can be asymmetrical. However different rotor shapes seem to have a small effect on the overall distribution profiles. The asymmetry is due to the nutation of the dipole direction will be slightly biased towards the low field direction. From Eq. 65, the oscillation between two angles u_1, u_2 will be weighted and more along the lower energy direction. Our condition is within $p_0 E/kT \ll 1$, so we are not yet in this condition. But it is important to point out that even a spherical polar top can have asymmetric polarization distribution and this will give asymmetric deflection profile, when $p_0 E/kT$ is close to or larger than unity.

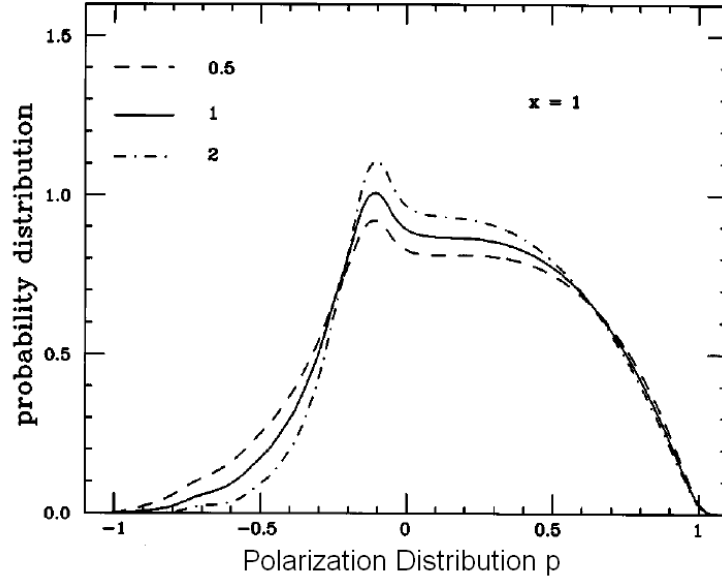


Figure 42: Polarization distribution of symmetrically prolate ($\gamma = 0.5$), spherical ($\gamma = 1$) and oblate ($\gamma = 2$) tops under high field (or large $\frac{p_0 E}{kT}$). (γ is defined in Eq. 16 and $x = \frac{p_0 E}{kT}$) The important point is that even a spherical polar top can have asymmetrical polarization distribution for large x . Figure Ref. [13].

Asymmetric Tops As mentioned earlier, a classical analytic solution for a dynamic rotation of asymmetric polar rigid rotor under an electric field is not available yet. Numerical methods are available. Dugourd etc. performed a numerical molecular dynamics simulation[33]. Their simulated results show good agreements with their experiments using asymmetric molecules PAMN. They showed that even for a asymmetric molecules one can still see the corresponding broadening. Their developed code could be very useful because in this case the shape of the molecule is no longer limited to the symmetry of the rotors and thus can be used to interpret the polarization distribution of any rigid polar rotors directly.

Quantum Mechanical Treatment: Again the quantum mechanical discussions had focused only on the symmetric tops. In general though, if one can diagonalize the generic Stark Hamiltonian of a asymmetric top one can also get the asymmetric solutions. However because the dimension of the matrix one needs to diagonalize grows rapidly as the total angular momentum J increases, the calculations are restricted to small J . Related material

can be found in [26][13][103][49].

Same adiabatic conditions are considering under the classical description.

Symmetric Tops The generic Hamiltonian for a symmetric top under an electric field is

$$H = H_{rot} + H_{stark} \quad (81)$$

$$H_{rot} = \frac{P_x^2}{2I_x} + \frac{P_y^2}{2I_y} + \frac{P_z^2}{2I_z} \quad (82)$$

$$= \frac{P^2}{2I_B} + P_z^2 \left(\frac{1}{2I_C} - \frac{1}{2I_B} \right) \quad (83)$$

$$\text{where } I_x = I_y = I_B, I_z = I_C \text{ and } P^2 = P_x^2 + P_y^2 + P_z^2$$

because the total angular momentum J and the angular momentum along z , K , are quantized, P^2 and P_z^2 will equal to $J(J+1)\hbar^2$ and $K^2\hbar^2$. So H_{rot} become

$$H_{rot} = BJ(J+1) - (C-B)K^2 \quad (84)$$

$$B = \hbar/I_B, C = \hbar/I_C \quad (85)$$

The angular moment projection on the field direction M is also quantized. So the good quantum numbers in this case are the regular J, K and M . So under this basis, from perturbation theory we can write out the projection of the dipole moment along the field direction [8][102][26]

$$\bar{p}_{(QM)} = \frac{MK}{J(J+1)} p_0 + \left[\frac{\left((J+1)^2 - M^2 \right) \left((J+1)^2 - M^2 \right)}{(J+1)^3 (2J+1) (2J+3)} - \frac{(J^2 - M^2) (J^2 - K^2)}{J^3 (2J+1) (2J+3)} \right] \frac{p_0 E}{B} \quad (86)$$

(Note that there is a typo in [26] in the third term in the denominator $(2J+3)$. One can check this with the other two references.)

One may wonder about the relation between the classical result \bar{p}_{Cl} in Eq. 64 and quantum result \bar{p}_{QM} . Becker [94] has shown in detail that they are equivalent. Now we can calculate the ensemble average and get the polarization distribution as in Eq. 76 (in this discrete case), up to the second order:

$$pdf(\bar{p}_{QM}) = \frac{\sum_{M,K} \delta(\bar{p}_{QM} - p(M, K)) e^{-\beta(BJ(J+1)-(C-B)K^2)}}{\sum_{M,K} e^{-\beta(BJ(J+1)-(C-B)K^2)}} \quad (87)$$

[13] where $\beta = 1/kT$. This is equivalent to Eq. 76 if the discrete summation is replaced by the continuous summation. In fact the angular momentum J we are dealing with is normally large enough that the continuous treatment is always valid and preferred in our case.

Example 2 *Derivation for the logarithmic adiabatic polarization distribution of an ensemble of spherical polar tops*

From Eq. 87 the $pdf(\bar{p}_{QM})$ for a spherical polar ensemble in a field E is given by ($C = B$)

$$pdf(\bar{p}_{QM}) = \frac{\sum_{M,K} \delta(\bar{p}_{QM} - p(M, K)) e^{-\beta BJ(J+1)}}{\sum_{M,K} e^{-\beta BJ(J+1)}} \quad (88)$$

$p(M, K)$ are all possible dipole moment polarization the ensemble can give. For a given total angular momentum J , the $M = -J \sim J$. Also K needs to be quantized as well $K = -J \sim J$ (one can also see Figure 40 for an illustration). Now we want to calculate the number of configurations of possible orientations of M and K that will give $p(M, K)$ the same with \bar{p}_{QM} , this means to find the number of possible solutions for M and K that can give the corresponding \bar{p}_{QM} . From Eq. 86 at zero field limit, $p(M, K)$ is just $\frac{MK}{J(J+1)}$. So we are going to find the number of ways in the ensemble from which $M * K = \bar{p}_{QM} J(J+1) \equiv C$.

In order to find how many possible points M, K satisfies $M * K = C$, we use same method when calculating DOS for the free electrons. When J is dense enough we can treat this as continuous integral. So we will calculate the area density crossed by the $M * K = C$ line.

We want to calculate the area covered by the $MK = C$ hyperbola in Figure 43. When J is high enough that means the points are dense enough and we can calculate the area dA between $MK = C$ and $MK = C + dC$

$$dA = \int_{\frac{C+dC}{J}}^J \frac{C+dC}{M} dM + J \cdot \frac{dC}{J} - \int_{\frac{C}{J}}^J \frac{C}{M'} dM'$$

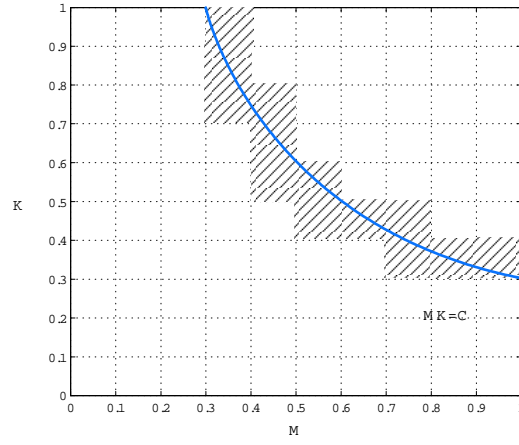


Figure 43: The number of configurations of the possible M and K quantum numbers that make up a constant value $M * K = C = \bar{p}_{QM} J(J + 1)$.

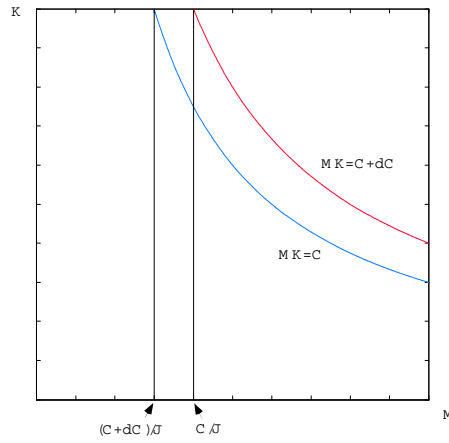


Figure 44: In the continuum approximation the number of configurations can be found by calculating the area between the two constant parabola.

$$\begin{aligned}
&= (C + dC) \cdot \ln(M) \Big|_{\frac{C+dC}{J}}^J + dC - C \cdot \ln\left(\frac{C}{M'}\right) \Big|_{\frac{C}{J}}^J \\
&= dC \cdot \ln \frac{J^2}{C} + C \cdot \ln\left(1 - \frac{dC}{C}\right) + dC \cdot \ln\left(1 - \frac{dC}{C}\right) + dC
\end{aligned}$$

Now Talor expansion of $\ln(x) = (x - 1) - \frac{(x-1)^2}{2} + \frac{(x-1)^3}{3} - \dots$ for $|x - 1| \leq 1$.

$$\therefore dA = dC \cdot \ln \frac{J^2}{C} + (-dC) - \frac{C}{2} \left(\frac{dC}{C}\right)^2 - \frac{C}{3} \left(\frac{dC}{C}\right)^3 + dC \left(-\frac{dC}{C} - \frac{1}{2} \left(\frac{dC}{C}\right)^2 + \dots\right) + dC$$

We can drop everything smaller than $\frac{dC}{C}$, than only the first term survives and this becomes,

$$\frac{dA}{dC} = \ln \frac{J^2}{C} = \ln \frac{1}{\bar{p}_{QM}} \quad (89)$$

This result is independent of value of J and the temperature. So we expect the broadening will be independent of J and T in the deflection experiments. As mentioned before, this is true with a classical picture as well. This is an important point because there have been so many confusion about the broadening could be simply rotational thermal averaging effect. Importantly for spherical rotor under low field limit the broadening is temperature independent. (This can also be further extended to symmetric rotor with not too large deformation from a sphere. See Figure 42 and discussion therein) Our rotational angular momentum at 20 Kelvin is always high enough. In Figure 45 and 46, I simulate the extreme case where J is as low as 20 and another J at 100, one can see that the logarithmic nature is still present at $J = 20$ and already match the logarithmic function at $J = 100$.

For asymmetric top In this case the only good quantum number will be M due to the random motion nature (or chaotic) of the rotational axis in the dynamic rotation of rigid body under torque[42]. Equation like Eq. 63 does not exist. And as is described in the beginning of this section, only numerical methods are available. However it is suspected that slightly asymmetric tops ($I_C \neq I_A \sim I_B$) can have similar behavior as symmetric tops because the similarity in the Hamiltonian[102].

Summary and Remark The first and second moment of the adiabatic polarization distribution then can be calculated. For symmetric rotors these are studied thoroughly by Kresin etc. [26]. The result is summarized into Table 4.

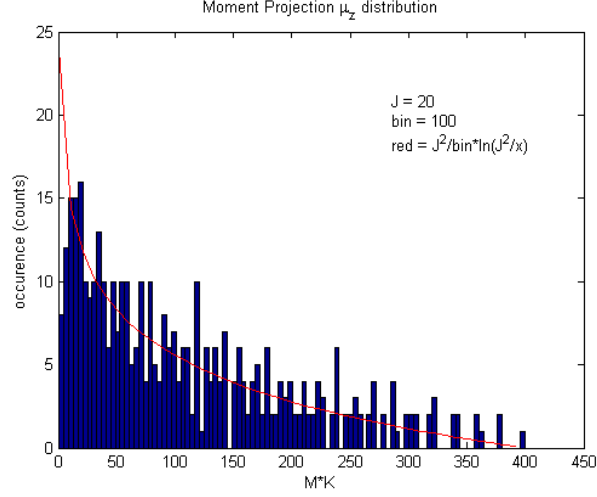


Figure 45: The examination between a real logarithmic function (in red, line) and a distribution of quantized polarization (blue histogram) under low angular momentum J .

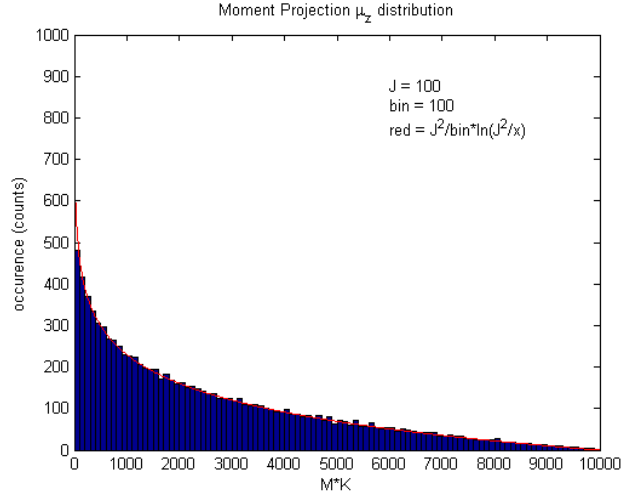


Figure 46: Angular momentum $J = 100$. As one can see the distribution (blue histogram) is very close to the logarithmic function (red).

Table 4: The polarization distributions and their first and second moment (mean and variance) for three kinds of rigid polar rotors: spherical, symmetric and asymmetric. Under low field limit.

rotor symm.	Polarization Distribution	1st Moment	2nd Moment
spherical	$\ln(\frac{p_0}{ p })$	$\frac{2}{9} \frac{p_0^2 E}{kT}$	$\frac{p_0^2}{9}$ (when $\frac{p_0 E}{kT} \ll 1$)
symmetric	depends on κ , $\frac{p_0 E}{kT}$	$\frac{2}{9} \frac{p_0^2 E}{kT} (1 - \frac{1}{5} \kappa)$	$\sim \frac{p_0^2}{9}$ (when $\frac{p_0 E}{kT} \ll 1$ and $\kappa \sim 0$)
asymmetric	N.A.	N.A.	N.A.

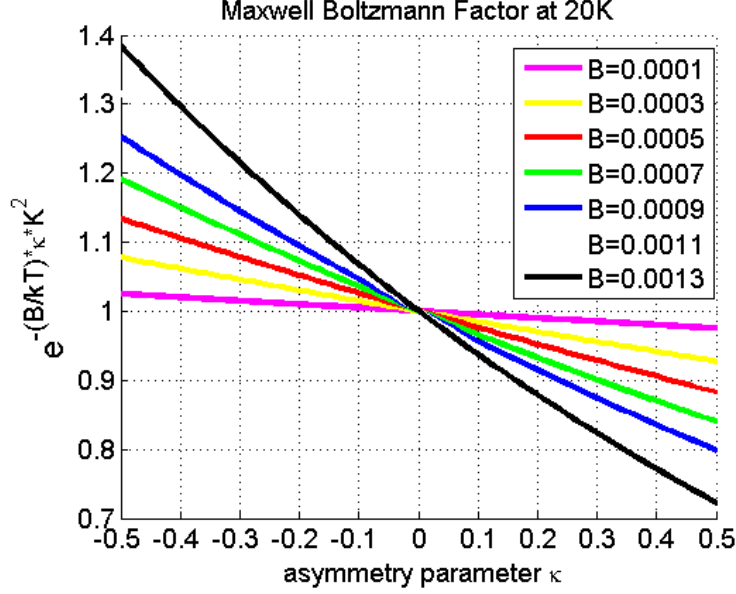


Figure 47: The Boltzmann factor associated with K quantum number: this is essentially the weighting factor in Eq 88. One can somehow include this and maybe one can derive the polarization distribution (refer to Figure 43). B is the rotational constant. Asymmetry parameter κ is defined in the first chapter.

For symmetric top the effect of deformation from spherical shape to the polarization distribution will lead to a change in the Boltzmann population in split K levels (see Figure 47). But we have seen classically this contributes very little to the polarization distribution for a wide range of asphericity (Figure 42)[13]. So the broadening will still be fairly good by $\frac{p_0^2}{9}$ estimation when $\frac{p_0 E}{kT} \ll 1$ and $\kappa \sim 0$. However for asymmetric top the polarization distribution does not have an analytic solution and exhibit non-integrable and unstable dynamics [31]. The results are organized into Table 4. Nonetheless up to 300 atom sodium clusters we do not see any significant broadening.

In cluster beams, there are no interactions. Due to the adiabatic entering into the field, the ensemble averaged orientation of *spherical* symmetric top is $\frac{2}{9} \frac{p_0^2 E}{kT}$ ($\kappa = 0$) (under $\frac{p_0 E}{kT} \ll 1$), which differ from the Langevin-Debye formula $\frac{1}{3} \frac{p_0^2 E}{kT}$ (which requires a heat bath, see section 2.2.1 and Eq. 22) by the coefficient $1/3$. For a symmetric spheroid top it is $\frac{2}{9} \frac{p_0^2 E}{kT} (1 - \frac{1}{5}\kappa)$, where κ is the asymmetric parameter of either prolate or ablate. This conclusion seems to be valid up to $x = \frac{p_0 E}{kT} \sim 0.3$ for commonly rotational constants[26]. So

one can experimentally observe the temperature dependence contribution to the average polarization to determine the dipole moment.

The reasons for the adiabatic treatment for the clusters ensemble throughout the experiment is given here:

1. Here we assume the clusters are rigid rotors because at 20 K the clusters are believed to be in its ground state. (Debye temperature for sodium is 158 K, so approximately the average energy to excite a phonon mode is $158/N^{1/3}$, where N is number of atoms in the cluster[109]. So in theory only close to a thousand atoms we will then start to see significant population of phonon modes at 20 K.) Even if only a few phonon modes (one or two) are excited, it is not enough to serve as a heat bath. So each polar cluster possesses a permanent dipole moment p_0 fixed to the body frame. (We can consider this a locked 'dipole' scheme in analogy to the 'locked spin model' terminology in magnetic studies[13].) Experimentally, it has been shown that in some cases where excited phonon modes (or if gas scattering presents, see the following) are highly excited the asymmetric (and only for asymmetric ones) clusters will not conserve their angular momentum while experiencing the field torque[38][3] (Sometimes called a memory loss effect[26].) This will lead to an absence of broadening in the polarization distribution and then only a shift in the deflected beam will be observed instead (so it will resemble the response of a polarizable particle). We believe we do not have any phonon excitation nor other relaxation present in our cluster beam.

2. Two adiabatic processes are considered established in our experiment.

- (a) The beam enters the field adiabatically. As mentioned earlier, the electric plates inevitably have fringe field. From the perspective of the moving cluster, the rate of change in field strength is $\sim 10^{-5}$ sec in time, which is very long compared to the rotation period of cluster ($\Gamma_{\text{rot}} \sim kT_{\text{rot}}$) $\sim 10^{-11-12}$ sec (depending on the rotational constant). This means the field is equivalently slowly turned on. So the rotational distribution of the cluster ensemble in the field can be linked to the rotational distribution of the cluster ensemble in the source, which reflects

the Boltzmann distribution at source temperature.

- (b) The ensemble travels through the field adiabatically. While the beam is in the field plates, there are no collisions nor thermal relaxation present in the molecular beam, thus the ensemble is adiabatic.

So the clusters adiabatically interact with the field throughout. We know the rotational energy and its distribution of the cluster ensemble at every stage.

3.6 Beam Profiles

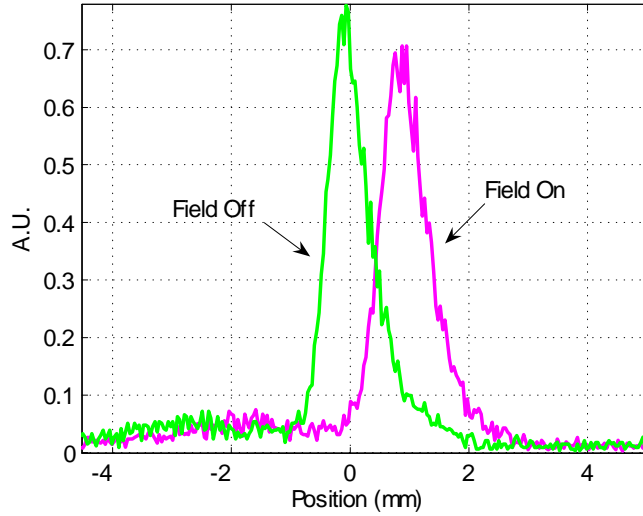


Figure 48: Na₆₀ beam profile with field on and field off.

Now we are ready to look at the beam profile we record at the TOF detector. Figure 48 presents an example of beam profiles for Na₆₀ at 20 K when the electric field is turned on and off. The x-axis has been converted from the TOF to the deflection units. The y -axis is total counts of particular size cluster. The profile is recorded over a period of time to obtain good signal noise ratio. The field-on and field-off cycles are chopped and alternated recorded to minimize the slow beam intensity variation effect. In the figure the cluster is uniformly deflected towards the strong field direction. To interpret the electric beam deflection profile we will need to establish the relation between the field-on profile P_{on} and the field-off profile P_{off} . The field-on profile is related to the field-off profile via the following convolution

$$P_{on} = P_{off} \otimes pdf(\bar{p}) \otimes pdf(v) \quad (90)$$

[109] where the $pdf(\bar{p})$ is the polarization distribution, $pdf(v)$ is the velocity distribution (will be discussed in the following section and so for simplicity we assume speed is uniform $pdf(v) = \delta$ -function, so $P_{on} = P_{off} \otimes pdf(\bar{p})$). The field-induced beam broadening as mentioned earlier is not included in Eq. 90. But this effect can be estimated empirically as well be described later in section 3.6.2.

In principle the field-broadening contribution $f_{field-broadening}$ can be subtracted off and one measures the $pdf(\bar{p})$ so one can in principle deconvolute P_{on} with $P_{off} \otimes pdf(v)$ to get $pdf(\bar{p})$. In practice the field broadening is subtracted empirically. Also the distribution of velocity is normally very small, (see the speed measurement section for justification, <1%) so one can treat $pdf(v)$ as a delta function. So one arrive at a point where we can avoid the deconvolution process which is normally very sensitive to noise and not easy to implement, and resort to simple profile moment analysis to understand the characteristics of $pdf(\bar{p})$. So although in theory one can simulate the entire experimental profile and then compare with the data, in practice too many experimental parameters need to be tuned. Therefore moment analysis is used instead. The effect of convolutions on several distributions is equivalent to an increase in the second moment of the distributions (as explained in the following).

Consequently one can fit two Gaussians to both the field on and field off profile and obtain the difference in the average positions which will correspond to the beam deflection. As for a spherical rigid rotor, which possesses intrinsic dipole moment, we will also find later the $pdf(\bar{p})$ is a logarithmic distribution.

3.6.1 To Get the Polarizability

It is straightfoward to get the polarizability from the deflection profiles. For a polarizable rigid rotor, the average of the $pdf(\bar{p})$ corresponds to the polarizability. From basic moment analysis we know that the average of the P_{off} will also be the average of the P_{on} because $pdf(\bar{p})$ and $pdf(v)$ are both symmetric function. Thus by taking the difference of the two

means, one finds the shifted function $pdf(\bar{p})$. Gaussian fits are used to find the means of the beam profiles P_{on} and P_{off} . The difference in the two means is the average deflection.

3.6.2 To Get the EDM

For an intrinsic dipole moment the polarization distribution is a logarithmic function for spherical clusters where $pE \ll kT$ (see Section 3.5.2). After convolution with the off-field profile P_{off} , we obtain the corresponding broadening in the on-field profile P_{on} . The second moment of the logarithmic polarization distribution is $\frac{p^2}{9}$ (From Eq. 4). Consequently

$$\sigma^2(P_{on}) = \sigma^2(P_{off}) + \frac{p^2}{9} \quad (91)$$

where σ is the standard deviation (width). Hence we find the dipole moment p . Due to the symmetric nature of the logarithmic polarization distribution we should see the field-on profile P_{on} broadens, giving intensity at both sides of field-off profile P_{off} (or towards both the high field and low field direction).

To empirically correct for the field induced broadening (and also the scattering induced beam width broadening) the following empirical method is used. Step by step procedure is described:

Experiment 1 (ex1). Electric field is turned off. Focus on large clusters, since scattering has less effect on the heavy clusters. (One can verify this by observing that the width of the peak as a function of N is asymptotically approaching a constant near $N = 200$, see Figure 83.) The width of the field off peaks of the large clusters will be simply related to the

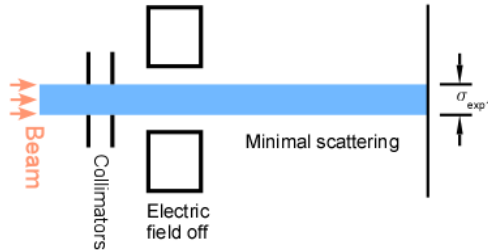


Figure 49: (exp1) Electric field off and focus on the large clusters. One can get the width of the collimated profile.

collimator geometry:

$$\sigma_c^2 = \sigma_{ex1}^2 \quad (92)$$

where σ_c is the beam width due to the geometrical factors.

Experiment 2 (ex2). Electric field is on. Scattering of smaller clusters cause the width of the beam to increase. This will be the case when the field is off and for the clusters smaller

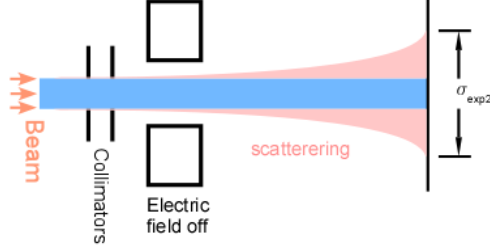


Figure 50: (exp2) Electric field on and focus on the small clusters. One can get the width contribution from the scattering.

than a certain size ($N < N_c$). Then the observed width in this experiment can be written as

$$\sigma_{ex2}^2 = \sigma_c^2 + \sigma_s^2(N) \quad (93)$$

$$= \sigma_{ex1}^2 + \sigma_s^2(N) \quad (94)$$

$$\therefore \sigma_s^2(N) = \sigma_{ex2}^2 - \sigma_{ex1}^2 \quad (95)$$

where we assume that the scattering will give an effective width of $\sigma_s^2(N)$ (because effect of scattering is equivalent with convoluting a scattering function with the original beam profile. See Eq. 90.)

Experiment 3 (ex3). Electric field is on. Focus on large clusters. So we will again have minimal scattering in the beam. Now the electric field will cause a field-induced broadening as we described before (see experimental section 3.4.1 and Figures 38 and 39) in the beam. To a good approximation the field broadening increase the effective width. Consequently

$$\sigma_{ex3}^2 = \sigma_c^2 + [\sigma_c C_1 d(N)]^2 \quad (96)$$

$$= \sigma_{ex1}^2 + [\sigma_{ex1} C_1 d(N)]^2 \quad (97)$$

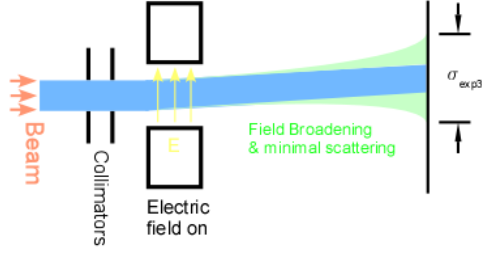


Figure 51: (exp3) Electric field is on and focus on the large clusters. One can get the field broadening contribution to the width.

$$\therefore C_1 = \frac{\sigma_{ex3}^2 - \sigma_{ex1}^2}{\sigma_{ex1}^2 \cdot d^2(N)} \quad (98)$$

where we approximate the field broadening with a factor $C_1 d(N)$, $d(N)$ is the average deflection of the beam (because field-induced broadening will be proportional to the deflection) and C_1 is a proportional factor we want to find out.

Experiment 4 (ex4). Electric field is turned on. Scattering of smaller clusters cause the width of the beam to increase and field broadening is also included. Now we choose the magic number clusters (2, 8, 20, 40, 58, 92, 138, 196, ... etc.) so that the beam will not be broadened due to the dipole logarithm polarization distribution broadening. Consequently Then we can write:

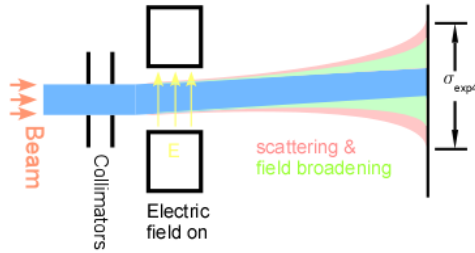


Figure 52: (exp4) Electric field is on and focus on the magic number clusters. One can obtain the scattering and field broadening contribution to the width.

$$\sigma_{ex4}^2 = \sigma_c^2 + [\sigma_c C_1 d(N)]^2 + \sigma_s^2(N) + [\sigma_s(N) C_1' d(N)]^2 + \underbrace{\sigma_{dipole}^2(N = magic\ number)}_{=0} \quad (99)$$

Here we also approximate the induced field broadening for the scattering part has an convolution effect, so a factor proportional to the average deflection is introduced $C'_1 d(N)$ (where C'_1 is the proportional factor we want to find out) in to the second moment addition. The last term is zero because we only look at the spherical clusters which can not have no dipole moment due to inversion symmetry.

$$\sigma_{ex4}^2 = \sigma_{ex1}^2 + (\sigma_{ex3}^2 - \sigma_{ex1}^2) + (\sigma_{ex2}^2 - \sigma_{ex1}^2) + [(\sigma_{ex2}^2 - \sigma_{ex1}^2) C'_1 d(N)]^2 \quad (100)$$

$$\therefore C'_1 = \frac{(\sigma_{ex4}^2 - \sigma_{ex3}^2) - (\sigma_{ex2}^2 - \sigma_{ex1}^2)}{(\sigma_{ex2}^2 - \sigma_{ex1}^2) \cdot d^2(N)} \quad (101)$$

In this way we can empirically get the C_1 and C'_1 factors. So we can plug this back into Eq. 99 for all clusters

$$\sigma_{ex4}^2 = \sigma_c^2 + [\sigma_c C_1 d(N)]^2 + \sigma_s^2(N) + [\sigma_s(N) C'_1 d(N)]^2 + \underbrace{\sigma_{dipole}^2(N)}_{\frac{v^2}{9}} \quad (102)$$

and empirically subtract off the first several terms of broadening and obtain a good estimate on the electric dipole moment contribution $\sigma_{dipole}^2(N)$. Gaussian fitting procedure is used to find the width.

3.7 Speed Measurements

To measure the speed we use the following chopper technique. The idea is to mechanically create a temporally depleted region in the cluster beam by means of a chopper. We can detect the intensity reduction at the detector when the chopper blocks the beam. (see Figure 53). When the intensity at the detector is at a minimum, the chopper is synchronized with beam pulse, and we know the traveling time. Combined with the known length of the beam path we can calculate the speed.

The chopper is located at the exit of the first skimmer. The chopper consists of a rotating blade which has slits at either end. The chopper blade is attached to a motor and the chopper rotates perpendicular to the beam (See Figure 53). As indicated in the figure the chopper creates two depleted regions but allows a narrow pulse of clusters to be transmitted. For a full description, the timing sequence and more details, refer to Moro's

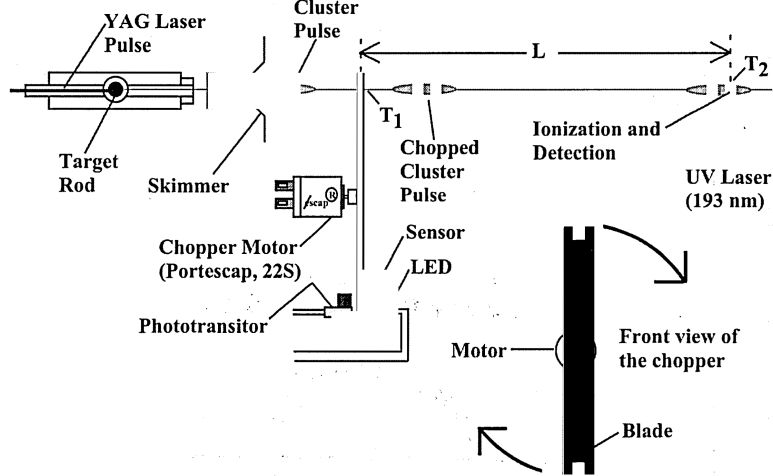


Figure 53: Setup of the chopper. The geometry of the chopper is on the right bottom. A courtesy figure from [80].

thesis[80]. The frequency of rotation is precisely controlled and a typical value is around 100Hz.

Because we have a TOF mass spectrometer as our detector, we can record the speed for all size clusters simultaneously. The 3-D Figure 54 shows the depletion in the cluster beam pulse created by the rotating chopper for all cluster sizes. The z axis represents the intensity of the clusters, y axis is the spatial position of the beam (converted from the chopper time delay, see [80]), and the x axis is the cluster size. The double minima structure due to the slit in the blade is clearly observed. Note that the small bump structure in the middle of the valley is distinct. The minimum position of the depleted region gradually shifts toward higher speeds for the smaller clusters. Also, the intensity of the middle bump is reduced for smaller clusters. This feature indicates that the spread in the speed distribution is greater for smaller cluster sizes.

Each cluster size has a distribution of speed $f(v_N)$ from which we can define an average speed u_N and a standard deviation σ_N . (Eq. 103 and Eq. 104)

$$u_N = \int v_N f(v_N) dv_N / \int f(v_N) dv_N \quad (103)$$

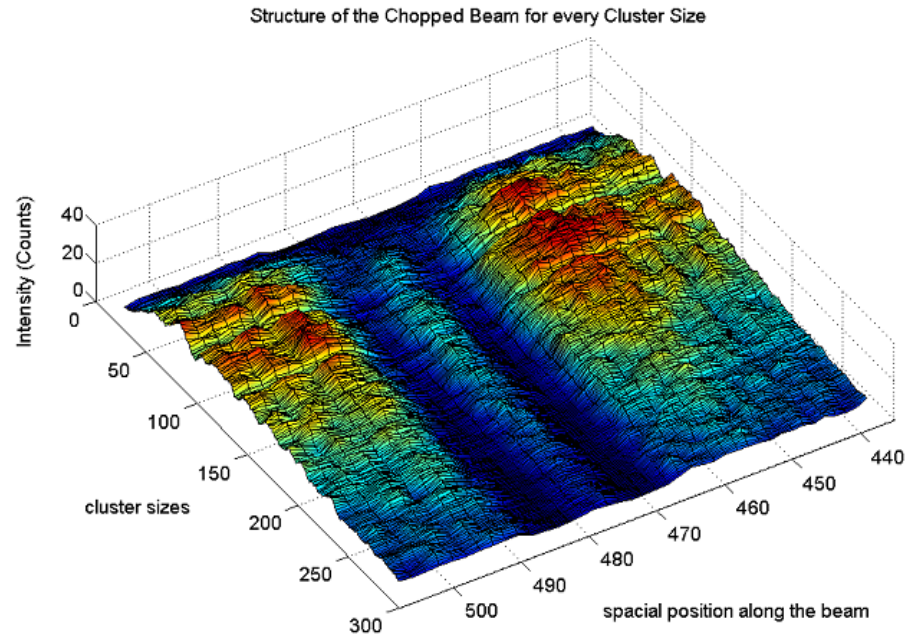


Figure 54: A spacial representation of middle portion of the clusters beam pulse, showing the intensity distribution of clusters in the beam and the depleted regions caused by the rotating chopper. Z-axis is the cluster intensity, x-axis are the spacial position along the beam streamline and y-axis showing the cluster size.

$$\sigma_N = \int v_N^2 f(v_N) dv_N / \int f(v_N) dv_N \quad (104)$$

To determine the uncertainty in the average speed for clusters u_N of a size N . We first locate the position of the bump structure in the middle of the valley in the 3-D speed chart (Figure 54). The uncertainty in the position of the maximum can be estimated by taking the maximum and dividing by the square root of the lost intensity counts. This is because for a Gaussian peak an estimate for the uncertainty in position of the mean μ , is σ/\sqrt{N} [15], where N is the total counts and σ is width of the Gaussian. The relative error of the average speed, is found to be 0.2% for middle size clusters.

The uncertainty in the spread in speed σ_N for cluster of a size N can be estimated by $\sigma/\sqrt{2N}$ [98] using the same Gaussian estimation method. In principle, we should perform a deconvolution using the chopper impulse response function to find the speed distribution (see Moro[80]). However this deconvolution is very sensitive to noise. Despite the deconvolution difficulty, one can qualitatively see the spread in the speed distribution by the contrast of the middle bump and note that the spread is very small due to the good jet expansion conditions. An approximate estimate on σ_N is less than 0.5% of the average speed. If we only want to measure the polarizability, the average speed is the only speed parameter that is important (see Eq. 90 and the discussion).

3.8 Detection and Recording of Spectrum

To determine the beam constituents as well as the beam deflection, we use a Time-of-Flight mass spectrometer, shown in Figure 55. (For a detailed description see [80]) The clusters are ionized in the detector chamber with a light pulse from an excimer laser (ArF:193nm or KrF:248nm) or an tunable OPO laser (205nm~700nm). The cluster ions are then detected using a time-of-flight mass spectrometer. The spectrometer consists of a series of electrostatic plates and grids which generate electric fields to accelerating the cluster ions towards an ion collector. The arrival of ion at the collector is converted to a pulse of current and is further amplified and discriminated. The final signals are recorded with a fast data acquisition card (2GHz) in a computer. Because we know the voltages and

the distance between the grids, we can convert the potential energy of the ions into kinetic energy and get the relation between the resulting time-of-flight of the cluster ion mass.

$$TOF = const * \sqrt{mass} \quad (105)$$

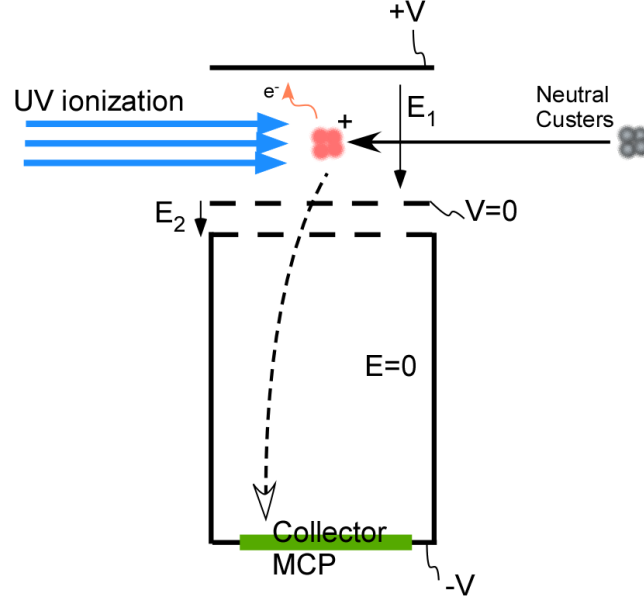


Figure 55: An illustration of the TOF mass spectrometer.

In this way one can record all the mass at the same instant, because the arrival time for different cluster is different. A typical mass spectrum is presented in Figure 56. This mode of the TOFMS is called high resolution mode.

Cluster deflections are detected also by the TOF machine but with some modification on the voltages on the acceleration grids so that the TOF is sensitive not only to the mass of particle but also to the position of the particle (see figure 57). In this mode the TOF of a cluster can be approximated and expressed as

$$TOF = \sqrt{mass} (Ax + B) \quad (106)$$

where A and B are constant to be calibrated and x is the position of the cluster with respect to the voltage grids. This position-sensitive mode of the TOFMS is quite unique.

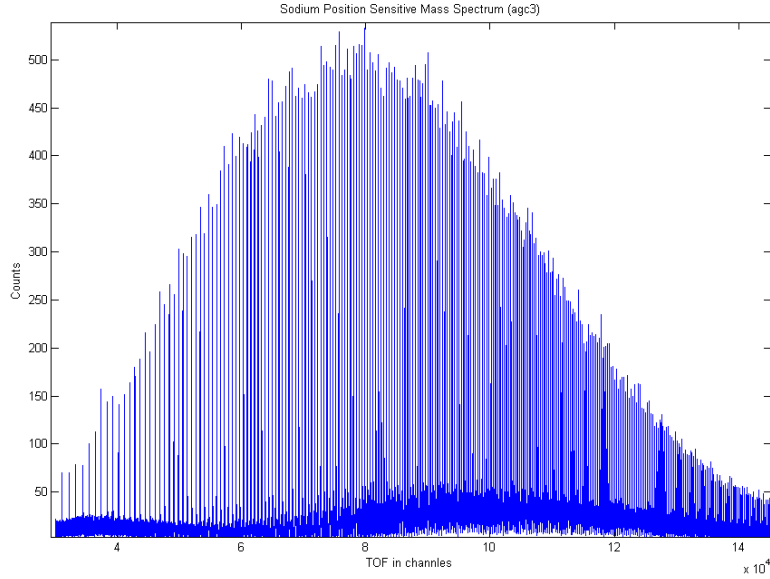


Figure 56: Typical mass spectrum of sodium clusters.

A deflection as small as $1 \mu\text{m}$ can be detected. A schematic view is illustrated below. The resolution on the mass: for high resolution $\Delta M/M \sim 1/8000$ (for $M = 2500 \text{ amu}$), for position sensitive $\Delta M/M \sim 1/1500$ (for $M = 2500 \text{ amu}$).

The abundance spectrum from TOF does not uniquely reflect the abundance of clusters in the beam. As one can easily see that the TOF mass abundance will also depend on the ionization absorption efficiency. Two ionization lasers are used. An excimer laser with two fixed wavelengths outputs at 248, 193 nm (with different working gas KrF, ArF individually.) and a OPO laser with tunable wavelength from 200 \sim 700 nm are used for ionization. (This can probe the ionization efficiency of metal clusters[108][110]. We have performed preliminary IP experiment for sodium clusters ($\text{Na}_2 \sim \text{Na}_9$) at 20 K. However due to the pointing issue of the ionization laser this experiment is not finished.)

When ionizing the neutral clusters in the beam, one has to make sure two things are correct. First is that only a single photon is involved in ionization. If second ionization occurs one can observe extra peaks in-between the peaks of the normal spectrum (See Figure 58). Second, the energy of the photon should not exceed the ionization threshold by too much, to avoid the subsequent fragmentation of the ionized clusters. Two dynamics

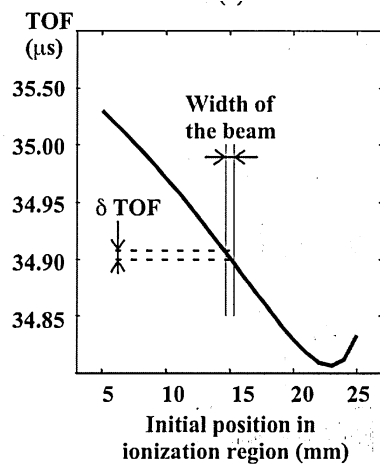


Figure 57: Position sensitive time of flight illustration. Also shown is the indication of the width of the beam and its corresponding width in the TOF time.

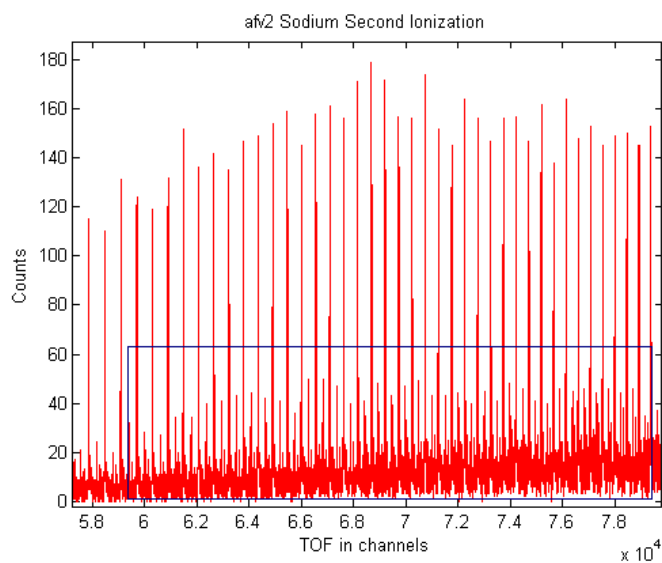


Figure 58: Second ionization of the sodium clusters. The signature pattern will emerge as extra middle peaks on top of the original spectrum. Clusters temperature are 20 Kelvin. Ionization laser is 225nm from the OPO laser.

fragmenting channels are observed if a neutral cluster is ionized with a photon with excessive energy (unimolecular dissociation)[23]. It only require about 0.9 eV to have these dissociation reactions.

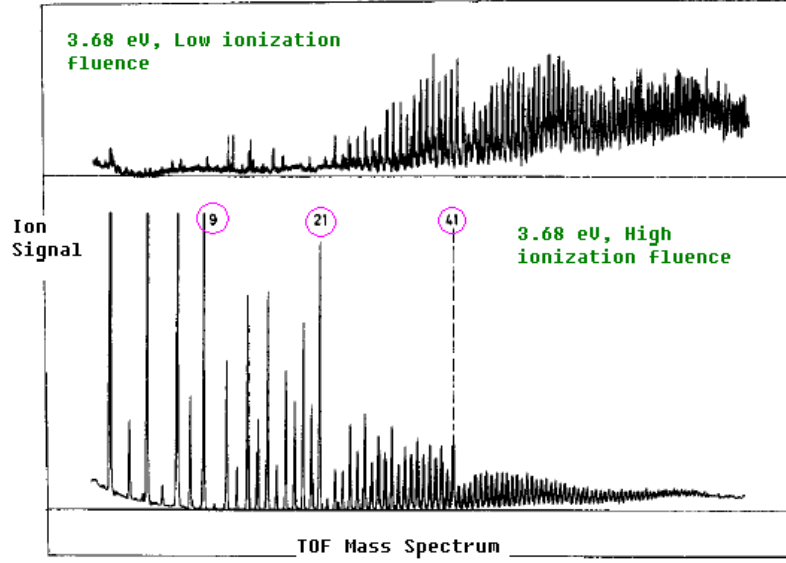


Figure 59: The upper figure is a mass spectrum using moderate ionization flux, which reflects the real neutral clusters distribution. The bottom figure is a mass spectrum with high photon flux. As one can see the clusters fragment after being ionized and the spectrum can be very different from the original. From Ref. [23].

The signature pattern of the fragmented spectrum will be the more stable clusters with one more mass number than the normal magic number in the mass abundance spectrum. (See figure 59) Note however, that our position-sensitive TOF is uniquely sensitive to these fragmenting clusters that a characteristic broadening is easily recognized. We make sure that the flux and also the energy of the ionization light does not effect the mass spectrum we observed. (Figure 60) and also it does not cause broadening in the beam width.

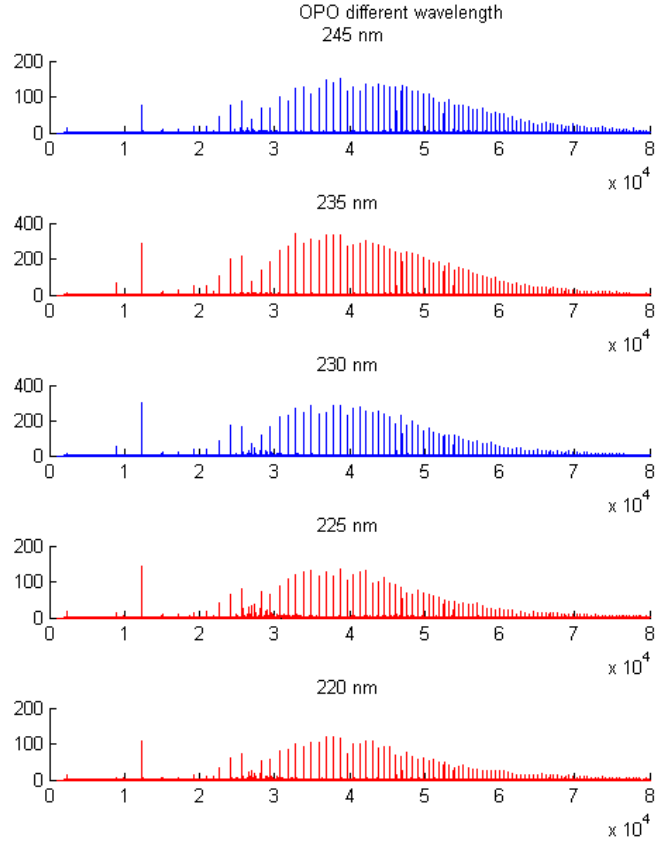


Figure 60: We can tune the ionization wavelength so that the mass spectrum of sodium clusters does not depend much on the wavelength of the ionizing light in the 220nm~245nm range. These series of experiments are tuned to a smaller size distribution. Energy flux is about $1 \sim 2 \text{ mJ/cm}^2$.

CHAPTER IV

RESULTS AND DISCUSSION

4.1 *Averaged Static Dipole Polarizability of Sodium Clusters at 20 °K*

4.1.1 Measured Results

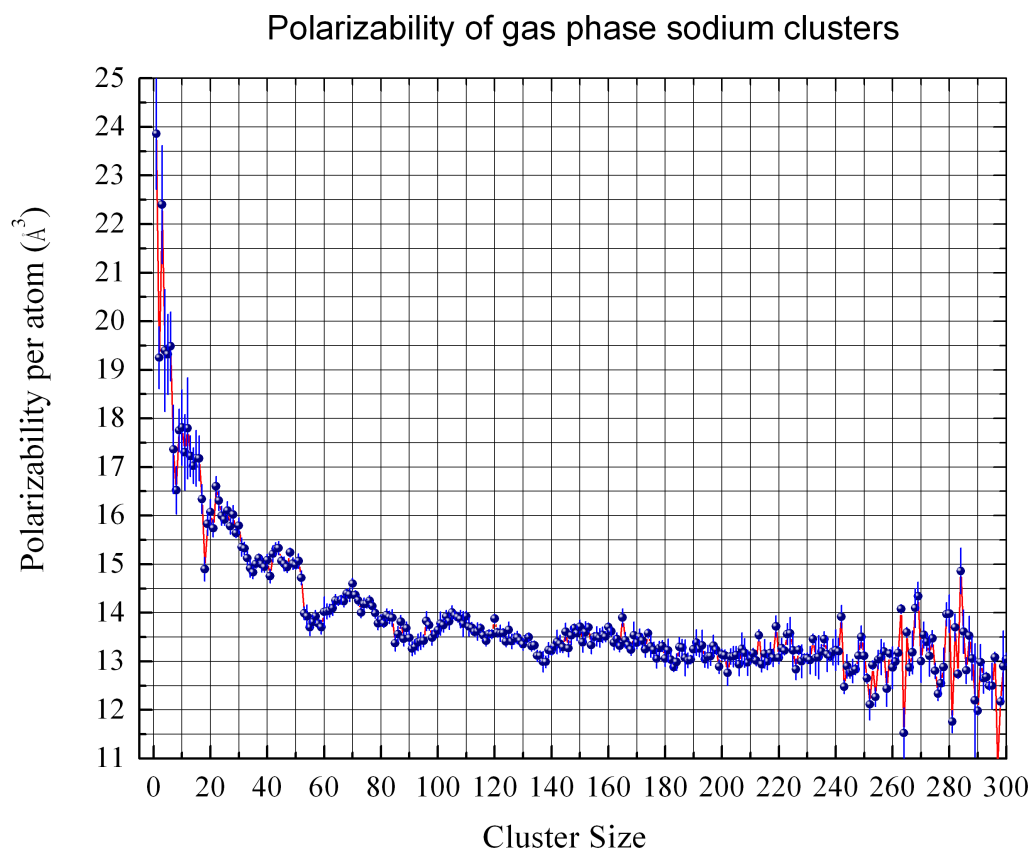


Figure 61: Average polarizability (per atom) of gas phase sodium clusters at 20 Kelvin. One can see the $1/R$ dependency and on top of it one can observe clear oscillations.

Figure 61 presents measurements of the averaged static dipole polarizability (per atom) of sodium clusters as a function of cluster size from the atom to around 250 atoms. The result is an average over many repetitions of the experiment. The data agrees globally with

earlier measurements at higher temperatures (Figure 63). The source temperature is 20 Kelvin. The fine structure in the polarizability curve is clearly visible. The general trend monotonically decreases with increasing size. The bulk polarizability of sodium metal is r_s^3 which is 9.6 \AA^3 per atom (r_s is the Wigner-Seitz radius). We can see that the trend is approaching, but does not quite reach the bulk value for sizes up to 300 atoms. This means that for sizes up to 10 nm^3 (300 sodium atoms $\frac{4\pi}{3}r_s^3 N$) the spillout is still enhanced due to finite size effects. From Chapter 2 we know that a good approximation to the polarizability is

$$\alpha(N) = 4\pi\epsilon_0 (R(N) + \delta)^3 \quad (110)$$

We can fit this curve to the measured polarizabilities of the closed shell clusters (these clusters are believed to be quasi spherical, because their filled electronic shells stabilize the cluster against Jahn-Teller distortion). From the fit we obtain two parameters: the bulk Wigner-Seitz radius ($r_s = R/N^{\frac{1}{3}}$) plus an electronic spillout (δ). (This will give respectively $r_s = 2.1 \pm 0.01 \text{ \AA}$, $\delta = 0.65 \pm 0.04 \text{ \AA}$. r_s corresponds very well with the known bulk value 2.1. δ gives a good agreement when compared with the theoretical calculated value[24].

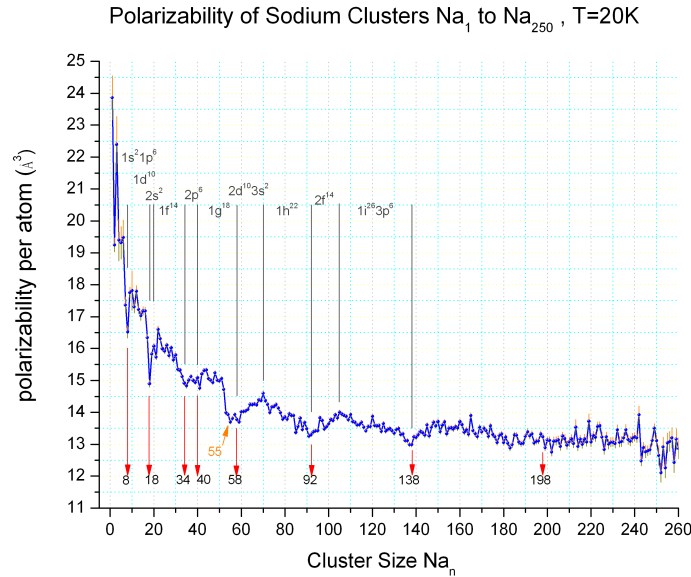


Figure 62: Polarizability curve with indications of maxima nad minima.

Now we examine the oscillations about the monotonic descent in the polarizability

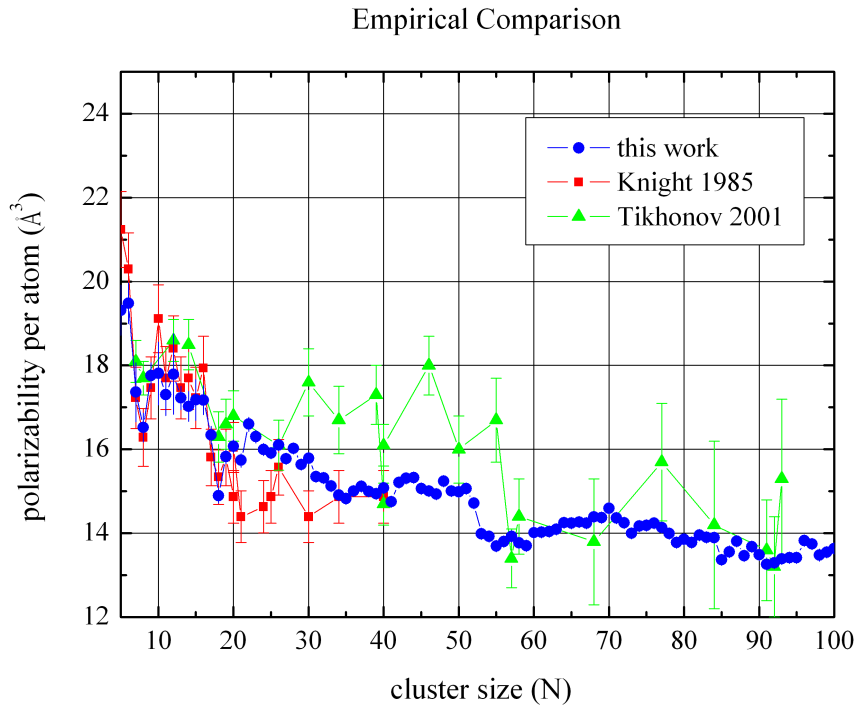


Figure 63: Our result compares with the earlier higher temperature measurements by Kresin[100] and Knight[58].

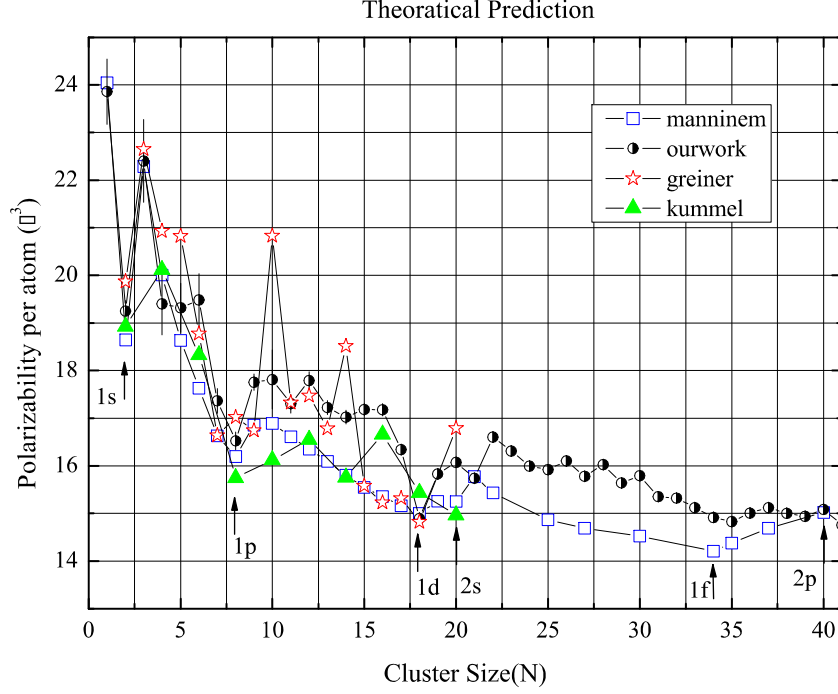


Figure 64: Compare with several theoretical predictions for small sizes, from Manninem[73], Greiner[99] and Kummel[65].

curve. The polarizability curve has several local extrema. These extrema are indicated by the arrows and vertical lines in Figure 62. The local minima occur for magic number clusters that have closed electronic shells. (cf. Table 1) It was previously assumed that the spherical symmetry of the magic-number clusters will lead to most compact electronic wavefunctions[58][100], and this will give the smallest polarizabilities.

Next we look at the maxima of the oscillations. The local maxima are at cluster sizes 70, 106, and 152+-2 (there might be a maximum at size 40 but it is not clear, but at least it is not a minimum). If we compare these numbers with the discrete energy levels of the spherical potentials in Figure 18, we see that these numbers at 70, 106 and 150+-2 are actually predicted to be spherical closed shells for an intermediate potential. But these maxima did not show up in the mass abundance spectrum experiment(cf. Table 1).

The uncertainties of the polarizabilities are the smallest in the middle size range, about 1% (20~160 atoms). For the smaller and larger cluster sizes we have larger uncertainties, because these clusters are less abundant in the beam, but it is no more than 10%. There is

an uncertainty in the absolute scale which affects all cluster sizes due to the calibration of the deflection field. This adds an uncertainty of 5%, which is not shown in the figure.

It is also noteworthy that there is an interesting flat plateau followed by a sharp dip at size 55 which does not correspond to any magic number (Figure 61). Starting from 34 the polarizabilities seem to stay constant followed by a sudden descent around 50 to a valley at 55. It is claimed that Na_{55} has a MacKay icosahedron structure[43][61], just like the Van der Waals clusters (refer to Figure 20 and discussion therein). Na_{55} has many interesting properties. For example Na_{55} shows bunching in the density of states when the cluster is measured by PES (photo-electron spectroscopy)[61]. Sodium cluster sizes which correspond to perfect icosahedra (55, 116, 147, 178 and 216) show a larger melting temperature compared to their neighboring cluster sizes[43]. However Na_{55} is the only one in the perfect icosahedra family (13, 55, 147 ...) that presents a low value in our polarizability curve. It is still unclear how the geometric structure of this cluster would reduce its polarizability. This indicates that there could be further interactions between the geometric and electronic shell structure for certain cluster sizes.

To explain the observed oscillating behavior from 58 to 192 we must keep in mind that the size-dependent polarizability of the cluster electrons is determined by the interplay of the following factors: (1) electronic shell structure (2) geometry or geometric depolarization, and (3) Surface effects (i.e., inhomogeneity of the electron density distribution or "spill-out"). We will carefully examine each of these effects quantitatively in the following sections.

4.1.2 Polarizability Enhancement due to Triaxial Ellipsoidal Distortion

From Chapter 2 we know that any shape deviation from a ideal sphere (assuming fixed volume) will lead to an increase in the rotational averaged polarizability. It has been observed that open-shell clusters can adopt a distorted shape, either prolate or oblate spheroids[32] due to the Jahn-Teller effect. Furthermore, a transition from prolate to oblate spheroid was observed in the sodium cation open shell clusters[92]. We will calculate the amount of distortion required to give the oscillations we see in the polarizability curve. We will also compare with the Clemenger-Nilson model to see if this simple model can explain the

oscillations we observe. Also we will compare our result with the polarizability extracted from photoabsorption cross-section measurement of sodium cations.

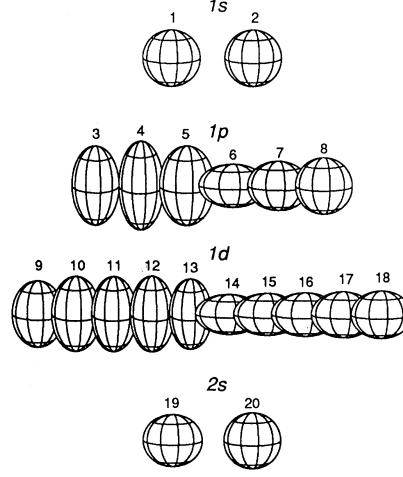


Figure 65: The suspected shapes of the sodium clusters' delocalized 3s electronic cloud (Na_{1-20}). Figure is reproduced from [32].

We will focus on two oscillations in the polarizability curve, one from a minimum at 58 to a maximum at 70 back to a minimum at 92, and another from a minimum at 92 to a maximum at 106 back to a minimum at 138. They are clearly shown in Figure 61. From the derivation in chapter 2 we can estimate how much distortion from a spherical shape would be required to explain the enhancement polarizability at the maximum we see in the experiment. Starting from a closed magic number cluster, as one adds more atoms to the clusters, the shapes of the clusters are believed to adopt a prolate (with increasing longer axis) and then an oblate shape (with decreasing shorter axis) as atoms are added until the next magic number is reached[44]. The transition from prolate to oblate will give a maximum in polarizability. We convert our experimental results to the distortion parameters as a function of size (by using Eq. 19 in Chapter 2.1) and the estimated distortion parameter is plotted in Figure 66.

We compare the empirical distortion parameters with the distortion expected in the

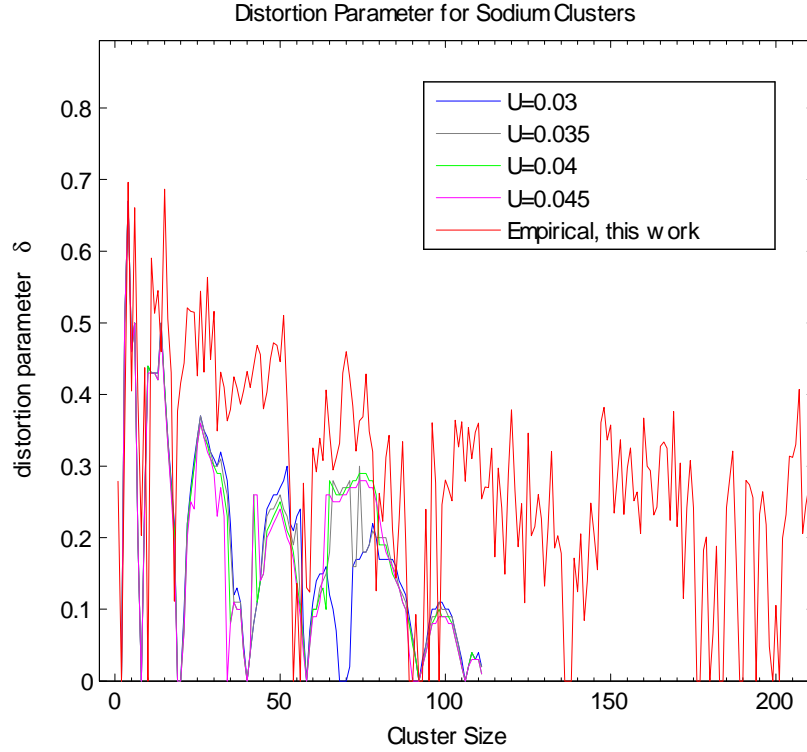


Figure 66: Distortion parameters $\delta = \frac{R_z - R_x}{R_z + R_x}$. Red: the amount which clusters need to deviate away from a sphere in order to account for the oscillation seen in our experiment. The other four: Clemenger-Nillson model with four different parameters U .

simple Clemenger-Nilsson model[29] (include all four anharmonicity parameters they considered). The calculated distortion parameters from the Clemenger-Nilsson model are presented in Figure 66. One can clearly see some discrepancies. First at cluster sizes 40 and 106 the model actually predicted a close shell structure and so distortion parameters are zero and they are minima. But instead what we observed is that the distortion parameter at size 40 is not a minimum and distortion parameter at size 106 is actually a maximum. One can see that from cluster size 58 to 92 the model predictions a distortion consistent with a 10-15 % enhancement of α but we observed 20 %. The distortion contribution can only account for about three-fourths of the observed distortion. The maxima at 70 is distinct in our measurement however it is somehow smooth (or might not have a maximum) at size 70. From 92 to 138 the predicted distortion contribution to α is much less than the observed enhancement. These facts suggest that the oscillations we see can not be simply explained by Jahn-Teller distortion of the clusters shape. The expected enhancement of the polarizability due to distortion does not correspond to what we observed in the experiment.

The photoabsorption cross section measurement probes the collective resonance modes of all the electrons and is related to the polarizability tensor of the clusters, see Appendix B. Experimentally de Heer and Selby measured the photoabsorption cross section for small neutral sodium clusters (less than 40 atoms) [97] and Haberland et al. repeated this experiment for sodium clusters cations (up to 64 atoms) [92]. There is a direct relation between the polarizability tensor and the photoabsorption cross section. One can actually convert the measured photoabsorption cross section to get the diagonal part of the polarizability tensor. In the appendix this important relation is briefly explained. The distortion parameter (or deformation parameter) converted from the photoabsorption experiment of the sodium cluster cations are plotted in Figure 67. One can see in general the distortion parameter (or deformation parameter) is very small, smaller than we actually observed (cf. Figure 66). The average polarizability converted from the same experiment of sodium cation photoabsorption measurement is presented in Figure 68. One can see that the polarizability of a cation cluster is equal to the polarizability of a neutral cluster with same number of valence electrons, at least for sizes larger than 18. This actually suggests that the

polarizability depends primarily on the number of valence electrons. The ion cores, and the cluster neutrality has only a weak effect. However the largest cluster in their experiment is 65 atoms so we can not yet compare our interesting maxima (70, 106 and 152) with their result.

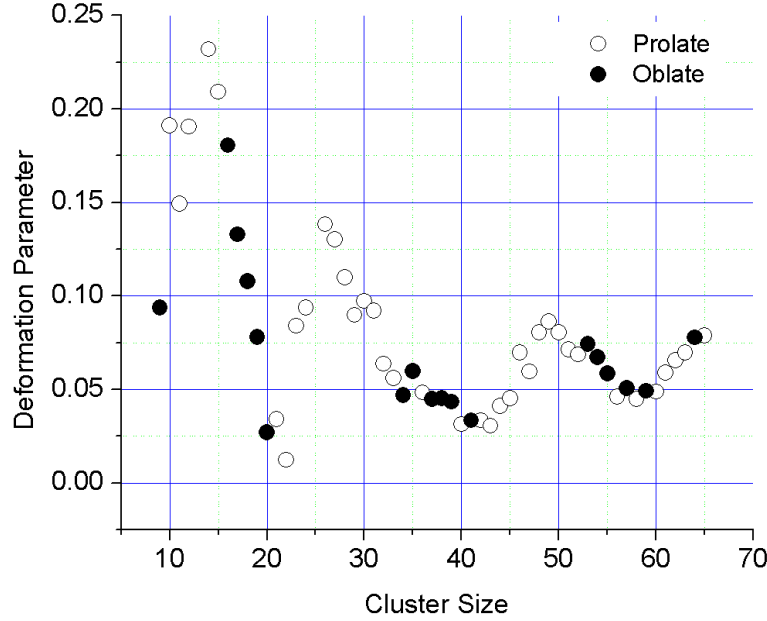


Figure 67: Deformation parameters extracted from the photoabsorption spectrum obtained by Haberland et al with the sodium cationic clusters. Regraphed from [92].

4.1.3 The Effect of Electronic Shell Structure on Polarizability

We have shown that the oscillations in the polarizability curve can be partially explained by the distortion of the cluster's shape away from a perfect sphere. It is important to emphasize that this is not the only possible explanation. In fact, spherical clusters will show oscillations in the polarizability due to the orthogonality requirement of the electronic wavefunctions. This effect is entirely electronic and involves no distortions. Several theories have already predicted this effect using the spherical jellium model[86][73][35]. More specifically, note that the local maxima of the polarizability occur at the cluster sizes where a new shell is opened with the principal quantum number 1 (see Figure 70).

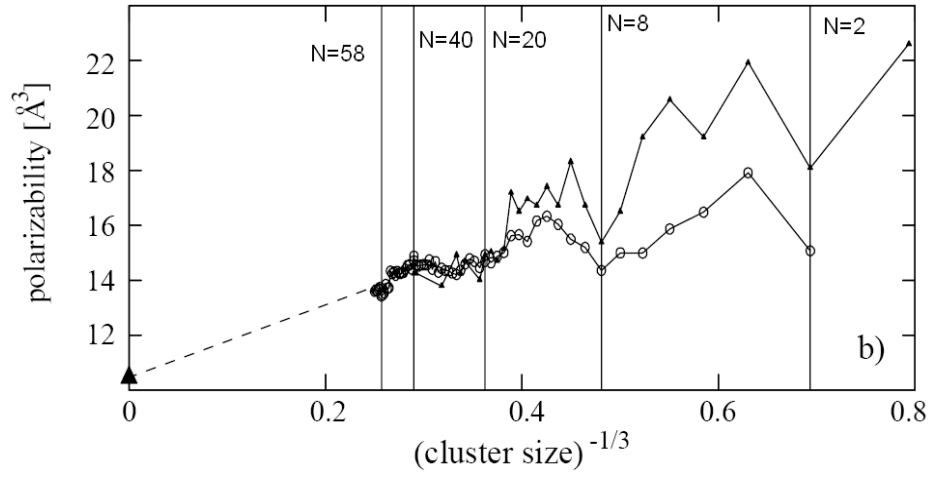


Figure 68: Polarizability per 3s electron of neutral (dots, from [58]) and charged sodium clusters (Na_x^+ , open circles, [92] and this is also the source of this figure). The plot for neutral clusters has been shifted by one mass, so that clusters with the same number of valence electrons are vertically above one another.

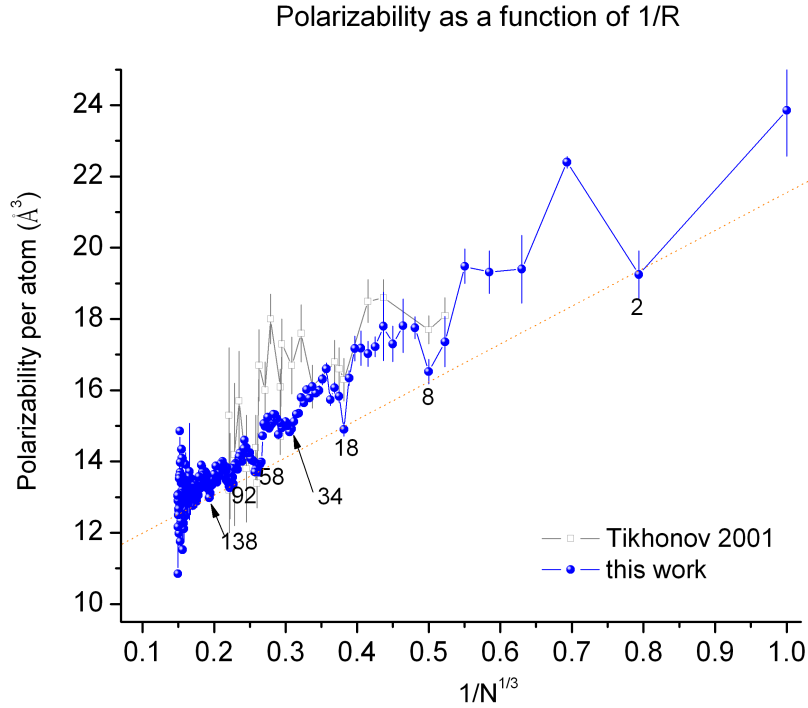


Figure 69: Experimental polarizability per atom as a function of $\frac{1}{N^{1/3}}$. (This work)

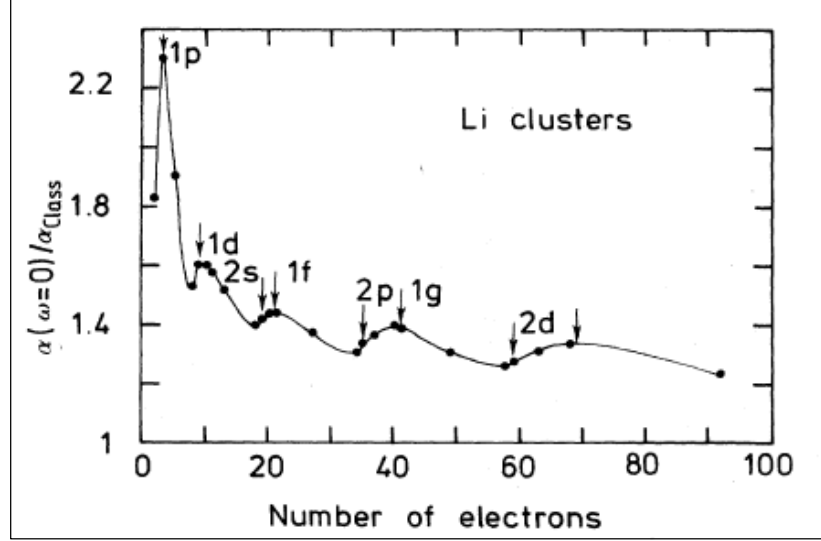


Figure 70: A theory predicted oscillation in the polarizability curve of alkali clusters (scaled to the bulk polarizability α_{classic}). All clusters are assumed to have a spherical shape. The arrows indicate the opening of a new shell right after a shell closure. From Ref. [86].

Puska et al. performed a LDA spherical jellium calculation and predicted the polarizabilities for alkali and aluminum clusters[86] (see Figure 70 for a prediction of lithium clusters). The theoretical polarizabilities of the predicted closed-shell clusters emerge as local minima and maxima in the polarizability curve. Therefore we can compare our result with theirs, Fig 71. From this theory we can write down the electronic shell configuration[66] in analogy to the atomic electronic configuration

$$1s^2 1p^6 1d^{10} 2s^2 1f^{14} \mid \overset{40}{2p^6} \mid \underset{34}{1g^{18}} \mid \overset{58}{2d^{10}} 3s^2 \mid \underset{58}{1h^{22}} \mid \overset{70}{2f^{14}} \mid \underset{92}{1i^{26}} 3p^6 \mid \overset{106}{2g^{18}} \mid \underset{138}{1j^{30}} 3d^{10} 4s^2 \mid \dots \quad (111)$$

Bar lines correspond to the magic numbers we identify in our measurement. The numbers above and below the bars correspond to the maxima and minima in polarizability. The opening of a new shell occurs right after a shell closure at the bars.

The reason that the polarizability curve has oscillations can be understood from the following argument. First if we look at the electronic configuration Eq. 111 and the theoretical polarizability curve in Fig 70 we will notice that the polarizability maxima always precede the opening of the next angular momentum shell with principal quantum number 1. And the polarizability minima always precede the opening of shell with principal quantum

number 2. For example the next electron added to the system after 70 opens the 1h shell, and the next electron added to the system after 106 opens the 1i shell. And minima at 34, 58, 92 and 138 open the second principal quantum number states $2p$, $2d$, $2f$ and $2g$. It is when filling the states with first principal quantum numbers that the polarizability curve decreases, and filling a level with principal number 2 will cause the polarizabilities to increase. This is because when filling the states with second principal quantum number (when $n=2$) the electronic wavefunctions are required to be orthogonal and in order to remain orthogonal the radial part of the electronic wavefunction must extend outward and thus increase the spillout[73]. This will give rise to a larger polarizability, which is a measure of the extent of a wavefunction. When filling the states with first principal quantum number there are no angular momentum states with smaller principal quantum number. So the polarizability per atom will decrease due to the decreasing surface to volume ratio. This explanation is tentative and requires deeper theoretical study.

To elucidate the idea, Figure 71 shows the predictions for sodium, lithium and aluminum clusters polarizabilities compared with our measurements. The oscillation amplitudes of the predictions seem to describe the trend in the experiment without any need to invoke the cluster's deformation. The predictions agree very well with the observations up to sizes of 198. However the predicted polarizabilities for the sodium are systematically about 25% lower than our sodium observation.

Our result is probably the first complete polarizability measurement that enables the theorists to study this intermediate size range. For large clusters our observed magic numbers differ from the theoretically expected values by one or two atoms. This is not surprising when one looks at the magic number table (Figure 1), deviations can be found among large cluster sizes. At higher temperature Bjørnholm explained this in the following way. With an increasing number of shells, confined to an energy interval about equal to the Fermi energy / number of atoms, the gaps at the closed shells will slowly diminish as size increases. At finite temperature electrons can be excited across the gaps, and this tends to smear out the magic numbers[18]. In our low temperature measurement we expect the clusters to be in their electronic ground state for all sizes up to 300 atoms so the most likely explanation

for the apparent deviation is the experimental uncertainty in determining the maxima or minima.

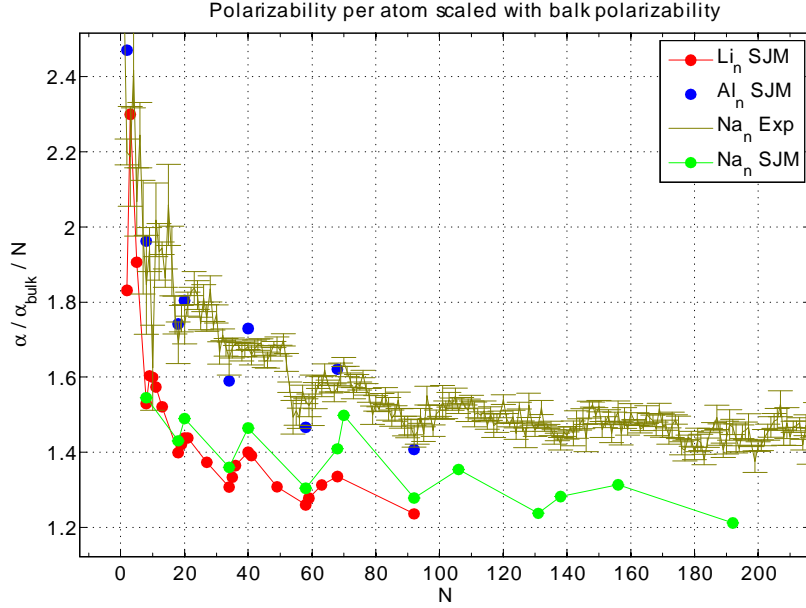


Figure 71: Polarizability ratio curve $\alpha/\alpha_{\text{bulk}}$ from our result and from the spherical jellium theoretical predictions. The $\alpha/\alpha_{\text{bulk}}$ is essentially $(1 + \delta/R)^3$ so this figure gives us an idea how does the spillout scale with the size when compared to the bulk counterpart.

The maxima in the polarizability curve should keep follow the orthogonality requirement when the size gets larger. Unfortunately for cluster sizes of 260 and above we lose precision due to the limitation in determining the mean of our beam profile. We suspect the next maximum should come in around 220 atoms. I could not find any theoretical prediction larger than Eq. 111 and Figure 71. It would be very interesting experiment to check the correspondence of these oscillations for larger cluster sizes. (Another interesting data point is cluster size 120, for every experiment we ran the polarizability curve seems to consistently give a peak at cluster size 120. With 119 electrons the cluster is actually the half-full $1i$ level, see Eq. 111, after the closure at 106.)

There is further experimental evidence which suggests cluster sizes 70, 106, and 152 have special properties. In 1999, Bjørnholm obtained the separation energy for the sodium clusters [17] from vacuum evaporation (See Figure 28). At that time they realized the

separation energy curve shows maximum at the magic numbers 58, 92, 138 and 192, meaning that these clusters need more energy to dissociate than their nearest neighbors. These are consistent with the higher stability of the closed shell magic number clusters. However, what they did not realize is that, as we closely observe the curve, the minima in the curve correspond to those clusters show a local maxima in our polarizability measurements, that is, the sizes 70, 106 and 152. The minima in separation energy suggest that they are relatively unstable (need comparably smallest amount of energy to dissociate). At that time theorists tried to obtain the experimental separation energy with a model of deformed shape but could not get a very satisfactory result[17] (see Figure 73). Also the oscillation pattern we see in the separation energy curve closely follows the oscillations we have observed in the polarizability.

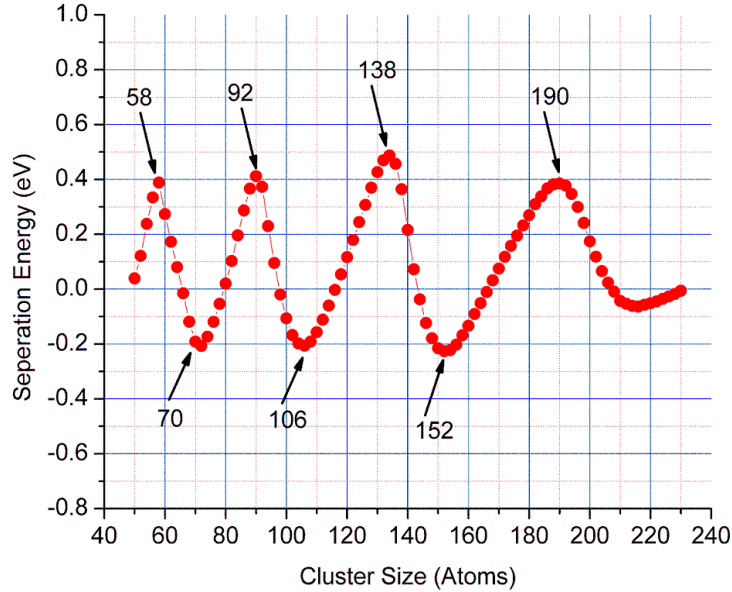


Figure 72: Experimental separation energy as a function of size from the experiments. The polarizability maxima numbers we observed actually correspond with the minima in experimental shell energy. Figure is regenerated from[17].

So it seems that the polarizability curve and separation energy curve are somehow related, although they result from very different physical processes. However if we just focus on sizes 70, 106 and 152 ± 2 , we can qualitatively describe the correlation between the

these two properties. The separation energy depends most directly on the binding energy of the atom in the clusters. The polarizability per atom is a measure of the volume of the cluster. The cluster sizes which correspond to a local maximum of the polarizability curve will have a larger volume per atom than their neighbors, and thus we would expect the average bonding energy to have a local minimum because the atoms are less tightly bonded. The binding energy will thus have a local minimum where the polarizability shows a local maximum. So there is a possibility that these numbers (70, 106, 152±2) could be magic numbers, but because they have a minimum of the binding energy they do not stand out in the mass abundance spectrum and ionization potential.

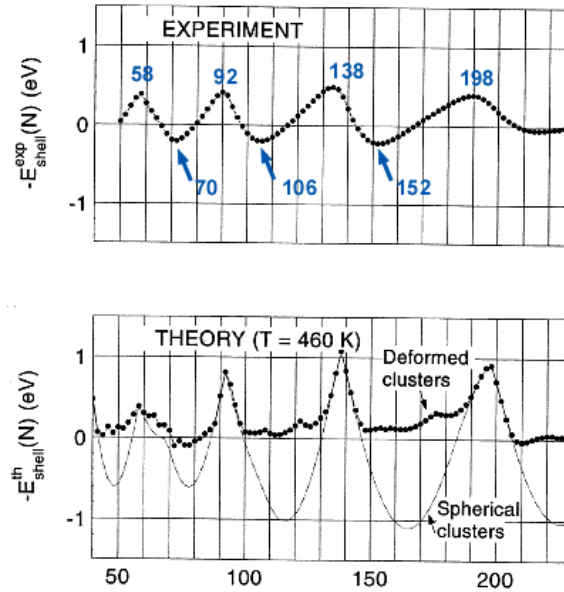


Figure 73: Experimental and theoretical shell energy as a function of size from the experiments. The theory is based on a deformed clusters shape (lower graph)[17].

Another way to study the electronic shell structure is to measure the photo-electron spectrum (PES). This has been carried out by von Issendorff's group[61][10] on sodium anion clusters. The magic numbers for the anion clusters are offset by one from the magic numbers of the neutral clusters. This is clearly shown in the photoelectron spectrum[61]. Notice that for Na_{70}^- they do not observe the opening of a new shell in the DOS. When they compared with theoretical calculation the PES reveals that the atomic arrangement

of Na_{70}^- has a icosahedra core packing with a cap (three adjacent triangular atoms faucets). However the orthogonality requirement is not considered in the model where DOS of Na_{70}^- in the PES was obtained. There could be other effects that the orthogonality requirement will cause in the PES measurement.

Although a distortion from a sphere can further give rise to an enhancement in average polarizability, the discussion in this section illustrates that there are other entirely electronic explanations for the oscillations. There is much experimental evidence that smaller clusters have non-spherical shapes, so these simple models which assume a spherical shape are not directly applicable. Despite this the good agreement between the predictions of the spherical jellium model and the experimental measurements suggests that the electronic explanation holds for medium cluster sizes.

4.2 *Upper Bound on Electric Dipole Moments of Sodium Clusters*

Our estimate of the electric dipole moments of sodium clusters are presented in Figure 74. Recall that the EDM (p) is extracted from the broadening of the beam profile by the equation

$$\frac{p^2}{9} = \sigma^2(P_{off}) - \sigma^2(P_{on}) - \sigma_{corr}^2 \quad (112)$$

In the equation above σ_{corr} represents the change in the profile width due to field broadening and other aberrations discussed in section 3.4.1.

Several measurements of the electric dipole moment are presented together to illustrate the statistical variance in the measurements. The values oscillate around zero, which suggests that the dipoles could be all zero or very small. The amplitude of the fluctuations gets larger as the size increases. This is due to the fact that in our measurement the broadening of the beam profile is determined by the dipole moment per atom rather than the total dipole moment. When we multiply the dipole moment per atom by the number of atoms to get the total dipole moment, the small noise in the signal is also multiplied by the number of atoms (see Eq. 53 for details). The dipole moment per atom is shown in Figure 76. The important thing to note is the small magnitude of the moments even with the noise - for

all cluster sizes less than 50 the total dipole moment is no more than 0.1 Debye.

Figure 75 presents a comparison between our result with the theoretical predictions of Greiner et. al. [99] for the small clusters ($N \leq 20$). The experimentally measured dipole moments are at least an order of magnitude smaller than the predictions. For certain cluster sizes the theory predicted the existence of zero dipole moment isomers (they are indicated by square at zero dipole moment). However, from cluster with sizes ranging from 11 to 18 atoms there are no zero dipole moment isomers and the dipole moment predicted are much larger than measured in the experiment.

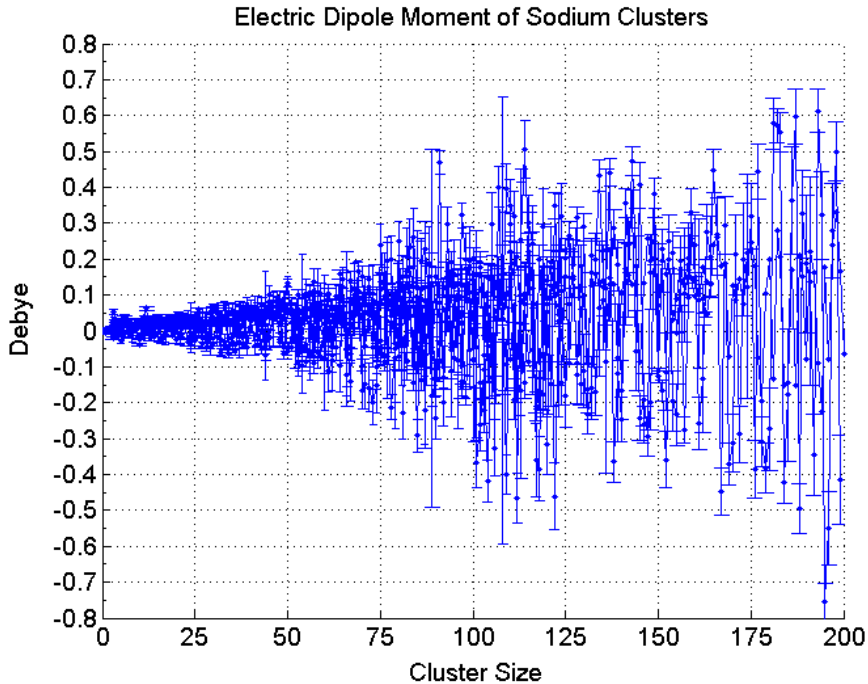


Figure 74: Electric dipole moments (EDMs) of neutral sodium clusters.

The only clusters we suspect to have a small dipole moment are Na_3 and Na_6 . These two will be discussed in the following section.

It is interesting that theories have predicted permanent electric dipoles exist in the alkali clusters. This is contradictory to our basic intuition about metals. The presence of a dipole moment implies the existence of large internal electric fields which should be screened by the delocalized conduction electrons. The electric fields associated with an electric dipole

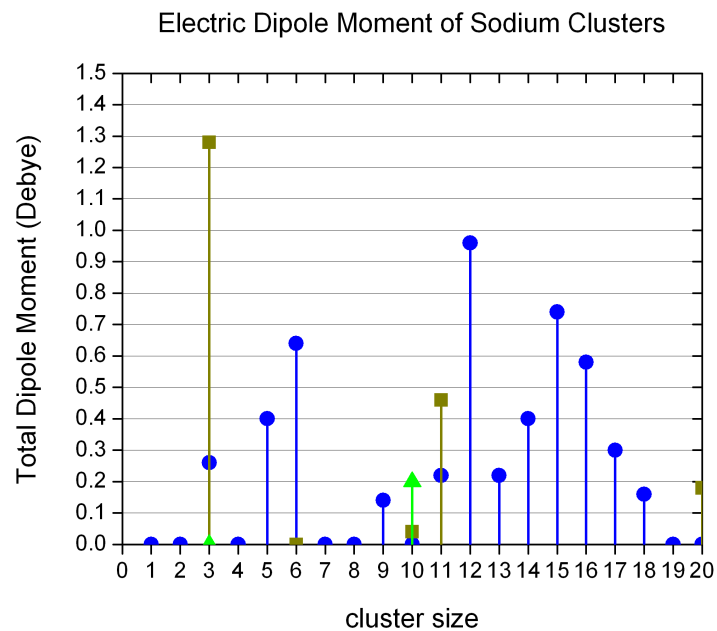


Figure 75: EDM of the small sodium clusters ($\text{Na}_{1\sim 20}$) from the theoretical predictions[99].

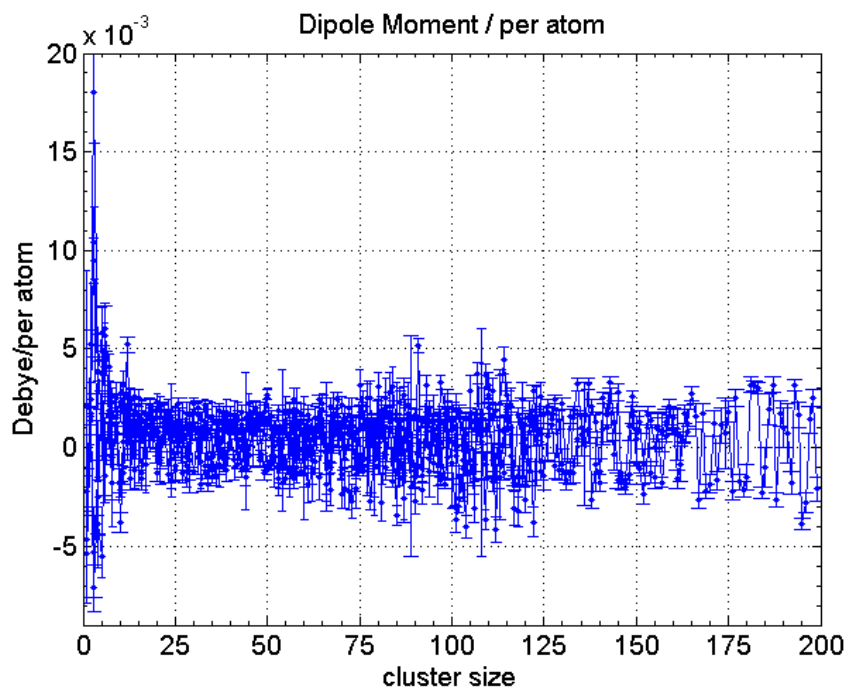


Figure 76: EDMs per atom.

moment in a cluster will cause a large potential difference across the cluster. For example, the predicted dipole moment $P = 0.1$ Debye in Na_{10} , according to Eq. 6 in chapter 2, would cause a voltage difference $V = 0.3$ Volts across the cluster. The corresponding dipole energy of 0.1 Debye is, according to Eq. 5, 3.4 meV. In contrast we find that $P < 0.05$ Debye, so that $V < 12$ mV and dipole energy $< 10^{-3}$ meV. Experimentally, for sodium clusters at least, we found that the screening ability of the electrons is found to persist up to the largest size. We propose that zero dipole moment is a requirement for the metallic state even in tiny metal clusters. (This suggests that at low temperatures the Nb, V, and Ta clusters are in a nonmetallic state because of their large electric dipoles[80][110].) The measurement of dipole moments in alkali clusters is therefore very significant for the study of cluster metallicity and metal-to-insulator transitions.

Von Issendorff has proposed a definition of metallicity which compares the HOMO-LUMO gap at E_F with the Kubo gap for a given cluster size. If the HOMO-LUMO gap is larger than the Kubo gap the cluster is said to be non-metallic. The HOMO-LUMO gap can be measured by PES (Photoelectron Spectroscopy) [104]. Under this definition, some of the sodium clusters, such as the ones with closed electronic shells will possess HOMO-LUMO gaps larger than the Kubo gap and would be classified as insulators. We have observed no dipole moments for the magic number clusters.

4.2.1 Possible Dipole Moment of Na_6

For all of the Na clusters the magnitude of the broadening places a tight bound on the value of their dipole moments. The one exception is Na_6 where we observe a large loss of area which is possibly due to the presence of an isomer with a dipole moment (see Figure 41). Note that we haven't observed the beam broadening signature associated with a permanent dipole moment. Instead we observed a reduction in the intensity of the beam when the electric field is switched on. If the cluster Na_6 has two structural isomers one which possesses a dipole moment and one which doesn't, the intensity of the beam will be depleted when the electric field is turned on and the fraction of the beam with a dipole moment is deflected out of the beam. The residue is the isomer with zero dipole moment.

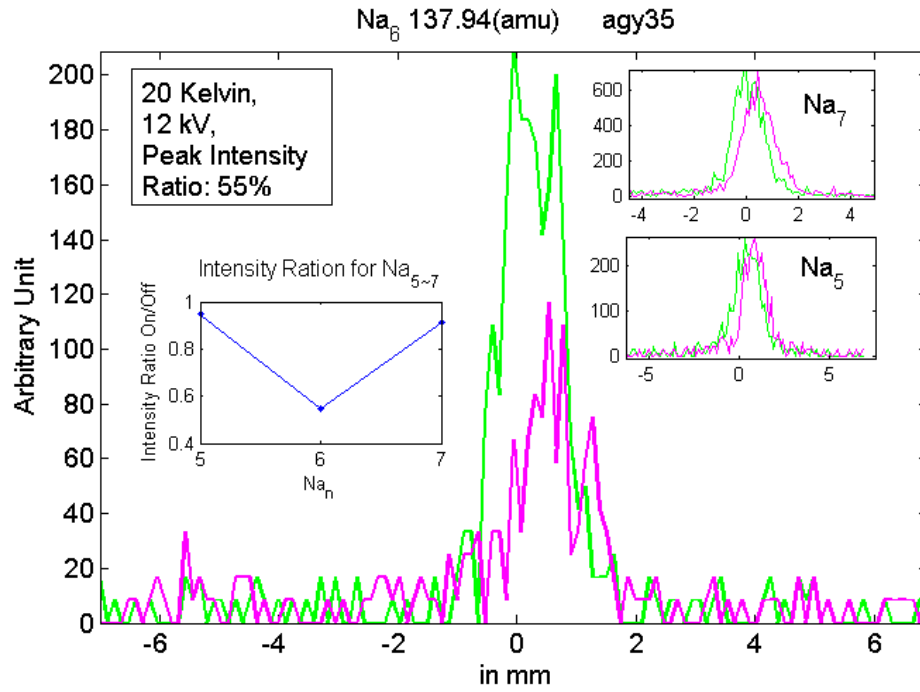


Figure 77: Na_6 cluster profile shows intensity reduction when the field is on (blue) and off (yellow) (this is raw data). If assuming two ground states in the beam and one of them possesses EDM that can be deflected out of the beam, then the thermal population ratio give us the energy difference between the two states $\Delta E = 1.2$ meV. Under the same run, the profiles of Na_5 and Na_7 are plotted in the insets of the figure for a comparison.

Theorists have predicted the existence of these two isomers and their total energies (atomization energies, or total binding energies)[90][40][27][85]. The theories seem to agree and converge on two structures but they disagree in their bond lengths and EDMs. We adopted the energies of these two isomers from [40]. The energies are 0.567 and 0.558 eV. The energy difference is 9 meV. The lower energy has the 3D structure (refer to Figure 78). The ratio of the thermal populations of these two states according to the Boltzmann distribution in the cluster source between the two states will be $e^{-(9 \text{ meV}/18 \text{ meV} (=20 \text{ K}))} = 0.0067 = 0.67\%$. This means at 20 K the dominant state should be the dipole one ($100\% - 0.67\% \simeq 99\%$). The fact that we still observe some residual intensity of the higher state indicates that the energy difference might be smaller than the theoretical prediction. If we convert the observe population ratio to the energy difference we will get ΔE should be 1.2 meV.

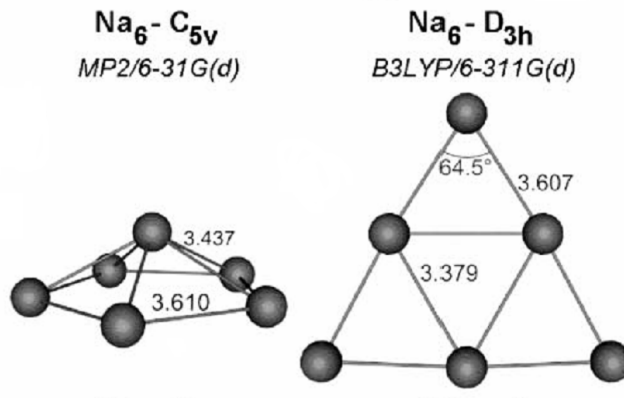


Figure 78: Ionic representation of the two energy isomers of Na₆ from theoretical prediction of [99].

This is probably the first time the two energy isomers of Na₆ have been experimentally observed, and this observation supports the conclusion of the theorists.

Our beam intensity is weak in the size range 3 – 7 atoms. This seems to be a common problem with a laser vaporization source, at least for alkali sodium clusters. Homer etc also had the similar situation[51]. Due to lack of intensity further conclusions on Na₃ and Na₆ will require more runs and possibly a different cluster source in order to increase the signal-to-noise ratio.

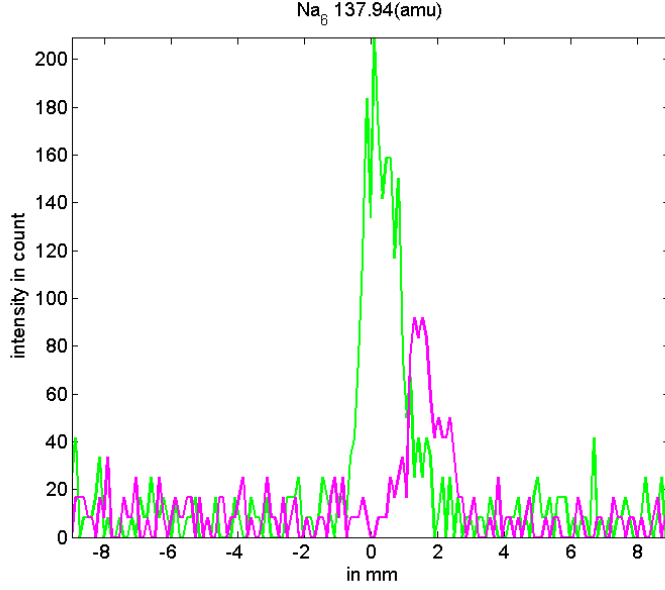


Figure 79: Another run (ahh series) showing intensity reduction on Na_6 . The intensity ratio gives the energy different very close to the previous.

4.2.2 A Short Look at Gold Cluster Au_9

It is worthwhile to consider other types of metal clusters before we discuss the possible origins of the EDM. One special case worthy of mention is the Au_9 cluster. The Au_9 beam profile shows a polarization distribution (logarithmic) characteristic of a dipole in the deflection experiment (see Figure 80). One can see that the beam is deflected in both directions (to the left and to the right, both high-field and low-field seeking). From the polarization distribution section we can infer that the extent of the tail can be a rough estimate of the magnitude of the dipole moment (in this case about 0.4 Debye, where the x-axis has been converted to the dipole unit). From a more rigorous logarithmic fitting procedure, we conclude that the dipole moment is 0.42 ± 0.02 Debye. (We convolved the off peak with a logarithmic distribution to match the on profile, under a least square method.) The measured polarizability of Au_9 from the profiles average deflection is $7.96 \text{ \AA}^3/\text{atom}$. If we subtract from the polarizability dipole's Langevin-Debye contribution $\frac{2p^2}{9kT} = 6.3 \text{ \AA}^3$ (With the approximation that the cluster has a spherical shape. Even if this is not true it will still be close. See the polarization distribution section for a full discussion). We find

the remaining polarizability is 65 \AA^3 .

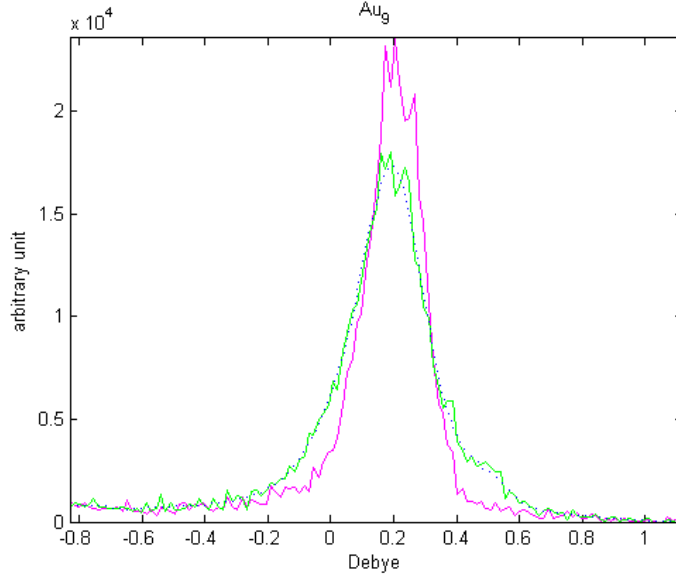


Figure 80: Gold cluster 9 show characteristic beam broadening of an intrinsic dipole moment. Estimated dipole is about 0.42 ± 0.02 Debye. Beam temperature is 33 K.

Interesting enough Au_9 had been predicted to have two energy isomers as well (as in Na_6 case). In the gold case both conformations adopt a planar structure (Figure 81). The theoretical calculations for the energy difference is 80 meV, which is close to 500 Kelvin in temperature. So we observe only the ground state 9a which does indeed have dipole moment of 0.32 Debye according to the theoretical prediction. There is no intensity reduction because at the experimental temperature (33 K) only the ground state 9a will be populated.

The origin of the electric dipole moment for the homonuclear metal clusters is still a topic of active debate. Here we introduce an interesting proposal from Professor Robert Whetten, based on valence bond theory, made by McAdon and Goddard around 1985, for a flattened or planar structure of cluster [76][77][78]. The theory is based on a triangle system consisting of three atoms. The bonded valence electrons will have a center of mass sitting in the middle of the triangle.

For other types of homonuclear metal clusters, like transition or rare earth, we do observe a beam broadening from case to case at low temperature under electric field [Bowlan etc., to be published]. To mention a few: Y_N , Ho_N , Co_N , Rh_N , Bi_N , Pr_N , Tb_N , Tm_N , ...

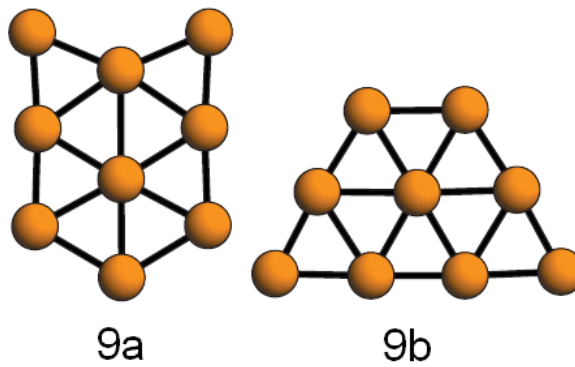


Figure 81: Theoretically predicted ionic structure of the two low-lying energy isomers of Au_9 clusters. The energy difference is 80 meV (~ 500 Kelvin). The corresponding dipole moments of 9a and 9b are 0.32 Debye and 1.01 Debye respectively. (Private communication with professor Hannu Haikkinen.)

In conclusion we have shown measured dipole moments of Na clusters and found that they are in some cases an order of magnitude smaller than predicted. We believe that zero dipole moment is a fundamental requirement for the metallic state.

APPENDIX A

ANCILLARY

A.1 *Some facts about bulk sodium*

MP: 370.87 K

BP: 1156 K

Debye Temperature: 158 K

Fermi energy: 3.23 eV

Wigner-Sietz radius: $r_{ws} = 2.12 \text{ \AA}[100]$,

Fermi wavelength of elctrons in simple sodium metals $\lambda_F = (32\pi^2/9)^{1/3}r_{ws} = 3.28r_{ws}$

For sodium atom the s electron provides about 98% of the total polarizability.

Bulk Sodium is BCC, large clusters 1000 - 10000 suspect to have FCC or icosahedral[75].

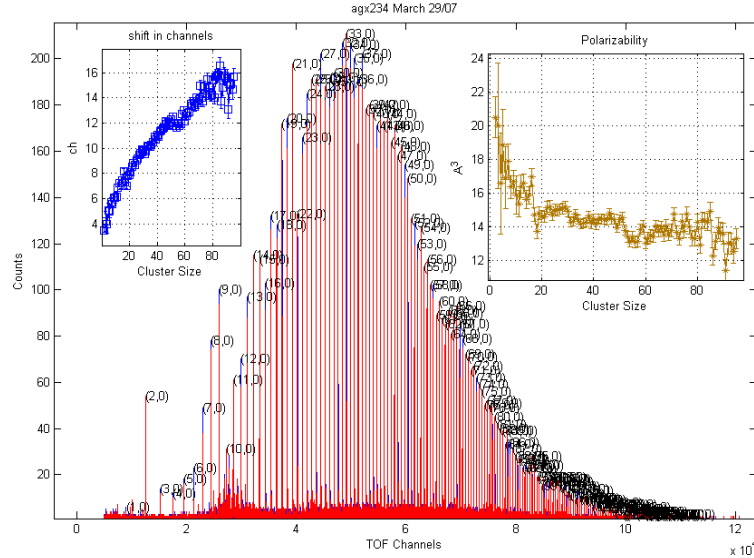


Figure 82: Sodium typical mass spectrum, with two inset showing left: the distance between on and off peaks in channels, and right: the corresponding polarizability.

Background Gas Scattering: Long Range London Dispersion Force. Slater-Kirkwood

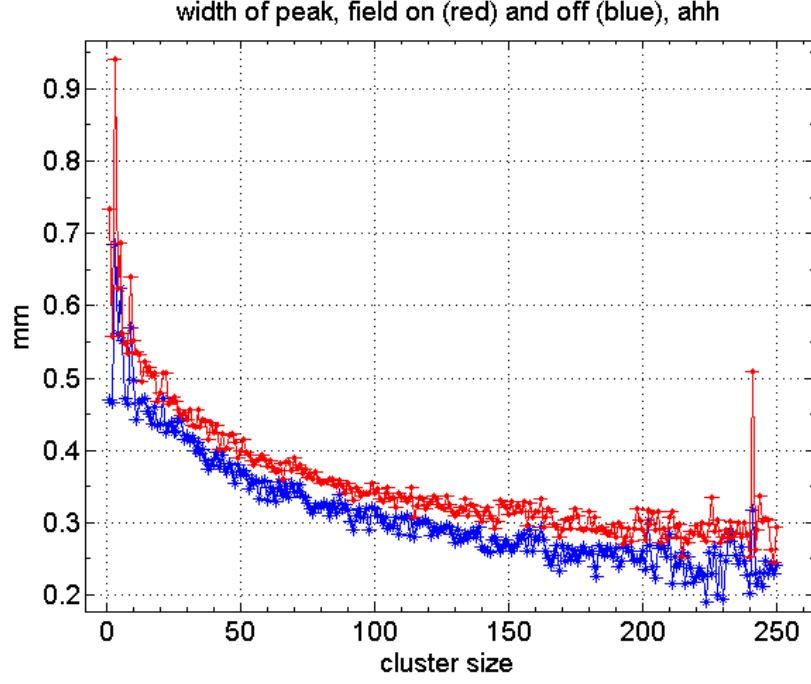


Figure 83: The width of the field off and field on peak in mm position units. One can see the increase in width as the size gets smaller.

electronic contribution to attraction interaction:

$$C_6 = \frac{\alpha_A + \alpha_B}{\sqrt{\frac{\alpha_A}{N_A}} + \sqrt{\frac{\alpha_B}{N_B}}} \quad (113)$$

$$\sigma \text{ (total cross section)} = \left(\frac{C_6}{v} \right)^{\frac{2}{5}} \quad (114)$$

where α_A and α_B are the polarizability of the two scattering particles, N_A and N_B are the number of valence electrons of the two particle individually, and v is the relative velocity between the two scatterers. Please see [63] for a thorough discussion.

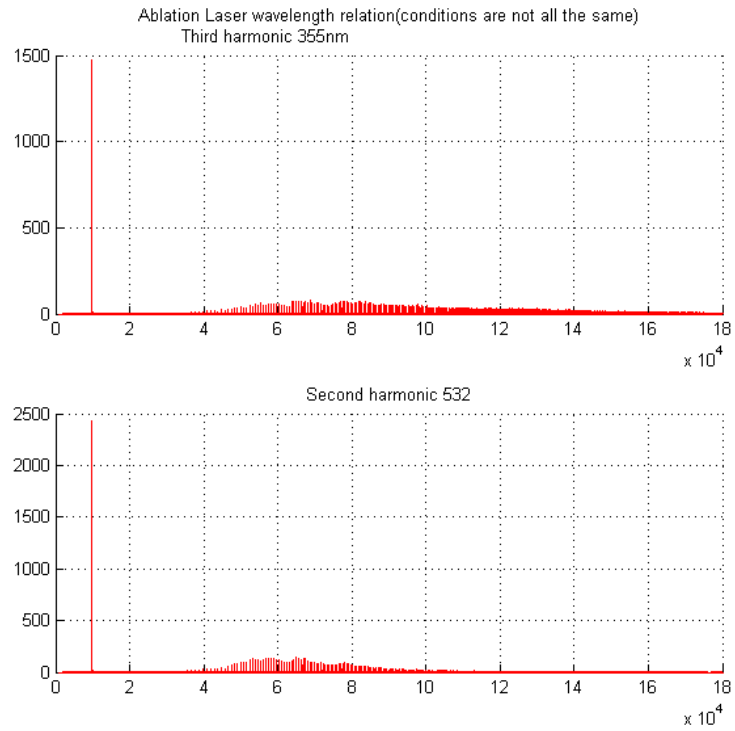


Figure 84: Mass abundances with different ablation laser wavelengths. Higher photon energy leads to more atoms evaporation and thus higher density and this gives rise to larger cluster size distribution. Other conditions are kept as close as possible.

A.2 Sodium clusters spectrum OPO different wavelenth picture

A.3 Langevin-debye response: thermal averaging

If we have a bunch of dipoles each with moment μ , the probability that dipole orient in θ and $\theta + d\theta$ is

$$\frac{e^{-\frac{E(\theta)}{kT}} \sin \theta d\theta}{\int_0^\pi e^{-\frac{E(\theta)}{kT}} \sin \theta d\theta} \quad (115)$$

$$E(\theta) = -\mu E \cos \theta \quad (116)$$

So average dipole moment along a field direction z ,

$$\langle \mu_z \rangle = \int \mu \cos \theta \frac{e^{-\frac{E(\theta)}{kT}} \sin \theta d\theta}{\int_0^\pi e^{-\frac{E(\theta)}{kT}} \sin \theta d\theta} \quad (117)$$

$$= \int \frac{\mu e^{-x \cos \theta} \cos \theta \sin \theta d\theta}{\int_0^\pi e^{-x \cos \theta} \sin \theta d\theta} \quad (118)$$

$$= \frac{\mu \int_{-1}^1 y e^{xy} dy}{\int_{-1}^1 e^{xy} dy} \quad (119)$$

$$= \mu L(x) \quad (120)$$

where

$$L(x) = \frac{e^x + e^{-x}}{e^x - e^{-x}} - \frac{1}{x} \quad (121)$$

and

$$x = \frac{\mu E}{kT} \quad (122)$$

$L(x)$ is the Langevin function. So when x is small $\langle \mu_z \rangle$ will become $\frac{1}{3} \frac{\mu^2 E}{kT}$.

A.4 Conference Proceedings

1. 2009 APS March Meeting

Monday–Friday, March 16–20, 2009; Pittsburgh, Pennsylvania

Session Z37: Mesoscopic Systems, Clusters, and Nanoscale Systems II

11:15 AM–1:39 PM, Friday, March 20, 2009 - 409

Sponsoring Unit: DCP

Chair: Shiv Khanna, Virginia Commonwealth University

Abstract ID: BAPS.2009.MAR.Z37.8

Abstract: Z37.00008 : Interpreting the magnetic and electric deflections of free metal clusters in molecular beams

12:39 PM–12:51 PM

Preview Abstract

Authors: Anthony Liang, John Bowlan, Walter de Heer

A short review of the analysis of magnetic and electric deflection data will be presented. Electric and magnetic beam deflection of several metal clusters, including Au_N , Al_N , Nb_NO , Na_N , Ho_N , Co_N , Rh_N at various temperatures (20K-300K) and field strengths will be presented. The relation between the broadening of the deflected beam and the polarization distribution of the ensemble assuming a classical polar spherical rigid rotor model is demonstrated. Complicating factors including asymmetry effects and residual temperature effects will be discussed.

Citation reference: <http://meetings.aps.org/link/BAPS.2009.MAR.Z37.8>

2. 2008 APS March Meeting

Session J21: Focus Session: Clusters, Cluster Assemblies, Nanoscale Materials IV

11:15 AM–2:03 PM, Tuesday, March 11, 2008

Morial Convention Center - 213

Sponsoring Unit: DCP

Chair: Meichun Qian, Virginia Commonwealth University

Abstract ID: BAPS.2008.MAR.J21.2

Abstract: J21.00002 : Low Temperature Static Dipole Polarizability of Free Sodium Clusters with from 2 to 250 atoms 11:51 AM–12:03 PM

Preview Abstract

Authors: Anthony Liang, John Bowlan, Xiao-Shan Xu, Shuang-Ye Yin, Walt A. de Heer

The electric dipole polarizabilities of all sodium clusters Na_N were measured from the atom up to $n=250$ using the molecular beam deflection method. Clusters were

formed in cryogenic laser vaporization source operating at a temperature of 20 K. This complete sequence of high-resolution polarizabilities measurements greatly enhances previous measurements. Electronic shell effects are observed as well as several features that are not readily understood in the shell model. The asymptotic limit of the measurements appears not to converge to the bulk sodium polarizability value. The data are compared with theoretical predictions.

Citation reference: <http://meetings.aps.org/link/BAPS.2008.MAR.J21.2>

3. 2007 APS March Meeting

Session L18: Metal Clusters, 2:30 PM–5:30 PM; Tuesday, March 6, 2007, Colorado Convention Center - 103

Sponsoring Unit: DCP

Chair: A. Welford Castleman, Pennsylvania State University

Abstract ID: BAPS.2007.MAR.L18.14

Abstract: L18.00014 : Electron pairing in pure Niobium and Niobium alloy clusters, 5:06 PM–5:18 PM

Preview Abstract

Authors: Anthony Liang, Xiaoshan Xu, Shuangye Yin, John Bowlan, Walt de Heer
Electrons in pure niobium and in niobium alloy clusters are ferroelectric at low temperatures. The ferroelectric effect is enhanced for niobium clusters doped with non-magnetic metals and reduced when doped with magnetic atoms. The effect is enhanced (reduced) for clusters with an even (odd) total number of valence electrons. For specific alloy clusters the ferroelectric state persists up to room temperature. Ferroelectricity in these clusters and superconductivity in the corresponding bulk appear to be related, with similar transition temperatures and similar responses to specific impurities. The spontaneous polarization of a ground state involving a Cooper pair explains the observations.

Citation reference: <http://meetings.aps.org/link/BAPS.2007.MAR.L18.14>

APPENDIX B

PHOTOABSORPTION OF SODIUM CLUSTERS

People now realize the collective oscillations of the electrons dominate the light response properties of finite quantum systems such as nanoparticles, fullerenes[96] and nuclei. See [14] for a review. It is found that same situation happens to the metal clusters. Instead of a transition between allowed quantum states, dipolar vibrations of delocalized valence electrons in simple alkali metal clusters are observed. These had been extensively investigated both experimentally and theoretically[62][97][107] since their first observation 20 years ago.

Because the photoabsorption spectrum contains the geometry information of the clusters, it will be useful to estimate the asphericity of the clusters and calculate the corresponding contribution to the polarizabilities in our measurement. Photoabsorption cross-section for neutral sodium clusters have been measured by [97]

First we look at the generic photoabsorption cross section of a dielectric sphere reads (Mie theory)

$$\sigma(\hbar\omega) = \frac{4\pi\omega}{c} R^3 \text{Im}\left(\frac{\epsilon(\omega) - 1}{\epsilon(\omega) + 2}\right) \quad (123)$$

The photoabsorption cross section of a cluster can be modeled as

$$\sigma(E = \hbar\omega) = \frac{\hbar e^2}{m_e c \epsilon_0} \sum_{i=1}^3 \frac{f_i E_i^2 \Gamma_i}{(E^2 - E_i^2)^2 + (E \Gamma_i)^2} \quad (124)$$

f_i , E_i , and Γ_i are oscillator strength, peak position, and the width of the single resonance. If the cluster can be approximated by triaxial ellipsoid, one can generally relate E_i to the polarizability α_i via $E_i = \hbar N e^2 / m_e \alpha_i$. One can also define moment M_k

$$M_0 = \int_0^\infty \sigma(E) dE \text{ for } k=0 \quad (125)$$

$$M_k = \frac{1}{M_0} \int_0^\infty E^k \sigma(E) dE \text{ for } k>0 \quad (126)$$

. For $k = 0$, one obtains the Thomas-Reiche-Kuhn sum rule for the oscillator strength f ,

which states that the zeroth moment is proportional to the number of electrons N .

$$f = \frac{2m_e c \epsilon_0}{\pi \hbar e^2} M_0 = \frac{0.911}{\text{\AA}^2(\text{eV})} \int \sigma dE = N \quad (127)$$

The average static polarizability is proportional to the minus second moment

$$\bar{\alpha} = \frac{e^2 \hbar^2}{m} M_{-2} \quad (128)$$

[92]. Often more than half of the oscillator strength are concentrated in a few peaks[97].

Photoabsorption cross-section for sodium clusters cations, Na_n^+ , $4 \leq n \leq 64$, have been measured at a temperature of about 105K and polarizabilities are obtained using the above method.

Absorption cross section of Cs_8 , K_9^+ , Na_8 , Na_9^+ are presented and the resonance energies are given in the table.

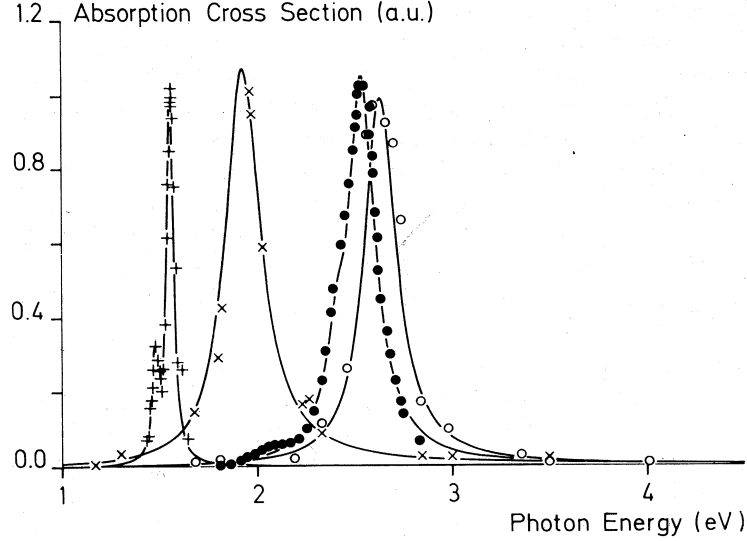


Figure 85: Giant resonances for 8-electron clusters (+) Cs_8 , (\times) K_9^+ , (\bullet) Na_8 , (\circ) Na_9^+ . The single peak put in evidence spherical symmetry. Source figure from [44]

Volume plasma in bulk metals cannot be excited optically because light waves are propagated transversely, whereas the compressional plasma waves in an infinite medium are propagated longitudinally. Therefore volume plasma have been primarily probed by electron energy-loss spectroscopy. However the situation becomes very different in nanoparticles, even those of the same metal. When a boundary surface is present, the wave vector no

longer remains a good quantum number, so in finite metal nanoclusters the compressional volume plasmons are expected to become capable of coupling to light[107]. The following figure from [107] presents a suspected volume plasma($\sim 4\text{eV}$) exist in Sodium clusters Na_{20} , Na_{92} and several among 21 - 40.

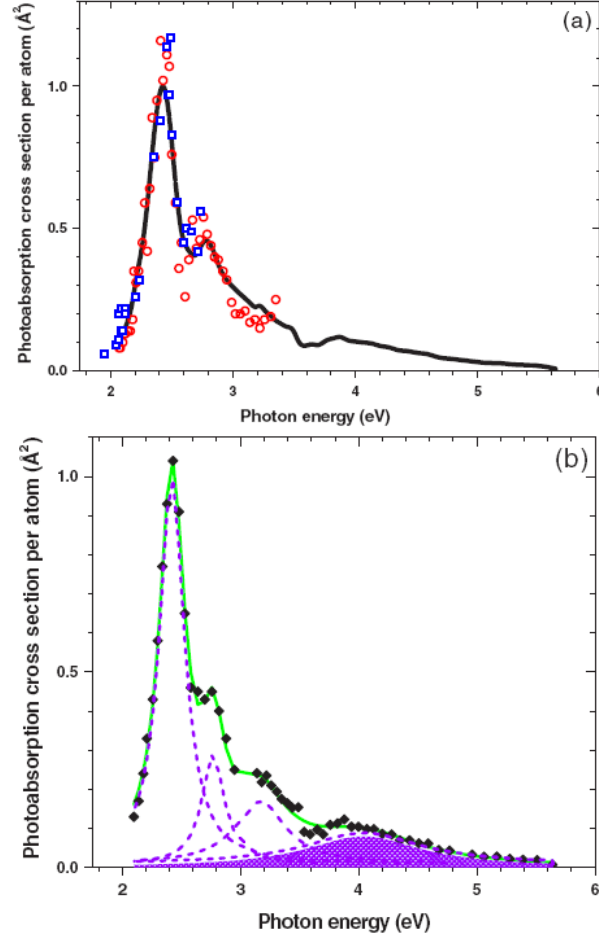


Figure 86: Photoabsorption cross section of Na_{20} , Na_{92} clusters showing possible volume resonance (shaded region lower graph). Source is from [107].

REFERENCES

- [1] ALAMEDDIN, G., HUNTER, J., CAMERON, D., and KAPPES, M. M., “Electronic and geometric structure in silver clusters,” *Chemical Physics Letters*, vol. 192, no. 1, pp. 122–128, 1992.
- [2] ALONSO, J. A., *Structure and properties of atomic nanoclusters*. London : Imperial College Press: Singapore ; Hackensack, NJ, 2005. Distributed by World Scientific Pub. ill. ; 24 cm. Introduction to clusters. – Experimental production of clusters. – Van der Waals clusters. – Electronic and atomic shells in metal clusters. – Electronic and optical properties of simple metal clusters. – Melting and fragmentation of metal clusters. – Bimetallic clusters. – Clusters of the transition metals. – Magnetism. – Clusters of ionic materials. – Carbon clusters. – Assembling of new materials from clusters. Includes bibliographical references and index. Julio A. Alonso. Book.
- [3] ANTOINE, R., EL RAHIM, M. A., BROYER, M., RAYANE, D., and DUGOURD, P., “Asymmetric top rotors in electric fields. ii. influence of internal torsions in molecular beam deflection experiments,” *Journal of Physical Chemistry A*, vol. 110, no. 33, pp. 10006–10011, 2006.
- [4] ANTOINE, R., RAYANE, D., ALLOUCHE, A. R., FRECON, M. A., BENICHO, E., DALBY, F. W., DUGOURD, P., BROYER, M., and GUET, C., “Static dipole polarizability of small mixed sodium-lithium clusters,” *Journal of Chemical Physics*, vol. 110, no. 12, pp. 5568–5577, 1999.
- [5] APELL, S. P., CABRERA-TRUJILLO, R., ODDERSHEDE, J., TRICKEY, S. B., and SABIN, J. R., “Effect of shape on molecular directional compton profiles,” *Journal of Molecular Structure-Theochem*, vol. 527, pp. 157–163, 2000.
- [6] APELL, S. P., SABIN, J. R., and ODDERSHEDE, J., “Molecular shape and the bragg rule,” *Physical Review A*, vol. 66, no. 3, p. 4, 2002.
- [7] APELL, S. P., TRICKEY, S. B., and SABIN, J. R., “Geometrical basis for molecular stopping anisotropy,” *Physical Review A*, vol. 58, no. 6, pp. 4616–4621, 1998.
- [8] ATKINS, P. W., *Physical chemistry*. New York :: W.H. Freeman, 7th ed. ed., 2002.
- [9] BALLENTINE, G. E., BERTSCH, G. F., ONISHI, N., and YABANA, K., “Moment distributions of clusters and molecules in the adiabatic rotor model,” *Computer Physics Communications*, vol. 178, no. 1, pp. 48–51, 2008.
- [10] BARTELS, C., HOCK, C., HUWER, J., KUHNEN, R., SCHWOBEL, J., and VON ISSENDORFF, B., “Probing the angular momentum character of the valence orbitals of free sodium nanoclusters,” *Science*, vol. 323, no. 5919, pp. 1323–1327, 2009.
- [11] BECK, D. E., “Self-consistent calculation of the polarizability of small jellium spheres,” *Physical Review B*, vol. 30, no. 12, pp. 6935–6942, 1984.

- [12] BERTSCH, G., ONISHI, N., and YABANA, K., "Magnetization of ferromagnetic clusters," *Zeitschrift Fur Physik D-Atoms Molecules and Clusters*, vol. 34, no. 3, pp. 213–217, 1995.
- [13] BERTSCH, G. F. and YABANA, K., "Cold cluster ferromagnetism," *Physical Review A*, vol. 49, no. 3, pp. 1930–1932, 1994.
- [14] BERTSCH, G. F., *Oscillations in finite quantum systems*. Cambridge monographs on mathematical physics, Cambridge [England] ;: Cambridge University Press, 1994.
- [15] BEVINGTON, P. R., *Data reduction and error analysis for the physical sciences*. New York :: McGraw-Hill, 2nd ed. ed., 1992. System requirements for diskette: IBM PC compatible; 5.25" diskette drive.
- [16] BILLAS, I. M. L., CHATELAIN, A., and DEHEER, W. A., "Magnetism from the atom to the bulk in iron, cobalt, and nickel clusters," *Science*, vol. 265, no. 5179, pp. 1682–1684, 1994.
- [17] BJORNHOLM, S. and BORGGREEN, J., "Electronic shell structure in clusters as reflected in mass abundance spectra," *Philosophical Magazine B-Physics of Condensed Matter Statistical Mechanics Electronic Optical and Magnetic Properties*, vol. 79, no. 9, pp. 1321–1342, 1999.
- [18] BJORNHOLM, S., BORGGREEN, J., ECHT, O., HANSEN, K., PEDERSEN, J., and RASMUSSEN, H. D., "Mean-field quantization of several hundred electrons in sodium metal-clusters," *Physical Review Letters*, vol. 65, no. 13, pp. 1627–1630, 1990.
- [19] BLUNDELL, S. A., GUET, C., and ZOPE, R. R., "Temperature dependence of the polarizability of sodium clusters," *Physical Review Letters*, vol. 84, no. 21, pp. 4826–4829, 2000.
- [20] BONIN, K. D., *Electric-dipole polarizabilities of atoms, molecules and clusters*. Singapore :: World Scientific, 1997.
- [21] BORGGREEN, J., HANSEN, K., CHANDEZON, F., DOSSING, T., ELHAJAL, M., and ECHT, O., "Absolute separation energies for na clusters," *Physical Review A*, vol. 62, no. 1, pp. art. no.–013202, 2000.
- [22] BRACK, M., "The physics of simple metal-clusters - self-consistent jellium model and semiclassical approaches," *Reviews of Modern Physics*, vol. 65, no. 3, pp. 677–732, 1993.
- [23] BRECHIGNAC, C., CAHUZAC, P., LEYGNIER, J., and WEINER, J., "Dynamics of uni-molecular dissociation of sodium cluster ions," *Journal of Chemical Physics*, vol. 90, no. 3, pp. 1492–1498, 1989.
- [24] BROYER, M., ANTOINE, R., BENICHO, E., COMPAGNON, I., DUGOURD, P., and RAYANE, D., "Structure of nano-objects through polarizability and dipole measurements," *Comptes Rendus Physique*, vol. 3, no. 3, pp. 301–317, 2002.
- [25] BUDKER, D., *Atomic physics : an exploration through problems and solutions*. Oxford :: Oxford University Press, 2004.

- [26] BULTHUIS, J., BECKER, J. A., MORO, R., and KRESIN, V. V., "Orientation of dipole molecules and clusters upon adiabatic entry into an external field," *Journal of Chemical Physics*, vol. 129, no. 2, p. 7, 2008.
- [27] CHANDRAKUMAR, K. R. S., GHANTY, T. K., and GHOSH, S. K., "Static dipole polarizability and binding energy of sodium clusters Na_n ($n=1-10$): A critical assessment of all-electron based post hartree-fock and density functional methods," *Journal of Chemical Physics*, vol. 120, no. 14, pp. 6487–6494, 2004.
- [28] CHATELAIN, A., "Stern-gerlach deflection of ferromagnetic cluster beams," *Philosophical Magazine B-Physics of Condensed Matter Statistical Mechanics Electronic Optical and Magnetic Properties*, vol. 79, no. 9, pp. 1367–1378, 1999.
- [29] CLEMENGER, K. L., *Spheroidal shell structure and static electric polarizabilities of alkali metal clusters*. Thesis, University of California, 1985. ill. ; 28 cm. Includes bibliographical references (pages 102-105). by Keith Levern Clemenger. Thesis/dissertation (deg); Manuscript (mss).
- [30] COX, A. J., LOUDERBACK, J. G., APSEL, S. E., and BLOOMFIELD, L. A., "Magnetism in 4d-transition metal-clusters," *Physical Review B*, vol. 49, no. 17, pp. 12295–12298, 1994.
- [31] DE HEER, W. A. and KRESIN, V. V., "Electric and magnetic dipole moments of free nanoclusters," 2009. <http://www.citebase.org/abstract?id=oai:arXiv.org:0901.4810>.
- [32] DEHEER, W. A., "The physics of simple metal-clusters - experimental aspects and simple-models," *Reviews of Modern Physics*, vol. 65, no. 3, pp. 611–676, 1993.
- [33] DUGOURD, P., ANTOINE, R., ABD EL RAHIM, M., RAYANE, D., BROYER, M., and CALVO, F., "Molecular dynamics simulations of molecular beam deflection experiments," *Chemical Physics Letters*, vol. 423, no. 1-3, pp. 13–16, 2006.
- [34] DUGOURD, P., COMPAGNON, I., LEPINE, F., ANTOINE, R., RAYANE, D., and BROYER, M., "Beam deviation of large polar molecules in static electric fields: theory and experiment," *Chemical Physics Letters*, vol. 336, no. 5-6, pp. 511–517, 2001.
- [35] EKARDT, W. and PENZAR, Z., "On the static polarizability of small metal particles," *Solid State Communications*, vol. 57, no. 8, pp. 661–663, 1986.
- [36] EKARDT, W. and PENZAR, Z., "Self-consistent sommerfeld droplet as a simple-model for an accurate prediction of the electronic-properties of small metal particles," *Physical Review B*, vol. 38, no. 6, pp. 4273–4276, 1988.
- [37] EKARDT, W., *Metal clusters*. Wiley series in theoretical chemistry, Chichester, England ;: Wiley, 1999.
- [38] EL RAHIM, M. A., ANTOINE, R., BROYER, M., RAYANE, D., and DUGOURD, P., "Asymmetric top rotors in electric fields: Influence of chaos and collisions in molecular beam deflection experiments," *Journal of Physical Chemistry A*, vol. 109, no. 38, pp. 8507–8514, 2005.
- [39] EVETTS, J., *Concise encyclopedia of magnetic & superconducting materials*. Advances in materials science and engineering, Oxford ;: Pergamon Press, 1st ed. ed., 1992.

- [40] FOIS, E. S., PENMAN, J. I., and MADDEN, P. A., "Self-interaction corrected density functionals and the structure of metal-clusters," *Journal of Chemical Physics*, vol. 98, no. 8, pp. 6352–6360, 1993.
- [41] GERLACH, W. and STERN, O., "The experimental evidence of direction quantization in the magnetic field," *Zeitschrift Fur Physik*, vol. 9, pp. 349–352, 1922.
- [42] GOLDSTEIN, H., *Classical mechanics*. Reading, Mass. :: Addison-Wesley Pub. Co., 2d ed. ed., 1980. Includes index.
- [43] HABERLAND, H., HIPPLER, T., DONGES, J., KOSTKO, O., SCHMIDT, M., and VON ISSENDORFF, B., "Melting of sodium clusters: Where do the magic numbers come from?," *Physical Review Letters*, vol. 94, no. 3, 2005.
- [44] HABERLAND, H., *Clusters of atoms and molecules : theory, experiment, and clusters of atoms*. Springer series in chemical physics ;, Berlin ;: Springer-Verlag, 1994.
- [45] HAGENA, O. F., "Nucleation and growth of clusters in expanding nozzle flows," *Surface Science*, vol. 106, no. 1-3, pp. 101–116, 1981.
- [46] HAKKINEN, H., MOSELER, M., KOSTKO, O., MORGNER, N., HOFFMANN, M. A., and VON ISSENDORFF, B., "Symmetry and electronic structure of noble-metal nanoparticles and the role of relativity," *Physical Review Letters*, vol. 93, no. 9, p. 4, 2004.
- [47] HAKKINEN, H., MOSELER, M., and LANDMAN, U., "Bonding in cu, ag, and au clusters: Relativistic effects, trends, and surprises," *Physical Review Letters*, vol. 89, no. 3, 2002.
- [48] HALPERIN, W. P., "Quantum size effects in metal particles," *Reviews of Modern Physics*, vol. 58, no. 3, pp. 533–606, 1986.
- [49] HAMAMOTO, N., ONISHI, N., and BERTSCH, G., "Magnetic properties of an ensemble of rotating ferromagnetic clusters," *Physical Review B*, vol. 61, no. 2, pp. 1336–1350, 2000.
- [50] HARRIS, I. A., KIDWELL, R. S., and NORTHBY, J. A., "Structure of charged argon clusters formed in a free jet expansion," *Physical Review Letters*, vol. 53, no. 25, pp. 2390–2393, 1984.
- [51] HONEA, E. C., HOMER, M. L., PERSSON, J. L., and WHETTEN, R. L., "Generation and photoionization of cold nan clusters - n to 200," *Chemical Physics Letters*, vol. 171, no. 3, pp. 147–154, 1990.
- [52] JACKSON, J. D., *Classical electrodynamics*. New York :: Wiley, 3rd ed. ed., 1999.
- [53] JOHNSTON, R. L., *Atomic and molecular clusters*. Master's series in physics and astronomy, London ;: Taylor & Francis, 2002.
- [54] KATAKUSE, I., ICHIHARA, T., FUJITA, Y., MATSUO, T., SAKURAI, T., and MATSUDA, H., "Mass distributions of copper, silver and gold clusters and electronic shell structure," *International Journal of Mass Spectrometry and Ion Processes*, vol. 67, no. 2, pp. 229–236, 1985.

- [55] KHANNA, S. N. and JENA, P., "Assembling crystals from clusters," *Physical Review Letters*, vol. 69, no. 11, pp. 1664–1667, 1992.
- [56] KITTEL, C., *Introduction to solid state physics*. Hoboken, NJ :: Wiley, 8th ed. ed., 2005. "Chapter 18, Nanostructures, was written by Professor Paul McEuen ...".
- [57] KNICKELBEIN, M. B., "Electric dipole polarizabilities of copper clusters," *Journal of Chemical Physics*, vol. 120, no. 22, pp. 10450–10454, 2004.
- [58] KNIGHT, W. D., CLEMENGER, K., DEHEER, W. A., and SAUNDERS, W. A., "Polarizability of alkali clusters," *Physical Review B*, vol. 31, no. 4, pp. 2539–2540, 1985.
- [59] KNIGHT, W. D., CLEMENGER, K., DEHEER, W. A., SAUNDERS, W. A., CHOU, M. Y., and COHEN, M. L., "Electronic shell structure and abundances of sodium clusters," *Physical Review Letters*, vol. 52, no. 24, pp. 2141–2143, 1984.
- [60] KNIGHT, W. D., DEHEER, W. A., SAUNDERS, W. A., CLEMENGER, K., CHOU, M. Y., and COHEN, M. L., "Alkali-metal clusters and the jellium model," *Chemical Physics Letters*, vol. 134, no. 1, pp. 1–5, 1987.
- [61] KOSTKO, O., HUBER, B., MOSELER, M., and VON ISSENDORFF, B., "Structure determination of medium-sized sodium clusters," *Physical Review Letters*, vol. 98, no. 4, 2007.
- [62] KRESIN, V. V., "Collective resonances and response properties of electrons in metal-clusters," *Physics Reports-Review Section of Physics Letters*, vol. 220, no. 1, pp. 1–52, 1992.
- [63] KRESIN, V. V., KASPEROVICH, V., TIKHONOV, G., and WONG, K., "Strong long-range forces between c-60 and na atoms and microclusters," *Physical Review A*, vol. 57, no. 1, pp. 383–387, 1998.
- [64] KUBO, R., KAWABATA, A., and KOBAYASHI, S., "Electronic-properties of small particles," *Annual Review of Materials Science*, vol. 14, pp. 49–66, 1984.
- [65] KUMMEL, S., AKOLA, J., and MANNINEN, M., "Thermal expansion in small metal clusters and its impact on the electric polarizability," *Physical Review Letters*, vol. 84, no. 17, pp. 3827–3830, 2000.
- [66] KURKINA, L. I., "Static polarizability of excited and charged alkali metal clusters," *Physics of the Solid State*, vol. 43, no. 4, pp. 792–798, 2001.
- [67] LANDAU, L. D., *Electrodynamics of continuous media*. Course of theoretical physics ;, Oxford :: Pergamon Press, 2nd ed., rev. and enl. / ed., 1984.
- [68] LANDAU, L. D., LIFSHITZ, E. M., and ALLEN, L. K., "Electrodynamics of continuous media," *American Journal of Physics*, vol. 29, no. 9, pp. 647–648, 1961.
- [69] LANG, N. D. and KOHN, W., "Theory of metal surfaces - charge density and surface energy," *Physical Review B*, vol. 1, no. 12, pp. 4555–&, 1970.
- [70] LANG, N. D. and KOHN, W., "Theory of metal surfaces - work function," *Physical Review B*, vol. 3, no. 4, pp. 1215–&, 1971.

- [71] LIU, X., BAUER, M., BERTAGNOLLI, H., RODUNER, E., VAN SLAGEREN, J., and PHILLIPP, F., "Structure and magnetization of small monodisperse platinum clusters," *Physical Review Letters*, vol. 97, no. 25, p. 4, 2006.
- [72] MACKAY, A. L., "A dense non-crystallographic packing of equal spheres," *Acta Crystallographica*, vol. 15, no. SEP, pp. 916–918, 1962.
- [73] MANNINEN, M., NIEMINEN, R. M., and PUSKA, M. J., "Electronic polarizability of small sodium clusters," *Physical Review B*, vol. 33, no. 6, pp. 4289–4290, 1986.
- [74] MARKOV, I. V., *Crystal growth for beginners : fundamentals of nucleation, crystal growth, and epitaxy*. Singapore ;: World Scientific, 1995.
- [75] MARTIN, T. P., NAHER, U., SCHABER, H., and ZIMMERMANN, U., "Evidence for a size-dependent melting of sodium clusters," *Journal of Chemical Physics*, vol. 100, no. 3, pp. 2322–2324, 1994.
- [76] MCADON, M. H. and GODDARD, W. A., "New concepts of metallic bonding based on valence-bond ideas," *Physical Review Letters*, vol. 55, no. 23, pp. 2563–2566, 1985.
- [77] MCADON, M. H. and GODDARD, W. A., "Generalized valence bond studies of metallic bonding - naked clusters and applications to bulk metals," *Journal of Physical Chemistry*, vol. 91, no. 10, pp. 2607–2626, 1987.
- [78] MCADON, M. H. and GODDARD, W. A., "Charge-density waves, spin-density waves, and peierls distortions in one-dimensional metals .1. hartree-fock studies of cu, ag, au, li, and na," *Journal of Chemical Physics*, vol. 88, no. 1, pp. 277–302, 1988.
- [79] MORO, R., BULTHUIS, J., HEINRICH, J., and KRESIN, V. V., "Electrostatic deflection of the water molecule: A fundamental asymmetric rotor," *Physical Review A*, vol. 75, no. 1, p. 6, 2007.
- [80] MORO, R., XU, X. S., YIN, S. Y., and DE HEER, W. A., "Ferroelectricity in free niobium clusters," *Science*, vol. 300, no. 5623, pp. 1265–1269, 2003.
- [81] OSBORN, J. A., "Demagnetizing factors of the general ellipsoid," *Physical Review*, vol. 67, no. 11-1, pp. 351–357, 1945.
- [82] PAULY, H., *Atom, molecule, and cluster beams*. Springer series on atomic, optical, and plasma physics ;, Berlin ;: Springer, 2000.
- [83] PEDERSEN, J., BJORNHOLM, S., BORGGREEN, J., HANSEN, K., MARTIN, T. P., and RASMUSSEN, H. D., "Observation of quantum supershells in clusters of sodium atoms," *Nature*, vol. 353, no. 6346, pp. 733–735, 1991.
- [84] PELLARIN, M., BAGUENARD, B., VIALLE, J. L., LERME, J., BROYER, M., MILLER, J., and PEREZ, A., "Evidence for icosahedral atomic shell structure in nickel and cobalt clusters - comparison with iron clusters," *Chemical Physics Letters*, vol. 217, no. 4, pp. 349–356, 1994.
- [85] POTEAU, R. and SPIEGELMANN, F., "Structural-properties of sodium microclusters (n=4-34) using a monte-carlo growth method," *Journal of Chemical Physics*, vol. 98, no. 8, pp. 6540–6557, 1993.

- [86] PUSKA, M. J., NIEMINEN, R. M., and MANNINEN, M., "Electronic polarizability of small metal spheres," *Physical Review B*, vol. 31, no. 6, pp. 3486–3495, 1985.
- [87] RABI, I., MILLMAN, S., KUSCH, P., and ZACHARIAS, J. R., "The molecular beam resonance method for measuring nuclear magnetic - moments the magnetic moments of li-3(6) li-3(7) and f-9(19)," *Physical Review*, vol. 55, no. 6, pp. 0526–0535, 1939.
- [88] RAMSEY, N., *Molecular beams*. The International series of monographs on physics, Oxford: Clarendon Press, 1956.
- [89] ROACH, P. J., WOODWARD, W. H., CASTLEMAN, A. W., REBER, A. C., and KHANNA, S. N., "Complementary active sites cause size-selective reactivity of aluminum cluster anions with water," *Science*, vol. 323, no. 5913, pp. 492–495, 2009.
- [90] ROTH LISBERGER, U. and ANDREONI, W., "Structural and electronic-properties of sodium microclusters (n=2-20) at low and high-temperatures - new insights from abinitio molecular-dynamics studies," *Journal of Chemical Physics*, vol. 94, no. 12, pp. 8129–8151, 1991.
- [91] SABIN, J. R., TRICKEY, S. B., APELL, S. P., and ODDERSHEDE, J., "Molecular shape, capacitance, and chemical hardness," *International Journal of Quantum Chemistry*, vol. 77, no. 1, pp. 358–366, 2000.
- [92] SCHMIDT, M. and HABERLAND, H., "Optical spectra and their moments for sodium clusters, na-n(+), with $3 \leq n \leq 64$," *European Physical Journal D*, vol. 6, no. 1, pp. 109–118, 1999.
- [93] SCHMIDT, M., KUSCHE, R., HIPPLER, T., DONGES, J., KRONMULLER, W., VON ISSENDORFF, B., and HABERLAND, H., "Negative heat capacity for a cluster of 147 sodium atoms," *Physical Review Letters*, vol. 86, no. 7, pp. 1191–1194, 2001.
- [94] SCHNELL, M., HERWIG, C., and BECKER, J. A., "Analysis of semiconductor cluster beam polarization taking small permanent dipole moments into account," *Zeitschrift Fur Physikalische Chemie-International Journal of Research in Physical Chemistry & Chemical Physics*, vol. 217, no. 8, pp. 1003–1030, 2003.
- [95] SCOLES, G., *Atomic and Molecular Beam Methods, V1*, vol. 1. Oxford University Press, 1988.
- [96] SCULLY, S. W. J., EMMONS, E. D., GHARAIBEH, M. F., PHANEUF, R. A., KILCOYNE, A. L. D., SCHLACHTER, A. S., SCHIPPERS, S., MULLER, A., CHAKRABORTY, H. S., MADJET, M. E., and ROST, J. M., "Photoexcitation of a volume plasmon in c-60 ions," *Physical Review Letters*, vol. 94, no. 6, p. 4, 2005.
- [97] SELBY, K., KRESIN, V., MASUI, J., VOLLMER, M., DEHEER, W. A., SCHEIDEMANN, A., and KNIGHT, W. D., "Photoabsorption spectra of sodium clusters," *Physical Review B*, vol. 43, no. 6, pp. 4565–4572, 1991.
- [98] SIVIA, D. S., *Data analysis : a Bayesian tutorial*. Oxford science publications, Oxford :: Clarendon Press ;, 1996.
- [99] SOLOV'YOV, I. A., SOLOV'YOV, A. V., and GREINER, W., "Structure and properties of small sodium clusters," *Physical Review A*, vol. 65, no. 5, p. 19, 2002.

- [100] TIKHONOV, G., KASPEROVICH, V., WONG, K., and KRESIN, V. V., "A measurement of the polarizability of sodium clusters," *Physical Review A*, vol. 6406, no. 6, p. 5, 2001.
- [101] TIKHONOV, G., WONG, K., KASPEROVICH, V., and KRESIN, V. V., "Velocity distribution measurement and two-wire field effects for electric deflection of a neutral supersonic cluster beam," *Review of Scientific Instruments*, vol. 73, no. 3, pp. 1204–1211, 2002.
- [102] TOWNES, C. H., *Microwave spectroscopy*. International series in pure and applied physics, New York: McGraw-Hill, 1955.
- [103] VISUTHIKRAISEE, V. and BERTSCH, G. F., "Spin-rotation coupling in ferromagnetic clusters," *Physical Review A*, vol. 54, no. 6, pp. 5104–5109, 1996.
- [104] VON ISSENDORFF, B. and CHESHNOVSKY, O., "Metal to insulator transitions in clusters," *Annual Review of Physical Chemistry*, vol. 56, pp. 549–580, 2005.
- [105] WANG, C. R., HUANG, R. B., LIU, Z. Y., and ZHENG, L. S., "Lognormal size distributions of elemental clusters," *Chemical Physics Letters*, vol. 227, no. 1-2, pp. 103–108, 1994.
- [106] WANG, C. R., HUANG, R. B., LIU, Z. Y., and ZHENG, L. S., "Statistical size distribution of laser-generated clusters," *Chemical Physics*, vol. 201, no. 1, pp. 23–34, 1995.
- [107] XIA, C. L., YIN, C. R., and KRESIN, V. V., "Photoabsorption by volume plasmons in metal nanoclusters," *Physical Review Letters*, vol. 102, no. 15, p. 4, 2009.
- [108] XU, X. S., YIN, S. Y., MORO, R., and DE HEER, W. A., "Distribution of magnetization of a cold ferromagnetic cluster beam," *Physical Review B*, vol. 78, no. 5, p. 13, 2008.
- [109] XU, X., *The magnetism of free cobalt clusters measured in molecular beams*. 2006. de Heer, Walter A., Committee Chair ; Chou, Meiyin, Committee Member ; Whetten, Robert L., Committee Member ; First, Phillip N., Committee Member ; Pummer, Earl Ward, Committee Member.
- [110] YIN, S. Y., XU, X. S., LIANG, A., BOWLAN, J., MORO, R., and DE HEER, W. A., "Electron pairing in ferroelectric niobium and niobium alloy clusters," *Journal of Superconductivity and Novel Magnetism*, vol. 21, no. 5, pp. 265–269, 2008.

VITA

Anthony was born in Tucson, Arizona, USA on Nov 25, 1980. When he was four his family and him left the country and went to Taiwan. He was then educated in Tainan, a city located in the southern part of Taiwan which is famous for its snacks, until he graduated from Tainan First High School in 1999. Then he left his home town and went to National Taiwan University in Taipei for further education. Later on he received a BS degree in Physics in 2003. He came to Georgia Tech, Atlanta, in 2003 Fall, to study for a Ph.D. degree in Physics. Anthony was interested in physics since he was very young. He is very grateful that he came to Georgia Tech to study the frontier physics in this wonderful environment.